

ELS-LEED study of collective electronic
excitations on Ag surfaces and thin films

Vom Fachbereich Physik
der Universität Hannover
zur Erlangung des Grades
Doktor der Naturwissenschaften

Dr. rer. nat.
genehmigte Dissertation

von

Francesca Moresco
geboren am 27. Februar 1965
in Genua (Italien)

1998

Referat: Prof. Dr. Martin Henzler
Korreferat: Prof. Dr. Mario Rocca
Tag der Prüfung: 13. November 1998

Abstract

Collective electronic excitations on Ag surfaces and thin films have been studied by ELS-LEED, a technique which allows to investigate both energy loss spectra and elastically diffracted electrons, with high energy and momentum resolution.

Surface plasmon energy and dispersion have been reinvestigated on Ag(111) and Ag(110). In agreement with previous literature we find a positive parabolic dispersion, with a linear term anisotropic with respect to crystal face and, for Ag(110), also to crystal azimuth. On the contrary, the quadratic term of surface plasmon dispersion has the same value for Ag(111) and Ag(110). The improved quality of the data allows moreover to separate the contribution to the loss spectra due to monopole and to multipole plasmon, proving the existence of the latter mode also on noble-metal surfaces.

The meaning of the linear and of the quadratic term of Ag surface plasmon dispersion has been studied in better detail by observing the effects of the K-induced missing row reconstruction on the surface plasmon dispersion of Ag(110). We prove that the nearly linear surface plasmon dispersion of Ag(001) is due to the presence on of interband transitions which nearly match the surface plasmon energy.

Finally, the investigation of thin films of Ag deposited on Si(111) has allowed to correlate the electronic collective properties with the morphology of the film, showing that the plasmon of a polycrystalline Ag layer is strongly influenced by the dimension of the grains and that it behaves like the Mie resonance of Ag clusters of the same size. Moreover we demonstrate that the plasmon is confined inside the single domain, showing a dispersion only for wavelength smaller than the lateral dimension of the grain.

Keywords

Plasmon, silver surfaces, thin films.

Contents

Introduction	3
1 Theory	7
1.1 What is a surface plasmon	7
1.2 Surface plasmon dispersion	10
1.2.1 Simple metal surfaces	10
1.2.2 Ag surfaces	13
1.2.3 Ag particles and thin films	17
2 Experimental	21
2.1 ELS-LEED	21
2.2 Inelastic scattering of electrons	24
2.3 Elastic diffraction of electrons	26
2.4 Technical details	28
2.4.1 The chamber	28
2.4.2 Preparation of the Ag surfaces	29
2.4.3 K induced reconstruction of the Ag(110) surface	29
2.4.4 Ag thin layers on Si(111) 7x7	30
3 Surface plasmon on Ag surfaces	33
3.1 Introduction	33
3.2 Data presentation	34
3.3 Surface plasmon dispersion	36
3.4 Temperature dependence	40
3.5 Surface plasmon damping	41
3.6 Multipole plasmon mode	45

4	K adsorption on Ag(110)	51
4.1	Introduction	51
4.2	Surface Structure	52
4.3	Surface electronic excitations	59
4.3.1	Influence of a trace amount of K on surface plasmon dispersion	59
4.3.2	Surface plasmon dispersion at higher K coverage on the reconstructed surfaces	64
4.3.3	Surface plasmon damping on the reconstructed surfaces	68
4.3.4	Surface plasmon at higher K coverage on the unrecon- structed surface	69
4.4	Collective excitations on K layers	75
5	Thin Ag films	81
5.1	Introduction	81
5.2	SPA-LEED analysis of the Ag overlayer	82
5.3	Plasmon energy on Ag overlayers	90
5.4	Plasmon dispersion on Ag overlayers	95
5.5	Plasmon damping on Ag overlayers	99
	Conclusions and outlook	103
	Bibliography	107

Acronyms

AES: Auger Electron Spectroscopy

ELS-LEED: Energy Loss Spectroscopy - Low Energy Electron Diffraction

FHWM: Full Width at Half Maximum

HREELS: High Resolution Electron Energy Loss Spectroscopy

LDA: Local Density Approximation

LEED: Low Energy Electron Diffraction

RPA: Random Phase Approximation

SBZ: Surface Brillouin Zone

SPA-LEED: Spot Profile Analysis of LEED

STM: Scanning Electron Microscopy

Introduction

Surface plasmons are the normal modes of charge fluctuation at a metallic surface and govern the long range interaction between a metal and the rest of the world [1]. Since collective electronic excitations influence fundamental transport and optical properties and are very sensitive to the details of the electronic density, understanding the relation between surface plasmon dispersion and damping and the properties of a semi-infinite electron gas has accordingly become a focus of research effort, that attracted attention for more than 20 years [2].

Moreover, electrical and optical properties of thin films have been studied over decades. These systems represent quasi two-dimensional electron gases whose average density and thickness can be easily modified. Besides, thin metallic overlayers deposited on semiconductor surfaces are of great interest, especially for the application to the miniaturization of integrated circuits.

During the past few years, collective electronic excitations have been experimentally investigated over a variety of different systems, including simple metals, charged surfaces, stepped surfaces, noble metals, thin adsorbate layers over a wide range of coverages and small metal particles, by means of different spectroscopic techniques, including electrons, atoms and photons. Considerable recent progress has also been achieved in the theoretical description of surface excitations. Time dependent density functional theory is now able to reasonably describe collective electronic excitations [3], giving an overall consistency to the experimental observation and providing very interesting interconnections among a variety of systems.

However, although the behaviour of electronic excitations can be said to be understood in the case of simple metals, the available theoretical models are not able to completely describe more complex systems, like d-electron metals. In this respect, Ag surfaces became a paradigm for the understanding of collective electronic excitations, because of the extremely small width of

the surface plasmon loss, which permits precise measurements.

Recent HREELS experiments of surface plasmon dispersion on Ag surfaces showed a positive dispersion (in contrast to the negative dispersion of simple metals), anisotropic with respect to the crystallographic face and, for Ag(110), also to the crystal azimuth. Such effect is obviously connected to the presence of d-electrons, but the origin of the anisotropy is still debated theoretically and the HREELS results of different laboratories are not in agreement on the quantitative evaluation of the dispersion's slope, showing that further experimental studies of the excitation spectrum of Ag was needed, possibly improving the momentum resolution, which is one of the major limiting factors in HREELS studies of surface plasmon dispersion.

In the present work, Energy Loss Spectroscopy of Low Energy Electron Diffraction (ELS-LEED), has been for the first time applied to the study of collective electronic excitations of silver surfaces, allowing to strongly reduce the experimental error in determining surface plasmon dispersion. Moreover, being ELS-LEED a combination of SPA-LEED and HREELS, it permits to contemporarily measure the electronic loss spectra and the profile of the LEED spots, making possible to relate geometrical properties and electronic excitations at the surface. In this thesis, surface plasmon dispersion and damping on Ag surfaces have been reinvestigated by ELS-LEED, separating for the first time the contribution to the loss intensity due to monopole and multipole surface plasmon. The meaning of the anisotropy of surface plasmon dispersion on Ag surfaces has been then deeply studied, by means of deposition of a small amount of K on Ag(110), which induces extended missing row reconstructions and modifies the electron band structure at the surface. Moreover, a combined study of structural properties and collective excitations has been performed on thin Ag overlayers deposited on Si(111), demonstrating that polycrystalline Ag grains behave like single clusters, confining the plasmon.

The vast range of experimental observations and the high experimental accuracy of the present investigation allows to better understand the complexity of electronic excitation spectra on silver, experimentally proving the fascinating prediction of the theory developed by A. Liebsch, which states that the electronic excitations of semi-infinite surfaces, thin films and clusters are governed by the same physical mechanism. I hope that the present results provide interesting material for developing new theoretical model calculations, able to better understand the electronic excitation spectra of d-electron metals.

The outline of this thesis is the following: the fundamental theoretical concepts of surface electronic excitations are introduced in chapter 1, while the experimental method is discussed in chapter 2 with a brief review of the fundamental concepts of electronic inelastic and elastic scattering off surfaces. The experimental results of surface plasmon dispersion measurements are discussed in chapter 3 for clean Ag(111) and Ag(110) surfaces, while in chapter 4 the influence of K adsorption on Ag(110) surface plasmon dispersion and geometrical structure is reported, together with the study of the electronic excitations on thin K overlayers. The investigation of thin Ag films deposited on Si(111) is finally presented in chapter 5, where a combined study of the structural geometrical properties of the layer and of the collective excitations spectra is reported.

Chapter 1

Theory

1.1 What is a surface plasmon

The interaction between a metallic surface and an external electromagnetic field creates a coherent superposition of electron-hole pairs that represents a wave-like disturbance of the charge density localized at the surface and that is called a surface plasmon [4]. Surface plasmons are the normal modes of charge fluctuation at a metallic surface [1] and, like their bulk counterpart, are longitudinal modes.

If we characterize the charge compression and rarefaction along the surface associated with a surface plasmon by a wave vector q_{\parallel} , we obtain from classical electrodynamics that the associated electric potential must decay exponentially away from the surface:

$$\Phi(\mathbf{r}) = \Phi_0 e^{i\mathbf{q}_{\parallel} \cdot \mathbf{r}_{\parallel}} e^{-q_{\parallel}|z|} \quad (1.1)$$

where \mathbf{r}_{\parallel} is the position vector in the surface plan and z is the distance normal to the surface measured from the truncation plane of the crystal.

The normal component of the electric field associated with eq.(1.1), E_z , obtained by differentiating eq.(1.1) with respect to the z direction, is discontinuous across the surface:

$$\begin{cases} E_z(z = 0^+) = \Phi_0 q_{\parallel} e^{i\mathbf{q}_{\parallel} \cdot \mathbf{r}_{\parallel}} \\ E_z(z = 0^-) = -\Phi_0 q_{\parallel} e^{i\mathbf{q}_{\parallel} \cdot \mathbf{r}_{\parallel}} \end{cases} \quad (1.2)$$

As no unbalanced surface charge can exist at a metallic surface, we must require that $\nabla \cdot \mathbf{D} = 0$ so that, if the metal that occupies the negative half-

space ($z < 0$) is characterized by the dielectric function $\epsilon(\omega)$, we obtain:

$$\epsilon(\omega) = -1 \quad (1.3)$$

This relation defines the surface plasma frequency, which is hence determined by bulk properties of the solid. For a free electron gas:

$$\epsilon(\omega) = 1 - \omega_p^2/\omega^2 \quad (1.4)$$

where

$$\omega_p = \sqrt{ne^2/m\epsilon_0} \quad (1.5)$$

is the plasma frequency in the bulk (occurring at $\epsilon(\omega_p) = 0$). Inside the Drude model eq.(1.3) admits the solution

$$\omega_s = \omega_p/\sqrt{2} \quad (1.6)$$

which represents a good approximation for long wavelength oscillations of the surface charge layer.

If the surface is not flat eq.(1.3) has to be modified. For spherical metal particles, a surface excitation at the Mie frequency [5] is expected when:

$$\epsilon(\omega_M) = -2 \Rightarrow \omega_M = \frac{\omega_p}{\sqrt{3}} \quad (1.7)$$

Moreover, in the case of noble metals, the presence of the filled d band close to the Fermi level strongly influence the dielectric function. On silver the simple relation (1.6) between bulk and surface plasmon does not hold anymore because of the mutual polarization between the $5s$ and $4d$ states. Such s - d polarization is responsible for a large renormalization of the Ag volume plasma frequency that can be explained representing qualitatively the dielectric function of Ag by [6, 7]:

$$\epsilon(\omega) = \epsilon_s(\omega) + \epsilon_d(\omega) - 1 \quad (1.8)$$

where $\epsilon_s(\omega)$ is the Drude term, appropriate for the $5s$ electrons and $\epsilon_d(\omega)$ is the bound electron contribution whose frequency dependence is governed by the interband transitions from the occupied $4d$ band to the $5s$ conduction band, close to the Fermi level. As reported in Fig.1.1, near to the region of the collective mode of Ag, $\epsilon_d(\omega)$ is real and has a value of about $5 \div 6$ [8]. The effect of this bound term is to reduce the volume plasma frequency from

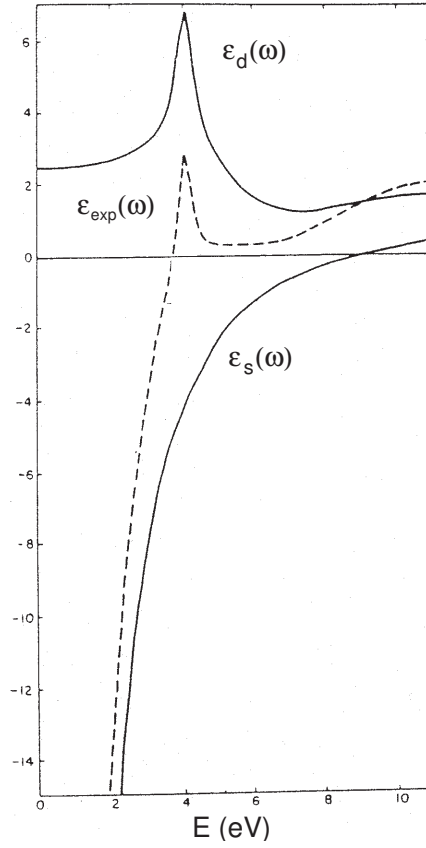


Figure 1.1: Dielectric function $\epsilon(\omega)$ versus energy for Ag measured optically, from ref.[8].

the unscreened value $\omega_p = 9.2$ eV (as calculated from eq.(1.5) for $n = 5$) to the observed value [3]:

$$\omega_p^* = \frac{\omega_p}{\sqrt{Re(\epsilon_d)}} \approx 3.8 \text{ eV} \quad (1.9)$$

Accordingly, the frequency of the surface plasmon is given by

$$\omega_s^* = \frac{\omega_p}{\sqrt{1 + Re(\epsilon_d)}} \approx 3.7 \text{ eV} \quad (1.10)$$

as confirmed by optical measurements [9, 10] whereas the unscreened value is

$\omega_s = \omega_p/\sqrt{2} = 6.5$ eV. Moreover the frequency of the Mie resonance becomes:

$$\omega_M^* = \frac{\omega_p}{\sqrt{2 + \text{Re}(\epsilon_d)}} \approx 3.5 \text{ eV} \quad (1.11)$$

where the unscreened value is $\omega_M = \omega_p/\sqrt{3} = 5.3$ eV.

1.2 Surface plasmon dispersion

We want now to give an overview on the dynamical response of electrons at a metal surface to a time varying external field. In the most simple case we can describe the surface as a positive charge background while the valence electrons are considered free. We'll see that such a model, known as "jellium model", is able to correctly describe the surface plasmon dispersion of simple metals, but that it fails in the case of Ag, where the presence of d electrons and the subsequent s - d polarization has a strong influence on the dynamical response at the surface.

1.2.1 Simple metal surfaces

The jellium model represents a metallic surface as a positively charged background that occupies the half space $z < 0$ and considers the valence electrons as free. Applying to a jellium surface a weak uniform external static field normal to the surface, the system will respond by creating an induced charge $\delta n(z)$ localized in the surface region [11]. If such applied field is dynamic, at finite frequencies the surface charge density $\delta n(z, q, \omega)$ will be a complex function. If we define the surface response function $g(q_{\parallel}, \omega)$ as

$$g(q_{\parallel}, \omega) = \int dz e^{qz} \delta n(z, q, \omega) \quad (1.12)$$

the probability of exciting electron-hole pairs or collective modes via elastic scattering of electrons will be determined from the imaginary part of $g(q_{\parallel}, \omega)$. $\text{Im}(g(q_{\parallel}, \omega))$ has been calculated within the local density approximation (LDA) and its frequency dependence is reported in Fig.1.2 for the case of potassium, at several q_{\parallel} [6]. The volume plasmon frequency of this system, as calculated inside the jellium model from eq. (1.5), lies at $\omega_p = 4.2$ eV, as the electronic density of potassium is $n = 4$. The main peak near

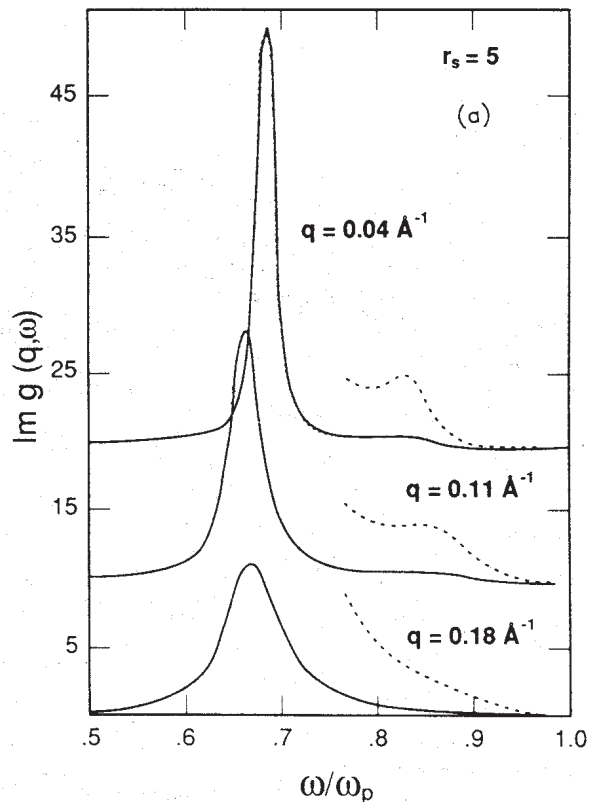


Figure 1.2: Frequency dependence of the surface loss function $Im g(q_{||}, \omega)$ for potassium, from ref. [6].

to $\omega_s = 3.0$ eV corresponds to the usual surface monopole mode, while the weaker spectral feature above $\omega_m \approx 0.8\omega_p$, $\omega_m \approx 3.4$ eV, corresponds to the so called "multipole surface mode" whose charge fluctuation normal to the surface has an extra node compared to the monopole charge distribution associated with an ordinary surface plasmon.

As we have seen on page 8, in the standard treatment of the dielectric response of a metal surface, one assumes that the solid is characterized by a local dielectric function $\epsilon(\omega)$ which jumps discontinuously at the surface, i.e.

$$\begin{cases} \epsilon = \epsilon(\omega) & \text{for } z < 0 \\ \epsilon = 1 & \text{for } z > 0 \end{cases} \quad (1.13)$$

where $\epsilon(\omega)$ is the Drude dielectric function $\epsilon(\omega) = 1 - \omega_p^2/\omega^2$.

From the continuity of \mathbf{D} across the solid-vacuum interface one obtains:

$$\text{Im } g(q_{\parallel}, \omega) = \frac{\epsilon(\omega) - 1}{\epsilon(\omega) + 1} \quad (1.14)$$

while the surface plasmon frequency is defined by the pole of the response function, i.e. by the condition $\epsilon(\omega) = -1$, already seen in Eq.(1.3). The relation (1.14), exact for $q_{\parallel} = 0$, is not correct for arbitrary q_{\parallel} because it does not consider that a real metal does not have a steplike surface profile, but a profile which varies smoothly on a microscopic scale.

Feibelman [1] has demonstrated that, to correctly describe the surface plasmon dispersion, the position of the surface screening charge relative to the jellium edge has to be considered. This may be seen by expanding the surface response function $g(q_{\parallel}, \omega)$ at small q_{\parallel} :

$$g(q_{\parallel}, \omega) \approx \frac{\epsilon(\omega) - 1 + q_{\parallel}d(\omega)[\epsilon(\omega) - 1]}{\epsilon(\omega) + 1 - q_{\parallel}d(\omega)[\epsilon(\omega) - 1]} \quad (1.15)$$

where $d(\omega)$ is the centroid of the surface screening charge induced by an electrical field normal to the surface, measured from the edge of the positive charge background. $d(\omega)$ is schematically shown in Fig.1.3 and it reads:

$$d(\omega) = \frac{\int dz z \delta n(z, 0, \omega)}{\int dz \delta n(z, 0, \omega)} \quad (1.16)$$

For $\omega \neq 0$, $d(\omega)$ is a complex quantity and, from the pole of the surface response function $g(q_{\parallel}, \omega)$, we find that the dispersion relation of the surface plasmon at small q_{\parallel} is given by:

$$\omega_s(q_{\parallel}) = \omega_s \left[1 - \frac{1}{2} q_{\parallel} \text{Re}(d(\omega_s)) + O(q_{\parallel}^2) \right] \quad (1.17)$$

Since $\text{Re}(d(\omega_s))$ has been calculated to be positive for all simple metals [1], the surface scattering process causes a negative dispersion at small q_{\parallel} .

The initial negative dispersion of the surface plasmon can be understood in terms of a simple physical picture. We have seen that the centroid of the surface screening charge is located outside the jellium edge, where the density of the electron gas is lower and the compressibility is higher than inside the crystal. Moreover the induced electric potential associated with this charge is $\propto \exp(-q_{\parallel}z)$ (eq.(1.1)) and decays exponentially towards the interior of

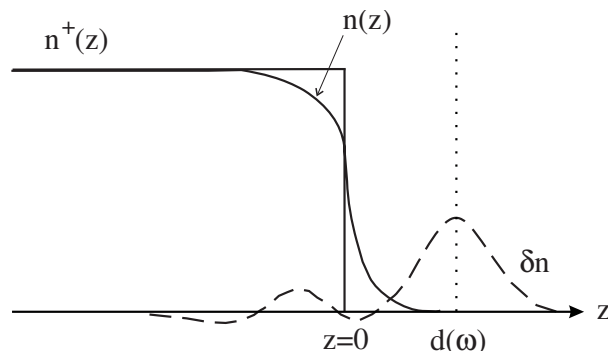


Figure 1.3: Position of the centroid of the dynamical screening charge $d(\omega)$ with respect to the geometric surface. $n^+(z)$ represent the positive jellium background, $n(z)$ the negative charge density and δn the induced density.

the metal, up to a distance depending on q_{\parallel} . The perturbation is therefore more localized with increasing q_{\parallel} and therefore extends over a region of lower charge density. As a lower density implies, from eq.(1.5), a lower plasmon frequency, the plasmon dispersion will be negative.

The theoretical prediction of the jellium model is in good agreement with the experimental data obtained by HREELS on all simple metals [12, 13, 14], which show in fact a negative initial dispersion.

1.2.2 Ag surfaces

Electron energy loss investigation on the low-index crystal faces of Ag has recently shown [2, 15, 16, 17] that the surface plasmon disperses towards higher frequencies with increasing parallel momentum q_{\parallel} . It has also been observed that Ag surface plasmon dispersion is anisotropic with respect to crystal face and, for Ag(110), also to crystal azimuth. Such behaviours are in contrast to the experimental observations on simple metals and to the predictions of the jellium model.

Silver has a special electronic structure, with a nearly free electron character down to almost 4 eV below the Fermi energy. Interband transitions involving occupied d bands or from $s-p$ states near the Fermi level to unoccupied $s-p$ bands have in fact a well defined onset at about 4 eV. Nevertheless the behaviour of the Ag surface plasmon is completely different from the free electron case and indicates that the $4d$ bands play a very important role in

the collective surface excitations of Ag.

Liebsch has shown [7] that the presence of the Ag 4*d* electrons influences the mechanism that determines the initial dispersion of the surface plasmon and has theoretically explained the observed blueshift of the Ag surface plasmon frequency with q_{\parallel} and of the Mie resonance with the inverse of the particle size. In the model of Liebsch [6], as schematically shown in Fig.1.4, the 5*s* conduction electrons are treated as a seminfinite homogeneous electron gas and the influence of the 4*d* electrons is described as a polarizable medium, via the same local dielectric function $\epsilon_d(\omega)$ of the bulk, defined in eq.(1.8). The position of the boundary up to which this polarizable medium extends is denoted by z_d and is the only free parameter of the model.

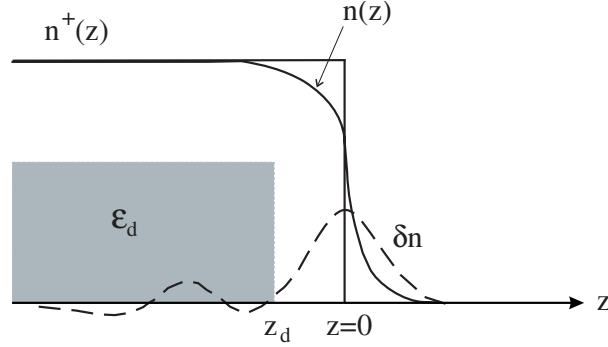


Figure 1.4: Schematic model for the dynamical response of a two-component 5*s*-4*d* electron system: n_0 denotes the ground density profile of the 5*s* electrons, δn the induced density charge and n^+ the positive jellium background.

The frequency dependence of the real part of ϵ_d and ϵ_s has been shown in Fig.1.1. In Fig.1.5 are reported the dispersion curves of Ag surface plasmon for $z_d = 0$ and $z_d = \pm 0.8\text{\AA}$ calculated within the random phase approximation (RPA). In the limit of small q_{\parallel} the curves converge to the frequency ω_s^* which is determined only by the bulk dielectric function and is therefore independent on z_d . At finite q_{\parallel} , the initial dispersion is positive for $z_d < 0$. This means that the absence of the *s*-*d* interaction in the region where $z > z_d$ causes a blue shift of the surface plasma frequency with increasing q_{\parallel} . The large red shift from the bare plasmon frequency $\omega_s(q)$ to the screened one $\omega_s^*(q)$ (defined in eq.(1.10)), due to the mutual polarization of *s* and *d* states, depends in fact strongly on q_{\parallel} and it is largest in the limit of small q_{\parallel} because the induced field decays in this case very slowly into the solid.

This behaviour can be better understood considering that, inside the bulk, the Coulomb interaction between two s electrons is fully screened by the medium representing the d states. At the surface, because of the spill-out of the s electrons, the s - d screening is reduced so that the exponential decay of the plasmon field is fully screened in the $q_{\parallel} = 0$ limit and partially screened for $q_{\parallel} \neq 0$. At finite q_{\parallel} there is a competition between two opposite trends: the usual negative dispersion of simple metals and a positive dispersion due to the apparent reduction of ϵ_d . The balance between these mechanisms depends on the location of the boundary z_d of the polarizable medium. The calculations of Liebsch [6] and the experimental results indicate that the second effect, connected to a blue shift of the plasmon, dominates.

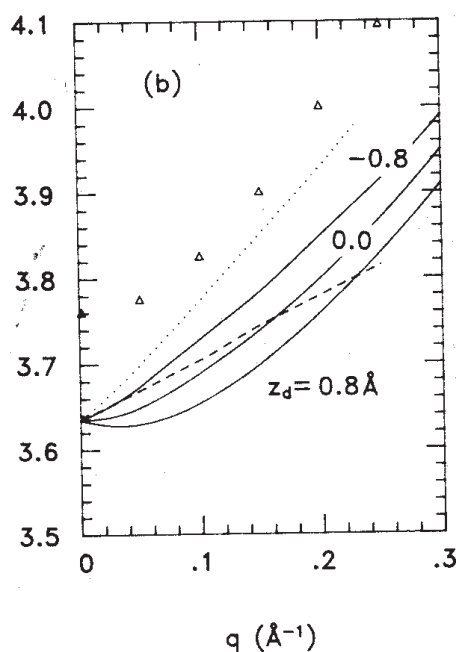


Figure 1.5: Dispersion of Ag surface plasmon for $z_d = 0$ and $z_d = \pm 0.8 \text{ \AA}$, from ref. [6]. The dotted and dashed lines are the measured dispersions on Ag(001) and Ag(111), from ref. [16,17]. The triangles show the dispersion of the bulk plasmon.

To conclude the description of the Liebsch's model, it is useful to reformulate the above results in terms of a complex self-energy [6], to be able to compare the dispersion of plasmons on Ag surfaces, clusters and thin film.

The Ag surface response function at small q_{\parallel} can be rewritten in the form:

$$g(q_{\parallel}, \omega) = \frac{\epsilon(q_{\parallel}, \omega) - 1}{\epsilon(q_{\parallel}, \omega) + 1} \quad (1.18)$$

where $\epsilon(q_{\parallel}, \omega)$ is now an effective dielectric function given by:

$$\epsilon(q_{\parallel}, \omega) = 1 - \frac{\omega_p^2}{\omega^2 + \Sigma(q_{\parallel}, \omega)} + (\epsilon_d - 1) \quad (1.19)$$

$\Sigma(q_{\parallel}, \omega)$ represent the self-energy and, at frequencies close to the surface plasmon, can be parametrized as:

$$\Sigma(q_{\parallel}, \omega) = q_{\parallel} d(\omega) \omega_s^{*2} \quad (1.20)$$

In this way the exact nonlocal surface response $g(q_{\parallel}, \omega)$ at small q_{\parallel} is written in terms of a "classical" dielectric function whose self-energy accounts for the quantum-mechanical surface effects and the nonlocal aspects of the response.

According to the poles of $g(q_{\parallel}, \omega)$, the dispersion of the Ag surface plasmon at small q_{\parallel} is given by:

$$\omega_s^*(q_{\parallel}) = \omega_s^* \left[1 - \frac{1}{2} q_{\parallel} D_s + O(q_{\parallel}^2) \right] \quad (1.21)$$

where $D_s = \text{Re} D(\omega_s^*)$. The experimental curves for Ag surfaces correspond to negative values of D_s , between -0.3 and -0.8 Å.

It is important to note that the observed anisotropy of Ag surface plasmon dispersion is not described by the model of Liebsch. Such model is based in fact on an abruptly terminated dielectric medium, not able to consider face-dependent effects. Moreover it is obvious that no one-parameter model can completely explain the full complexity of the experimental dispersion.

A totally different theoretical explanation of the positive dispersion on Ag surfaces has been given by Feibelman [18]. His approach starts from the consideration that, due to the vicinity of the plasmon energy to the onset of interband transitions, the surface plasmon of Ag can be considered as a frustrated, collective $d \rightarrow s$ excitation. The position of the centroid of the induced charge $d(\omega)$ is governed by the matrix element of such $d \rightarrow s$ transition:

$$d \propto \left| \int dz \Phi(z) \Psi_d(z) \Psi_s^*(z) \right|^2 \quad (1.22)$$

where $\Phi(z)$ is the electrical potential associated to the surface plasmon, $\Psi_d(z)$ is the wave function corresponding to an occupied d orbital, and $\Psi_s(z)$ refers to an unoccupied state, e.g. a $5s$ level above the Fermi energy. Since the surface plasmon electric field, which is the z -derivative of $\Phi(z)$, decreases rapidly towards the interior of the crystal, $\Phi(z)$ varies very rapidly near to the surface edge, while a few Å below the surface it varies with z . One therefore expects that the contribution of the d electrons to $d(\omega)$ is enhanced as a function of their proximity to the surface. Accordingly, the linear slope of the plasmon dispersion, determined by $d(\omega)$, will be smaller for Ag(111) where the d electrons states are located more deeply below the geometric surface than for Ag(100) whose d -electrons lie closer to the jellium edge and it will be more positive in the more corrugated $\langle 100 \rangle$ direction than in the $\langle 1\bar{1}0 \rangle$ direction of Ag(110). Notably in this model only the outermost layer of d -electrons has been considered to qualitatively explain the observed effect on the surface plasmon dispersion. We will see in section 4.3.1 that such explanation is not in agreement with the experimental results of the present work, as we have observed that an increased surface corrugation along the $\langle 001 \rangle$ direction of Ag(110), connected to surface reconstruction, does not determine an increase of the positive dispersion slope, compared to the unreconstructed case [19].

1.2.3 Ag particles and thin films

The Mie resonance of small Ag particles was observed to shift to higher frequencies with decreasing particle size, thus showing an opposite behaviour respect to the red shift seen for the Mie resonance of small simple metal particles [20, 21, 22]. Fig.1.6 shows the variation of the Ag Mie resonance with the inverse of the particle radius [22]. As in the case of Ag surface plasmon dispersion, the presence of the filled $4d$ levels changes the sign of the variation of the particle resonance frequency.

Liebsch has applied the same model used for the case of the Ag surface to determine the adsorption spectrum of Ag particles [6]. The potential associated to the dynamically induced charge density is screened due to the presence of the polarizable medium representing the occupied $4d$ states. Such a medium can again be represented by the same bound dielectric contribution $\epsilon_d(\omega)$ as in the volume.

The important feature of the model is again that the s - d interaction is absent in the surface region, where the $5s$ electrons spill out into the

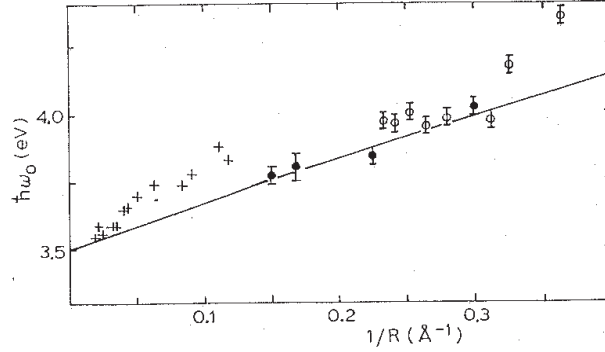


Figure 1.6: Variation of the Mie resonance with the inverse of the particle radius [22]. The solid line is a fit through the experimental data.

vacuum. A part of the density fluctuation associated with the Mie resonances oscillates then with the (higher) unscreened plasma frequency, determining an increase of the resonance frequency. Such effect becomes more pronounced with decreasing particle radius because of the larger surface to volume ratio, thus explaining the observed blue shift with decreasing particle size.

In analogy with eq. (1.21), the size dependence of the Ag Mie resonance at large particle radius (R) can be written as:

$$\omega_M^*(R) = \omega_M^* \left[1 - \frac{1}{2} R^{-1} D_M \left(\frac{\omega_s^*}{\omega_M^*} \right)^2 + O((1/R)^2) \right] \quad (1.23)$$

where $\omega_M^* = 3.5$ eV. Because of the closeness of the frequency ω_s^* and ω_M^* this relation shows that the linear coefficient of the Mie resonance should be nearly the same of the one of the surface plasmon, i.e. $D_s \approx D_M$. Experimentally one finds indeed that [21, 22] $D_M = -0.85$ Å.

A similar relationship was observed for the plasma frequency of Ag thin films, which increases with the inverse of its thickness, t [23, 24]. According to Liebsch [3] the reason of the blue shift of the Ag overlayer mode with $1/t$ is the finite, rather than semi-infinite, range in which the s - d polarization is active. As the coverage is reduced, the overall screening of the plasmon charge via the polarizable d electron medium diminishes, giving a correspondingly higher frequency. Moreover, the spill out region not affected by the s - d polarization becomes relatively more important, causing a further blue shift of the plasma frequency. The dependence of the plasma frequency of the Ag overlayer can be written, in analogy to the case of clusters and seminfinite

surfaces, as:

$$\omega_L^*(t) = \omega_L^* \left[1 - \frac{1}{2} t^{-1} D_L(\omega_L) + O((1/t)^2) \right] \quad (1.24)$$

It is important to underline that in the model of Liebsch the three phenomena described, i.e. the dispersion of Ag surface plasmon with q_{\parallel} , the blue shift of the Mie resonances on Ag clusters with $1/R$ and the linear shift of the overlayer mode with $1/t$, are governed by the same physical mechanism. A similar value for the slope of the plasmon's shift is accordingly expected for the three cases.

Chapter 2

Experimental

2.1 ELS-LEED

Scattering experiments are an important source of information to study the geometrical and vibrational properties of a surface. Elastic scattering can tell us something about the symmetry and the geometric arrangement of atoms near to the surface, while inelastic scattering yields information about possible excitations at a surface or at an interface, both of electronic or of vibronic kind [25].

Low energy electrons penetrate only a few Ångstrom into materials and, among the variety of particles that can be used for surface scattering experiments, play a rather important role. Slow electrons can be in fact produced by a simple electron gun and can be easily deflected and analyzed in energy by means of electrostatic methods and finally detected by a channeltron.

The experimental technique used in the present work (Energy Loss Spectroscopy of Low Energy Electron Diffraction, acronym ELS-LEED) is a unique method which allows to study both inelastically and elastically electrons scattered from a surface, thus giving information about the geometric order at the surface and in the same time about energy and dispersion of surface excitations.

The Spot Profile Analysis of the LEED peaks (SPA-LEED) is a well developed technique to quantitatively evaluate the deviations from periodicity of surface arrangements due to any kind of defects [26]. A conventional SPA-LEED makes use of an electronic deflection unit to scan the elastically scattered electrons at each point in reciprocal space.

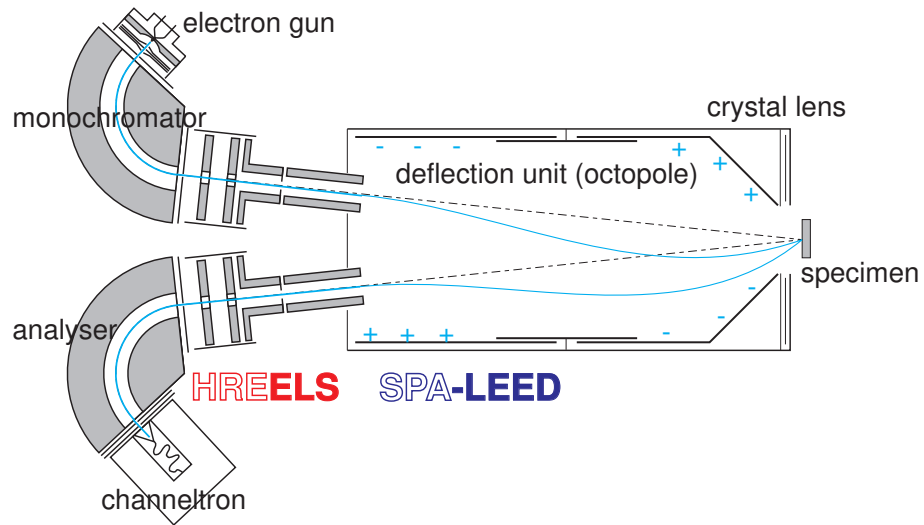


Figure 2.1: A schematic view of the ELS-LEED spectrometer

On the other hand, High Resolution Electron Energy Loss Spectroscopy (HREELS) is a standard surface science technique, able to measure the electrons inelastically diffracted from a surface, with an energy resolution of some meV [27].

The combination of the deflection unit from a SPA-LEED with the monochromator and the analyzer of a HREELS yields a new experimental system, called ELS-LEED, which allows to measure the energy losses with contemporarily high energy and high momentum resolution [28]. From ELS-LEED measurements it is therefore possible to obtain structural information about the geometrical order at the surface, and contemporarily about frequency and dispersion of surface excitations like phonons, plasmons, etc. In particular the dispersion of the surface plasmon can be measured by ELS-LEED with a better momentum resolution than with conventional HREEL spectrometers. In a HREELS system the resolution in q space is in fact determined by the angular acceptance of the spectrometer (about 1.5° for both monochromator and analyzer) and by the geometry of the experiment. For high impact energies and big deflection angles, the window in momentum space over which the data are integrated can therefore become very large and even comparable to the range over which the plasmon dispersion takes place, determining artifacts in the observed dispersion especially if the inelastic cross section of the losses varies rapidly in such a range [29]. On the other hand,

in a ELS-LEED experiment the position in momentum space is changed by an electronic deflection of the electron beam, allowing a better momentum resolution, limited by the quality of the crystal under investigation.

In Fig.2.1 the structure of ELS-LEED is schematically represented. The electron beam, coming from a heated tungsten filament, is focalized into a 127° cylindrical condenser (the monochromator) and it is then accelerated to the selected primary energy. Next, the beam goes through the SPA-LEED octupole, where it is deflected to select the desired momentum transfer and it is finally scattered off the surface. The diffracted electrons are selected in energy by a 127° cylindrical analyzer (identical to the monochromator) and are then counted by a channeltron.

In order to switch quickly between the different measuring possibilities, both octupole and analyzers are controlled by computer, while the voltages necessary for scanning energy and momentum are generated by a 24-bit digital to analog converter.

Without applying any deflection voltage, both incident and deflected beam form a fixed angle of 6° respect to the normal to the surface plane.

The energy and the wavevector parallel to the surface (q_{\parallel}) are conserved, so that:

$$\begin{cases} E_{loss} = E_i - E_s \\ \hbar q_{\parallel} = k_s \sin \Theta_s - k_i \sin \Theta_i \end{cases} \quad (2.1)$$

where k_i and k_s are the wavevectors of the incident and of the scattered electrons, respectively.

The momentum resolution of ELS-LEED, as determined from the width in momentum space of the (00) diffracted peak on a Si(111) surface, is 0.004 \AA^{-1} , but it is generally limited by the quality of the surface [28]. In the present experiments we had a momentum resolution of 0.04 \AA^{-1} for a commercial Ag(111) single crystal, of 0.02 \AA^{-1} for a non-commercial Ag(110) crystal and of 0.04 \AA^{-1} for the thin Ag layers deposited on Si(111). In spite of the limited improvement in the momentum resolution compared to grazing angle conventional EELS, which has typically an integration window in momentum space of about $0.04 \div 0.08 \text{ \AA}^{-1}$, the dispersion of the data points is greatly reduced in the present case because of the electronic deflection system of ELS-LEED, which is much more precise than the mechanical displacement of the monochromator necessary by HREEL spectrometer.

The best energy resolution obtainable with our ELS-LEED is about 4 meV, but for the present experiment it was tuned to 20 meV to improve

the signal to noise ratio of the losses. During the study of Ag thin layers the energy resolution was further reduced to 30 meV, because of the low intensity in the loss peaks.

2.2 Inelastic scattering of electrons

The complete understanding of the inelastic scattering process at a surface requires knowledge about the nature of the interaction between the incoming electrons and the vibrating atoms in the solid. This is a complex problem in general, since the electron interacts strongly with the substrate. Nevertheless, a rather simple mathematical approach is possible for inelastic scattering in long-range potentials [27], as the dominant contribution to inelastic scattering process comes from elastic reflection of the incident electron beam via the interaction with the crystal potential, combined with small-angle inelastic scattering due to the excitation of electron-hole pairs or collective modes.

The inelastic event occurs far from the surface, so that an electron in the vacuum above the crystal senses the long-range electric field. This interaction produces small-angles scattering typically more intense than the scattering observed at large deflection angles. Since the long-range electric field of the incident electron interacts with the fluctuating dipolar field associated with the induced surface charges, such process is normally called "dipole scattering".

The spatial extension of the dipole field increases exponentially with decreasing q_{\parallel} . Accordingly, the inelastic scattering cross section is peaked along the forward direction, so that the scattering intensity is stronger at angles close to the specular direction, forming a so called "dipole lobe".

On the other hand, if the loss is determined by the strong forces operating during the impact of the electron with the ion cores, also large deflection angles are possible. For this regime, called "impact scattering", it is necessary to turn to a fully microscopic calculation to describe the cross section theoretically.

Within the dipole scattering approximation it is possible to obtain a simple form for the cross section, without needing a microscopic calculation of the electron-substrate interaction. The scattering process can be described using the Born approximation of a quantum mechanical scattering theory and the differential cross section of an electron inelastically scattered from a flat surface can be written as [27, 30]:

$$\frac{dS}{d\omega d\Omega} \propto \frac{1}{\cos \Theta_i} \cdot \frac{k_s}{k_i} \cdot \frac{P(\mathbf{q}_{\parallel}, \omega)}{q_{\parallel}^2} \cdot \frac{|v_{\perp} q_{\parallel} (R_s + R_i) + i(R_s - R_i)(\omega - \mathbf{v}_{\parallel} \cdot \mathbf{q}_{\parallel})|^2}{[v_{\perp}^2 q_{\parallel}^2 + (\omega - \mathbf{v}_{\parallel} \cdot \mathbf{q}_{\parallel})^2]^2} \quad (2.2)$$

where v_{\parallel} and v_{\perp} are the parallel and normal components of the velocity of the incident electrons with respect to the plane of the surface. The quantities $R_i (= R_{E_i})$ and $R_s (= R_{E_i - \hbar\omega})$ represent the complex reflection amplitudes, respectively before and after the energy loss, as schematically shown in Fig.2.2. Since the energy loss is caused by a long range interaction occurring far from the surface, it is decoupled from the eventual elastic reflection and it may take place either before or after the elastic scattering. The two events are coherent and will interfere with each other.

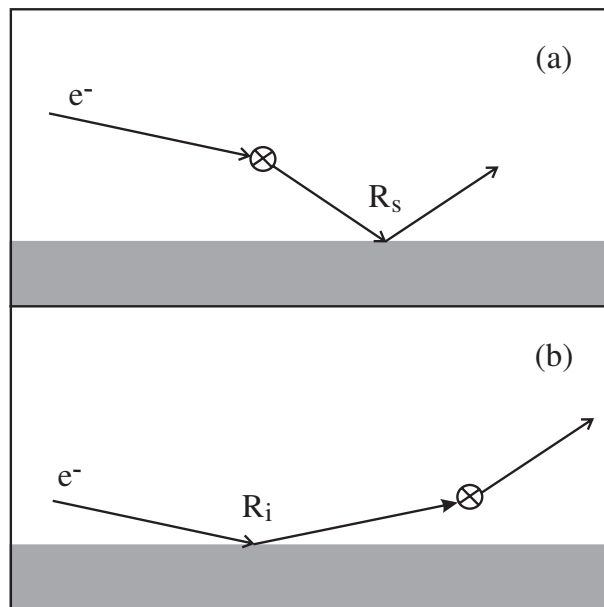


Figure 2.2: Possible loss events in dipole scattering. The loss may take place before the impact with the surface (a) or after it (b).

The function $P(\mathbf{q}_{\parallel}, \omega)$ describes the effects of the charge density fluctuations inside the crystal and contains information on the physics of the surface region.

For small loss energy and scattering angles, we can assume $R_s \approx R_i$ and we obtain:

$$\frac{dS}{d\omega d\Omega} \propto \frac{1}{\cos \Theta_i} \cdot \frac{k_s}{k_i} \cdot \frac{|R_i|^2 P(\mathbf{q}_{\parallel}, \omega)}{[v_{\perp}^2 q_{\parallel}^2 + (\omega - \mathbf{v}_{\parallel} \cdot \mathbf{q}_{\parallel})^2]^2} \quad (2.3)$$

All factors of this expression, except for $P(\mathbf{q}_{\parallel}, \omega)$, are fully determined or directly measurable.

The quantity $P(\mathbf{q}_{\parallel}, \omega)$ is related to the loss function $g(\mathbf{q}_{\parallel}, \omega)$ defined in eq.(1.12) by:

$$Im g(\mathbf{q}_{\parallel}, \omega) = \frac{P(\mathbf{q}_{\parallel}, \omega)}{|\mathbf{q}_{\parallel}|} \quad (2.4)$$

In the small q_{\parallel} limit we have seen (eq.(1.14)) that

$$Im g = Im \left(\frac{\epsilon - 1}{\epsilon + 1} \right) \quad (2.5)$$

so that eq.(2.3) becomes proportional to q_{\parallel} and vanishes at $q_{\parallel} = 0$. At larger values of q_{\parallel} the energy loss intensity will have a maximum at the so called "surfing condition":

$$\omega = \mathbf{v}_{\parallel} \cdot \mathbf{q}_{\parallel} \quad (2.6)$$

This condition is satisfied when the electron velocity parallel to the surface v_{\parallel} equals the phase velocity ω/q_{\parallel} of the surface excitation responsible for the surface scattering process and occurs generally near to the specular direction.

2.3 Elastic diffraction of electrons

The elastic diffraction of slow electrons (LEED) is a standard diffraction technique [25], used to check the crystallographic quality of a surface. The condition of the occurrence of an "elastic" Bragg spot is given by:

$$\mathbf{K}_{\parallel} = \mathbf{k}_{\parallel s} - \mathbf{k}_{\parallel i} = \mathbf{G}_{\parallel} \quad (2.7)$$

i.e. the scattering vector component parallel to the surface must equal a vector of the two dimensional surface reciprocal lattice \mathbf{G}_{\parallel} . The LEED pattern gives an image of the surface reciprocal net. For the component \mathbf{k}_{\perp} , perpendicular to the surface, no Bragg condition applies, so that the well known Ewald construction can be extended to a 2D problem by attributing to every point of the two-dimensional reciprocal lattice a rod normal to the surface, as shown in Fig.2.3.

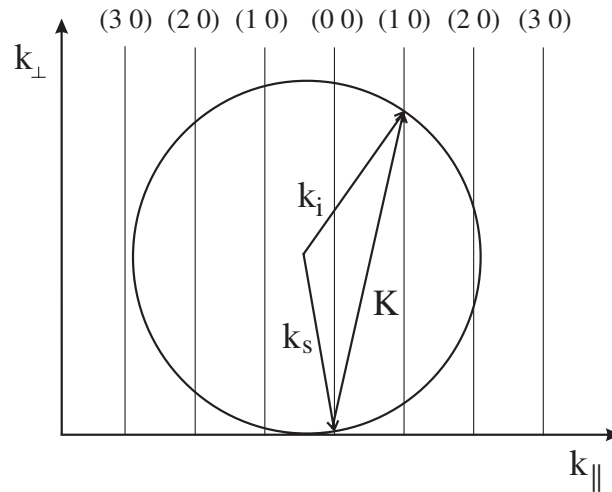


Figure 2.3: Ewald's construction for elastic scattering on a 2D surface lattice.

The mere existence of a sharp spot pattern implies the existence of a well-ordered surface and provides direct information about the symmetry of the substrate. Additional information can be obtained by studying the variation of the diffracted intensity across the width of a single spot, the so called "spot profile" [26, 31]: any deviation from perfect 2D periodicity will in fact modify the reciprocal lattice rods. Broadening and splitting will appear as one varies k_{\parallel} . A splitting always originates from a superperiodicity with a period given by the inverse of the splitting distance in reciprocal space. A broadening has the same origin, but indicates a lack of long range order and the angular half width will then be a measure of the average size of islands or superstructures.

Additional information is available from the impact energy dependence of the spot shape. Any arrangement within one layer will produce a spot shape independent of energy, while a structure involving several layers like the presence of surface steps on a single crystal surface will produce a periodic change of profile with energy. From this kind of analysis it is possible to quantitatively study the roughness of homogeneous surfaces [32].

A detailed understanding of the intensity of a LEED pattern involves the complex problem of describing multiple scattering within the topmost atomic layers of a crystal. Due to the strong scattering of low energy electrons, multiple scattering events are important for a full computation of a LEED pattern.

Nevertheless a simple treatment of the surface scattering process within the framework of single scattering events, known as kinematic approximation, yields insight into the most important features of scattering at surfaces: the spot position is strictly evaluated within the kinematic approximation and the spot profile analysis is still valid.

2.4 Technical details

2.4.1 The chamber

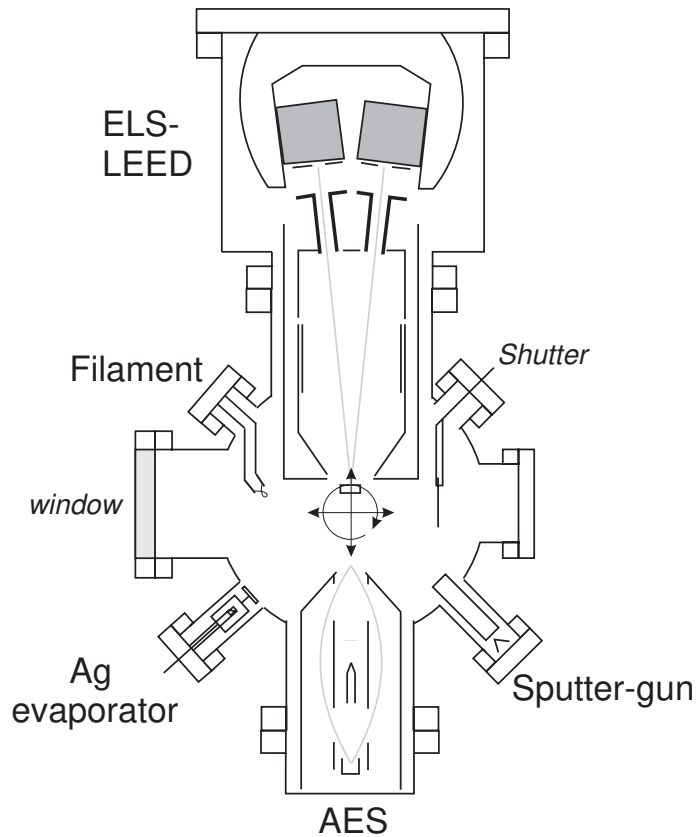


Figure 2.4: A schematic view of the chamber.

The Ultra High Vacuum (UHV) chamber used in the present work is schematically represented in Fig.2.4 and contains the ELS-LEED spectrometer described in section 2.1, a sputter gun used to prepare Ag surfaces, the cell for

the evaporation of metal atoms and an Auger Electron Spectrometer used to check the presence of contamination on the surface and also to calibrate the thickness of the K and Ag layers. For the preparation of K layers a commercial getter source (SAES getters) has been inserted into the chamber. The basic pressure of the chamber is 5×10^{-10} mbar obtained by a standard UHV pumping system. The sample-holder [33] allows to cool the crystal with liquid nitrogen to about 90 K and to heat it with a tungsten filament placed in the back of the crystal or by direct current. The sample is electrically isolated from the copper sample-holder by a sapphire plate. The temperature of the crystal is measured by a NiCr-Ni thermocouple placed in thermal contact with the sample.

2.4.2 Preparation of the Ag surfaces

The experiment on clean Ag surfaces has been performed on a commercial (111)-oriented Ag monocrystal and on a Ag(110) crystal which was polished chemo-mechanically in our laboratory of Hannover, showing finally a surface of high order with a reduced mosaic spread than a commercial crystal. The surfaces were prepared by several cycles of argon ion sputtering and annealing at a temperature of 650 K until no traces of impurities could be detected by Auger electron spectroscopy.

2.4.3 K induced reconstruction of the Ag(110) surface

Alkali metal adsorption on Ag(110) induces long range missing row reconstruction already at very small concentrations [34]. The reconstruction is known to be thermally activated [35], with a critical temperature between 150 K and 250 K, depending also on the alkali metal coverage.

Potassium was evaporated from a well outgassed commercial getter source at a sample temperature of 300 K to study the reconstructed phases and keeping the crystal at 100 K to inhibit such reconstructions.

The evaluation of the K coverage was obtained by Auger Electron Spectroscopy (AES) comparing the evaporation time with the ratio of the K transition at 252 eV with the Ag transition at 352 eV, as reported in Fig.2.5. The completion of the first K monolayer, corresponding to $\Theta_K = 1$ ML, has been determined by the position of the change in the slope of the dependence of the AES peak ratio vs. the exposure time, which occurred for a ratio of the AES intensities $I_K/I_{Ag} = 0.7$ after an exposure time of 30 min. Since

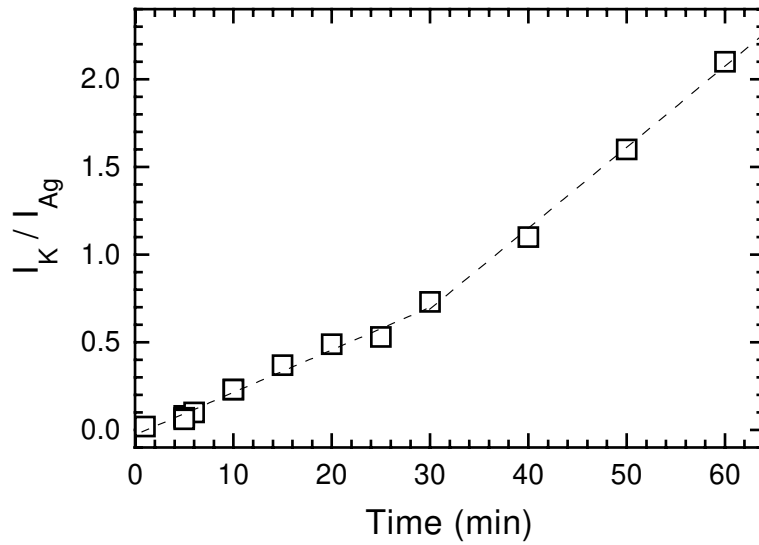


Figure 2.5: Ratio of the intensities of the K transition at 252 eV and of the Ag transition at 352 eV versus exposure time, as obtained by AES.

the metallic radius of K is 2.32 Å, $\Theta_K = 1$ ML corresponds to a coverage of 0.64 K atoms per Ag(110) unit cell, i.e. to 5.4×10^{14} atoms cm^{-2} .

2.4.4 Ag thin layers on Si(111) 7x7

The Si(111) crystal, protected with a layer of oxide, was cut manually to fit the sample-holder shape and inserted into the chamber. The surface oxide was then removed in UHV by heating the crystal to a temperature of 1200°C while keeping the pressure in the chamber lower than 2×10^{-9} mbar. The crystal was then cooled slowly down and annealed at 600°C for some minutes in order to allow for the surface diffusion necessary to build a sharp 7×7 surface reconstruction.

Ag was evaporated by electron bombardment from a graphite crucible, while keeping the sample either at a temperature of 100 K or at room temperature. The amount of evaporated Ag was controlled with a quartz crystal microbalance calibrated against the AES measurements.

The frequency of the quartz microbalance depends linearly on the mass density of the material evaporated on it:

$$\Delta f = C\rho \quad (2.8)$$

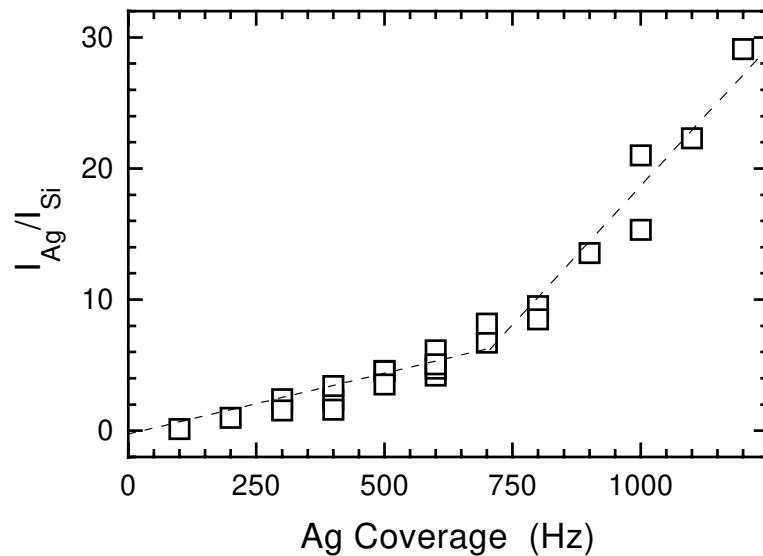


Figure 2.6: Ratio of the intensities of the Ag transition at 352 eV and of the Si transition at 92 eV, as obtained by AES, versus the variation of frequency of the microbalance.

where C is a constant and ρ is the density of silver in mass units [36]. In the present case 1ML of silver deposited on the microbalance corresponds to a variation of the frequency $\Delta f = 56.2\text{Hz}$. As the quartz oscillator is placed much nearer to the evaporator than the crystal, the flux of Ag atoms will be smaller at the sample position. A calibration in this respect has therefore been performed by placing a second microbalance at the crystal position and comparing the frequency variations of the two oscillators as reported in ref. [36]. The result of such measurement was that 1 ML of Ag on the sample corresponds to 11.7 ML of Ag on the microbalance. 1ML of Ag on the crystal corresponds then to a variation of frequency of

$$\Delta f^* = 56.2 \times 11.76 \approx 660\text{Hz} \quad (2.9)$$

A further calibration of the Ag coverage has been done by means of Auger spectroscopy, from the ratio of the Ag transition at 352 eV and of the Si transition at 92 eV, as reported in Fig.2.6. The completion of the first monolayer corresponds to the change in the slope of the AES ratio vs. exposure. Such a change is in good agreement with the evaluation obtained by the quartz oscillator.

Chapter 3

Surface plasmon on Ag surfaces

3.1 Introduction

Surface plasmon dispersion on silver was firstly investigated by HREELS in Marseille by J.M. Layet and coworkers in 1987 [37], while a systematic study of the surface plasmon properties on metal surfaces started some years later by the group of W. Plummer in Philadelphia [15, 38] and by the group of M. Rocca and U. Valbusa in Genova [16, 17, 39]. For Ag surfaces a positive dispersion was reported by all groups and the dispersion was observed to be anisotropic with respect to the crystallographic face and, for Ag(110), also to the crystal azimuth. The origin of the azimuthal anisotropy for Ag(110) was ascribed to the quadratic term by Lee et al. [38] and to the linear term by Rocca et al. [17] while, for Ag(111), Suto et al. [15] excluded the presence of a linear term in the dispersion, contrary to Rocca et al. [40]. Moreover the data for Ag(111) in ref.[40] showed an anomalously large spread for the surface plasmon frequency near to $q_{\parallel} \approx 0$ and the values for surface plasmon damping reported by the different laboratories differ by a factor of three.

These findings indicated that further investigation of the electronic excitation spectrum of Ag surfaces was necessary, possibly improving the momentum resolution, determined by the angular acceptance of the HREEL spectrometer. A finite angular acceptance is in fact one of the major limiting factor for studying surface plasmon dispersion and can also determine anomalies in the dispersion [29].

As discussed in section 2.1, the ELS-LEED spectrometer allows to greatly improve the quality of the energy loss measurements. In this work such a

technique has been applied to the study of surface plasmon dispersion and damping on Ag(111) and Ag(110) [41, 42], showing that the linear term of the dispersion is anisotropic, while the quadratic term is relatively large and the same for both surfaces. These results confirm therefore the interpretation of the data of the Genova group with respect to the anisotropy, while the magnitude of the quadratic term is nearer to the result of the Philadelphia group. The quadratic term remains however anisotropic with respect to crystal face as it is reported to be nearly absent for Ag(001) [16].

The reinvestigation of Ag surface plasmon by ELS-LEED allowed moreover to evidence the presence of the multipole plasmon mode also for Ag [43]. Such mode is particularly evident near to $q_{\parallel} = 0$, where the dipole scattering intensity, by which the ordinary surface plasmon is excited, has a minimum.

3.2 Data presentation

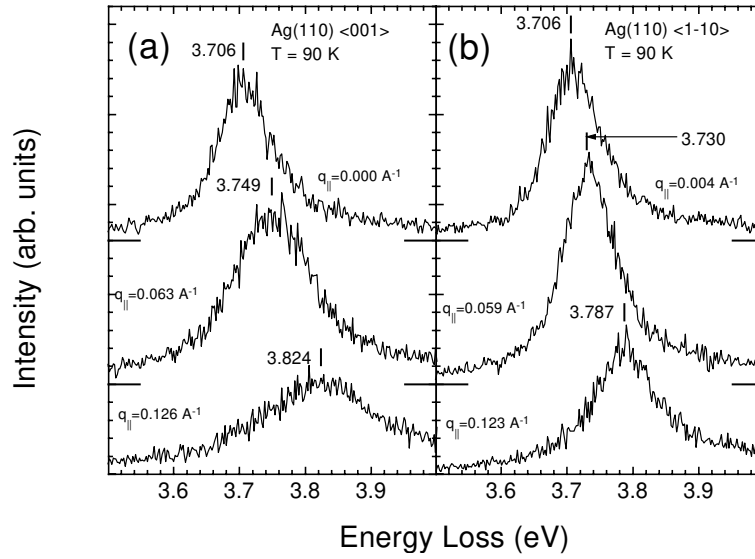


Figure 3.1: Energy loss spectra for Ag(110) recorded at $E_i = 65.4$ eV for the directions (a) $\langle 100 \rangle$ and (b) $\langle 1\bar{1}0 \rangle$.

Sample spectra recorded for Ag(110) along the two high symmetry crystallographic directions $\langle 001 \rangle$ and $\langle 1\bar{1}0 \rangle$ at different q_{\parallel} are shown in Fig.3.1, while a schematic view of the Ag(110) surface is reported in Fig.3.2. Only

one sharp energy loss peak is present in the loss spectra, corresponding to the excitation of the surface plasmon mode.

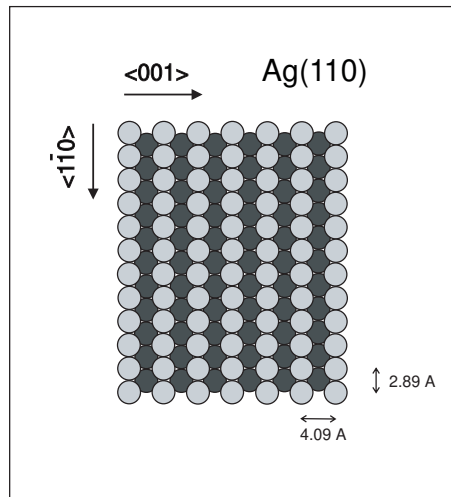


Figure 3.2: Schematic representation of the (110) surface of Ag. The two high symmetry crystallographic directions $\langle 001 \rangle$ and $\langle 1\bar{1}0 \rangle$ are indicated.

The surface plasmon frequency $\hbar\omega_s$ has been inferred from the position of the maximum of the loss peak, determined by a gaussian fit after subtraction of an inelastic linear background due to electron-hole pair excitations.

The transferred momentum parallel to the surface, q_{\parallel} , can be calculated from the angles of incidence Θ_i and of scattering Θ_s by applying energy and momentum conservation (eq.(2.1)). Such angles are selected by applying a given deflection voltage to the octupole.

As one can see from Fig.3.1, the dependence on q_{\parallel} of both the energy and the width of the peaks is anisotropic with respect to crystal face and, for Ag(110), also to crystal azimuth, as for large q_{\parallel} the peaks of Ag(110) are shifted to higher energies and are broader along $\langle 001 \rangle$ than along $\langle 1\bar{1}0 \rangle$, while those of Ag(111) are in-between.

Sample spectra recorded for different q_{\parallel} and temperatures for Ag(111) are reported in Fig.3.3. They show that the energy loss decreases with increasing temperature while the damping increases, confirming the behaviour previously observed on Ag(001) [44].

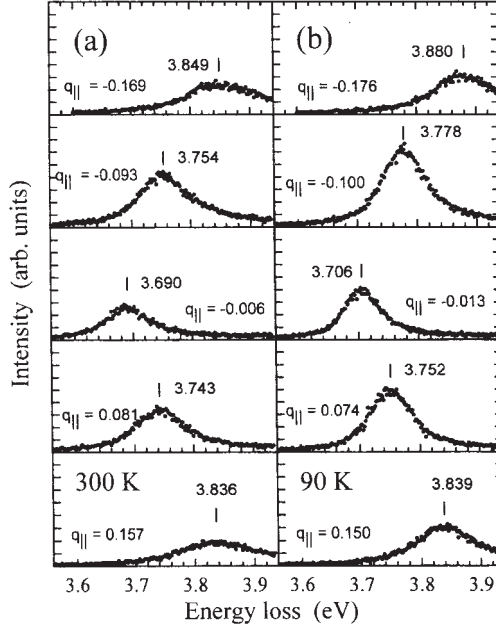


Figure 3.3: Energy loss spectra for Ag(111) recorded at $E_i = 20.1$ eV for (a) T=300 K and (b) T=90K.

3.3 Surface plasmon dispersion

The values of the maximum of the energy loss peak ($\hbar\omega_s$) are reported versus $q_{||}$ in Fig.3.4(a) for Ag(110) along the two high symmetry directions and in Fig.3.4(b) for Ag(111). The data have been recorded at a temperature T of 100 K. Different symbols in Fig.3.4(a) refers to two different sets of data, measured at two different impact energies ($E_i = 65.4$ eV and $E_i = 16.5$ eV). As one can see the different sets of data overlap perfectly. The insets show the region near to $q_{||} = 0$ to highlight the initial linear behaviour for both surfaces and the azimuthal anisotropy of the Ag(110) data.

The solid curves in Fig.3.4 are the results of the parabolic best fit:

$$\hbar\omega(q_{||}) = \hbar\omega_s + Aq_{||} + Bq_{||}^2 \quad (3.1)$$

The best fit parameters and the uncertainties were determined by the χ^2 method, using the MINUIT computing routine, which requires that the uncertainty on $q_{||}$ is reported on the dependent variable. In the present case an error as small as ± 2.5 meV had to be assumed to obtain unitary statistical

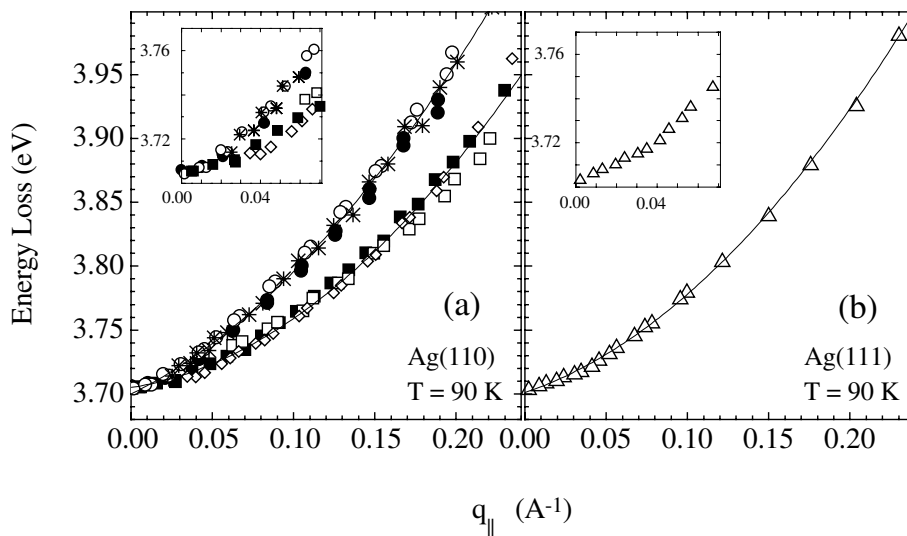


Figure 3.4: Surface plasmon dispersion with q_{\parallel} at $T=90$ K for (a) Ag(110) along $\langle 1\bar{1}0 \rangle$ (squares and diamonds) at $E_i = 65.4$ eV and $\langle 001 \rangle$ (circles and stars) recorded at $E_i = 65.4$ eV (circles) and $E_i = 16.5$ eV (stars) and (b) Ag(111) at $E_i = 20.1$ eV. Solid lines are the best-fit curves for the data. The different symbols in (a) refer to different sets of measurements. Filled and open symbols in (a) refer to different sets of measurements recorded for the same electron impact energies. The insets are an enlargement of the low q_{\parallel} limit.

variance, because of the good quality of the data. The results are shown in Table 3.1.

As one can see, the surface plasmon frequency $\hbar\omega_s$ agrees within experimental error for all the three cases. It is however slightly lower than the value reported for HREELS measurements for Ag(001) (3.710 eV at $T = 100$ K [44]) and Ag(111) (3.708 eV at $T = 100$ K [40]). The reason for this discrepancy is not clear, but it is interesting to note that the ELS-LEED values are in better agreement with the optical value of $\hbar\omega_s = 3.665$ eV ref.[10]. The explanation for this discrepancy is probably connected to the different temperature dependence of $\hbar\omega_s$ for the different Ag surfaces as will be shown in the following paragraphs.

All curves show the same quadratic coefficient, whereas the linear term is different. As the linear term of the dispersion is determined by the electronic properties of the material at the solid-vacuum interface (see section 1.1),

Table 3.1: Surface plasmon dispersion coefficients derived by χ^2 analysis for the data recorded at T=100 K.

Face	Azimuth	$\hbar\omega_s(0)$ (eV)	A (eV Å)	B (eV Å ²)
(110)	< 001 >	3.700 ± 0.002	0.62 ± 0.04	3.4 ± 0.3
(110)	< 110 >	3.705 ± 0.003	0.19 ± 0.04	3.4 ± 0.2
(111)		3.701 ± 0.001	0.43 ± 0.02	3.4 ± 0.1

the reported results confirm the surface origin of the anisotropy in surface plasmon dispersion, as already reported by Rocca et al. [40]. Thanks to the high momentum resolution of ELS-LEED, the errors on the coefficients have been reduced in the present study by a factor two to four.

On Ag(111) the linear term of the dispersion is nearly identical with the previous determination, while the quadratic term is slightly larger (it reads 2.7 ± 0.5 eV Å² in ref.[40]).

On Ag(110) the dispersion parameters differ from the results obtained by Rocca et al. [17], as the linear term come out to be smaller and the quadratic term larger. Indeed the ELS-LEED values compare better with the HREELS results of Lee et al. [38] although the better momentum resolution of the present experiment rules out the conclusion that the term responsible for the anisotropy might be the quadratic one.

The quadratic term of the dispersion is generally assumed to be connected to bulk properties and it is therefore expected to be isotropic. The results for Ag(111) and Ag(110) reported in Table 3.1 look like to confirm this idea. Nevertheless the surface plasmon dispersion on Ag(001), as obtained by previous HREELS measurements [16, 29], shows a nearly purely linear dispersion. A comparison of the ELS-LEED results for Ag(110) and Ag(111) with the dispersion on Ag(001) is reported in Fig.3.5. As one can see the discrepancy is far too large to be of experimental origin, due to the different experimental method (HREELS vs. ELS-LEED). The anomalous behaviour of Ag(001) indicates therefore that the situation is more complicated and that the quadratic term of the dispersion must be in some way influenced by surface effects. Such problem will be discussed at length in section 4.3.1.

According to Liebsch's theory, the parameter D_s defined in eq. (1.21) is

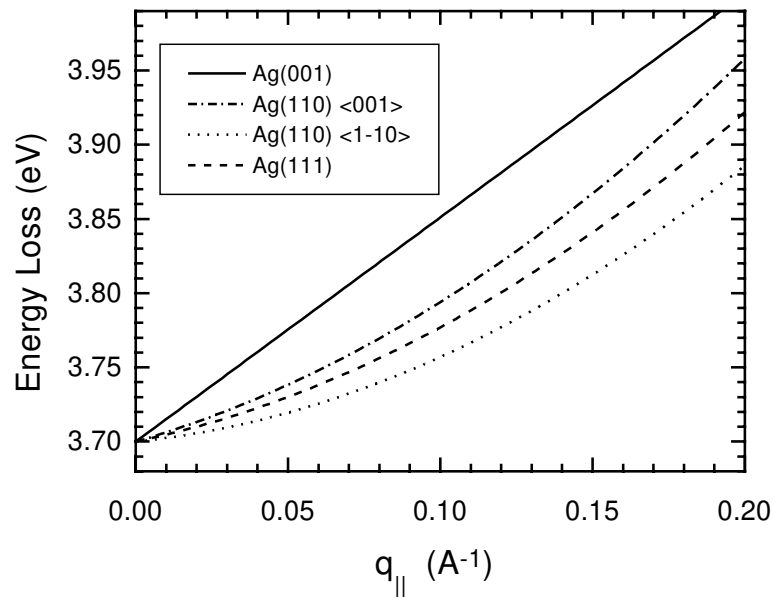


Figure 3.5: Surface plasmon dispersion curves measured on the different low index Miller surfaces of Ag at $T=100$ K. The curves for Ag(110) and Ag(111) are the best fit obtained by the present ELS-LEED measurements, while the dispersion on Ag(001) was measured by HREELS [16].

connected to the linear term of the surface plasmon dispersion (A) by:

$$\frac{A}{\omega_s} = -\frac{1}{2}D_s \quad (3.2)$$

so that $D_s = -0.34 \text{ \AA}$ for Ag(110) $\langle 001 \rangle$, $D_s = -0.10 \text{ \AA}$ for Ag(110) $\langle 1\bar{1}0 \rangle$ and $D_s = -0.23 \text{ \AA}$ for Ag(111). The negative sign of D_s indicates that the distance z_d , defined in section 1.2.2 and schematically shown in Fig.1.4, is negative, i.e. that the polarizable medium describing the d electrons lies inside the geometric surface. It is interesting to note that the average value of D_s for the two azimuthal directions of Ag(110) is $\bar{D}_s = 0.22 \text{ \AA}$, thus coinciding with the value of D_s on Ag(111). This identity means that both surfaces can be described by the same average value of z_d , while Ag(001) seems again to behave differently.

The present reinvestigation of surface plasmon dispersion on Ag(111) and Ag(110), thanks to the better momentum resolution of ELS-LEED, allows

us to conclude that $\omega_s(q_{\parallel} = 0)$ is the same for the three low Miller index surfaces of Ag and that the dominant coefficient of the dispersion for small q_{\parallel} is linear and positive, larger for Ag(110) < 001 > than for Ag(111) and for Ag(110) < $\bar{1}\bar{1}0$ >. The quadratic term is the same for the two surfaces and indicates that the anisotropy in the dispersion does not depend on bulk properties.

However the origin of the anisotropy of surface plasmon dispersion among the Ag surfaces is still not clear: it can be possibly connected to the different surface corrugation on the different faces and directions [18] or maybe due to the influence of the electronic band structure of the surface. As we'll see in section 4.3.1, a variation of the surface corrugation does not modify surface plasmon dispersion, so that it is straightforward to conclude that surface plasmon dispersion is mainly determined by the electronic structure at the surface.

3.4 Temperature dependence

In Fig.3.6 is reported the surface plasmon dispersion on Ag(110) and Ag(111) measured at room temperature, while the corresponding dispersion coefficients are shown in Table 3.2. As one can see, for both surfaces the only parameter affected by increasing T outside of experimental errors is $\hbar\omega_s$. The plasmon frequency decreases with T, while the dispersion shift rigidly. A similar result was obtained on Ag(100) [45].

The observed shift in frequency is caused by the thermal expansion of the crystal, which influences both the electron-gas density and the band structure.

Surface plasmon energy is reported versus the temperature of the sample in Fig.3.7(a) for Ag(110) and in Fig.3.7(b) for Ag(111) showing a linear shift with T. Such behaviour can be ascribed to the thermal expansion of the crystal and is a consequence of the linearity of the shift of the bond energies with thermal lattice expansion. The results of a linear fit at $q_{\parallel} = 0$ are reported in Table 3.3, where is compared with the result reported for Ag(001) [44].

As one can see, $\hbar\omega_s(T = 0)$ coincides within error for all the surfaces, while the temperature dependence is slightly larger for Ag(111) than for the other two surfaces thus causing an apparent anisotropy of $\hbar\omega_s$ at T=300 K. The effect is however at the limit of the experimental error.

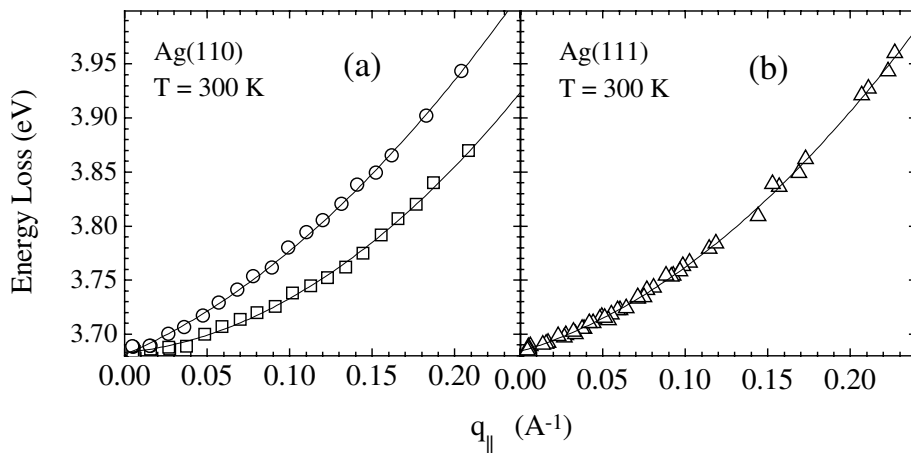


Figure 3.6: Surface plasmon dispersion with q_{\parallel} at $T=300$ K for (a) Ag(110) at $E_i = 65.4$ eV along $\langle 1\bar{1}0 \rangle$ (\square) and $\langle 001 \rangle$ (\circ) and (b) Ag(111) at $E_i = 20.1$ eV. Solid lines are the best fit curves for the data.

Table 3.2: Surface plasmon dispersion coefficients derived by χ^2 analysis for the data recorded at $T=300$ K

Face	Azimuth	$\hbar\omega_s(0)$ (eV)	A (eV \AA)	B (eV \AA^2)
(110)	$\langle 001 \rangle$	3.681 ± 0.002	0.65 ± 0.04	3.1 ± 0.3
(110)	$\langle 110 \rangle$	3.683 ± 0.003	0.14 ± 0.06	3.6 ± 0.3
(111)		3.684 ± 0.002	0.44 ± 0.02	3.3 ± 0.2

3.5 Surface plasmon damping

By analogy with the bulk plasmon case, the lifetime of the surface plasmon is limited by its decay into single particle excitations. Different processes are possible, involving direct intraband transitions inside a single sp -band or $d \rightarrow sp$ interband transitions. Such decay mechanisms can be direct or mediated by the exchange of reciprocal lattice vectors or phonons [2]. The Jellium theory [1] includes obviously only the elastic mechanism involving sp electrons and predicts an infinite lifetime of the plasmon at $q_{\parallel} = 0$ and a linear growth of the loss line with q_{\parallel} , corresponding to the growing phase space into which the surface plasmon can decay.

In a recent paper Ishida and Liebsch [46] showed that for simple metals

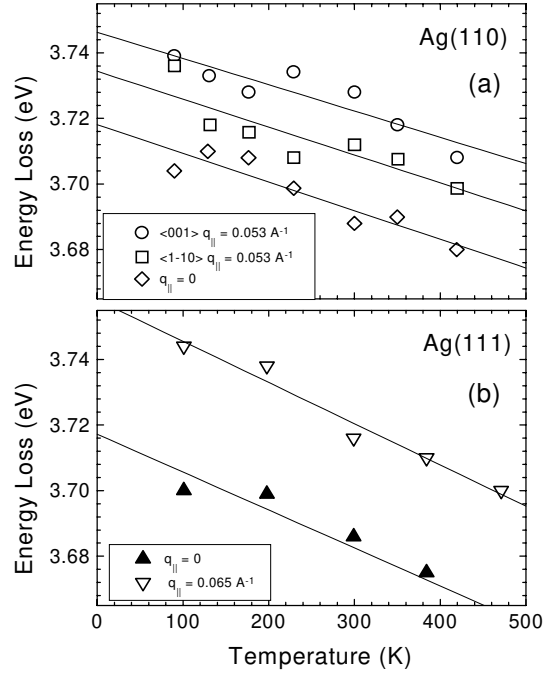


Figure 3.7: Surface plasmon energy $\hbar\omega_s$ versus T (a) for Ag(110) at three different q_{\parallel} and (b) for Ag(111). The solid lines are the best fits of the data.

Table 3.3: Surface plasmon energy versus the crystal temperature: coefficients of the linear fit $\hbar\omega_s(T) = \hbar\omega_s(0) + AT$. The data for Ag(001) are from ref. [44].

Face	$\hbar\omega_s(0)$ (meV)	A (meV K ⁻¹)
(111)	3717 ± 4	-0.121 ± 0.01
(110)	3718 ± 4	-0.087 ± 0.04
(001)	3719 ± 4	-0.094 ± 0.01

the width of the surface plasmon peak at $q_{\parallel} \approx 0$ is a sensitive function of the lattice potential, i.e. it is influenced by the periodic potential of the bulk. The plasmon broadening then takes place via coupling to bulk interband transitions. At larger q_{\parallel} however the plasmon lifetime becomes less sensitive to the bulk lattice potential and the increasing of the damping

is then caused by electron-hole pair excitations in the surface region. In real systems the lifetime of the plasmon is further limited by the scattering against crystallographic defects.

In the present experiment surface plasmon damping has been inferred from the full width at half maximum (FWHM) of the loss peak, after the subtraction of a nearly constant inelastic background due to electron-hole pair excitations and a gaussian deconvolution with respect to energy and momentum resolution:

$$\Delta\hbar\omega_s = \sqrt{(\Delta E_{loss})^2 - (\Delta E_{exp})^2} \quad (3.3)$$

where ΔE_{loss} is the FWHM of the loss peak and ΔE_{exp} takes into account the two independent effects due to the energy and momentum resolution, so that:

$$\Delta E_{exp} = (\Delta E_i)^2 + [\hbar\omega_s(q_{||} + \Delta q_{||}) - \hbar\omega_s(q_{||} - \Delta q_{||})]^2 \quad (3.4)$$

where ΔE_i and $\Delta q_{||}$ are the energy and momentum resolution of the instrument, described in section 2.1.

The so obtained surface plasmon damping is reported versus $q_{||}$ in Fig.3.8 for Ag(110) along $\langle 001 \rangle$ and $\langle 1\bar{1}0 \rangle$ and for Ag(111). The data indicate a flat initial dependence of the FWHM on $q_{||}$ and a stronger increase with $q_{||}$ beyond a critical value $q_{||c}$. On the other hand the damping of the surface plasmon on Ag(100) (also reported in Fig.3.8 for comparison (dashed line)) shows a strong increase with $q_{||}$ already for small values. The value of $q_{||c}$ is the same for all surfaces ($q_{||c} \approx 0.11\text{\AA}^{-1}$), but the slope of the dispersion beyond $q_{||c}$ depends on crystal face.

The result of the linear best fit to the data in Fig.3.8 for $q_{||} < q_{||c}$ and $q_{||} > q_{||c}$ are collected in Table 3.4 and 3.5. As one can see $\Delta\hbar\omega_s(0)$ depends on crystal face and is smaller for Ag(111).

Surface plasmon damping is anisotropic with respect to $q_{||}$ for the different faces and for the azimuthal directions of Ag(110).

As one can see, for $q_{||} < q_{||c}$ a small negative dispersion is observed for both Ag(110) $\langle 1\bar{1}0 \rangle$ and Ag(111), i.e. along close packed directions, confirming in sign but not in magnitude the effect reported for Ag(111) by Rocca et al. [40].

A negative initial dispersion of the FWHM with $q_{||}$, even if small as in the present case, is nevertheless surprising as one would expect a linear positive growth with $q_{||}$, due to the growing phase space at disposition for surface plasmon decay into electron-hole pairs. Beyond $q_{||c}$ the slope of the dispersion

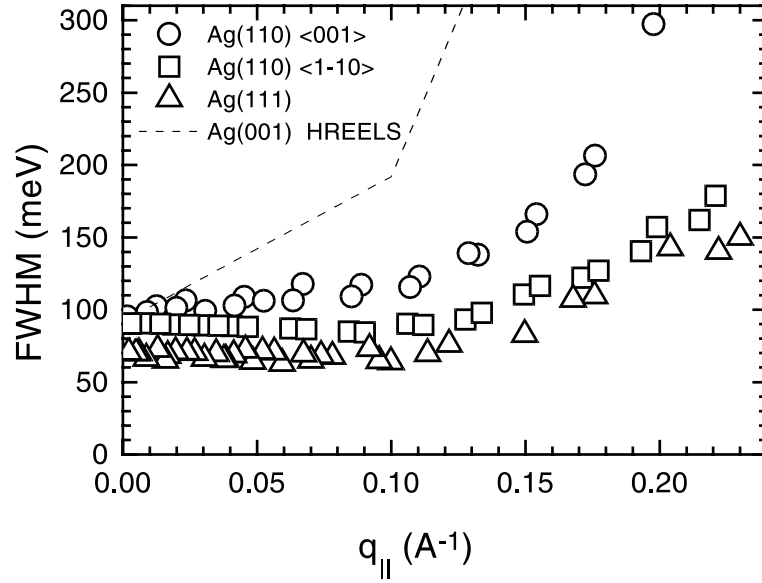


Figure 3.8: Dispersion with $q_{||}$ of the FWHM of the surface plasmon at T=100 K on Ag(110) along $\langle 1\bar{1}0 \rangle$ and $\langle 001 \rangle$ and on Ag(111). The dashed line is the behaviour observed on Ag(001) at T=300 K, from ref.[16].

Table 3.4: Surface plasmon damping parameters versus $q_{||}$ derived by a χ^2 analysis for $q_{||} < 0.11 \text{ \AA}^{-1}$ at T=100 K, from the linear relation $\Delta\hbar\omega_s(q_{||}) = \Delta\hbar\omega_s(0) + Bq_{||}$

Face	Azimuth	$\Delta\hbar\omega_s(0)$ (eV)	B (eV \AA)
(110)	$\langle 001 \rangle$	0.097 ± 0.002	0.20 ± 0.04
(110)	$\langle 1\bar{1}0 \rangle$	0.089 ± 0.001	-0.007 ± 0.015
(111)		0.069 ± 0.001	-0.032 ± 0.004

is strongly anisotropic, indicating that the surface electronic structure must be responsible for the behaviour of plasmon damping and of its anisotropy, but also that the phenomenon is more complicated than assumed so far.

The existence of a link between the anisotropy of surface plasmon dispersion and the anisotropy of surface plasmon damping was indeed suggested by Li et al.[47] in a theoretical paper, starting from the idea that both quantities

Table 3.5: Surface plasmon damping parameters versus q_{\parallel} derived by a χ^2 analysis for $q_{\parallel} > 0.11 \text{ \AA}^{-1}$ at T=100 K, from the linear relation $\Delta\hbar\omega_s(q_{\parallel}) = A + Bq_{\parallel}$

Face	Azimuth	A (eV)	B (eV \AA)
(110)	< 001 >	-0.08 ± 0.04	1.71 ± 0.25
(110)	< 110 >	0.008 ± 0.009	0.80 ± 0.05
(111)		-0.01 ± 0.01	0.71 ± 0.03

are influenced by the electronic band structure at the surface. In this frame the abnormal initial slope of the damping of Ag(001) could be connected to the abnormal frequency dispersion and be due to the presence of the inter-band transition at 3.6 eV at \bar{X} involving filled and empty Shockley states [48, 49] which is nearly degenerate with the surface plasmon frequency.

3.6 Multipole plasmon mode

On a fine scale, the energy loss spectra measured by ELS-LEED on Ag(111) and Ag(110) near to $q_{\parallel} = 0$ show a position of the maximum and a FWHM depending on E_i . Some examples of this anomalous effect are reported in Fig.3.9 for Ag(110). As one can see $\hbar\omega_s$ is 3.71 eV at 16.5 eV, 29.0 eV, 49.4 eV, 53.0 eV and 65.4 eV but it is definitely larger at 17.8 eV and 34.3 eV. The effect is not instrumental and shows therefore that such energy loss spectra are structured, i.e. composed by different unresolved peaks. The weight of the different component seems to depend on impact energy and on scattering geometry.

In Fig.3.10 the dispersion of the energy and of the damping of the loss peaks measured on Ag(110) is reported for an anomalous set of data and for a normal one. As one can see, the data points coincide for large q_{\parallel} , but they deviate significantly near to $q_{\parallel} = 0$. From Fig.3.10(b) we could also note that the larger E_{loss} values correspond to peaks of larger FWHM.

A similar situation occurs for Ag(111). The maximum of the losses is reported in Fig.3.11 for two values of E_i and compared with the data obtained from a previous HREELS investigation [40]. As one can see, at small q_{\parallel} , E_{loss} depends again on the scattering conditions and, as shown in Fig.3.11(b), the

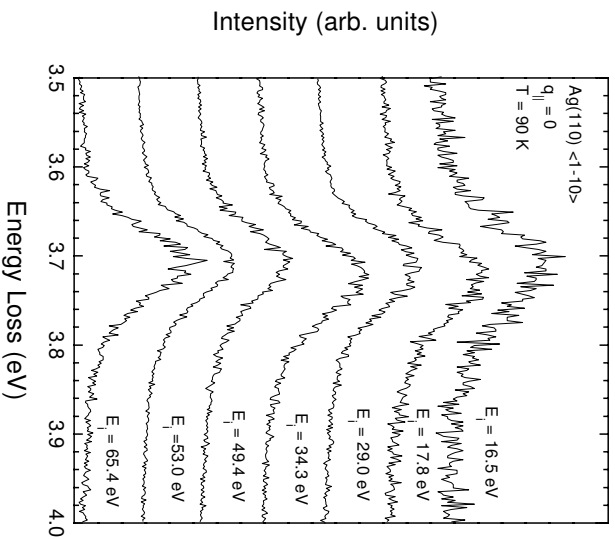


Figure 3.9: Energy loss spectra for Ag(110) at different impact energies. The position of the maximum and the width of the peaks depends on E_i , showing the complex nature of the losses.

FWHM of the losses is larger where E_{loss} is anomalously high.

In the upper panels of Fig.3.12 ELS-LEED spectra recorded at $q_{\parallel} \approx 0$ for two different impact energies are compared, for (a) Ag(110) and (b) Ag(111). The intensity of the spectra has been normalized to the low frequency edge of the loss peak. The spectra reported in the lower panel have been obtained by subtracting the two peaks of the upper panels: in both cases a well defined peak is found, centered at about 3.74 eV.

The observed anomaly in the peaks cannot be due to the excitation of the bulk plasmon, as it would be expected at $\hbar\omega_p = 3.78$ eV [50] (arrow in Fig.3.12(b)) while no intensity is present at that E_{loss} value in the difference spectra. Similarly it cannot be due to an interband transition as then much broader peaks would be expected [39]. Finally it cannot be due to an elastic reflectivity structure [45], as that effect can be easily discriminated by changing the impact energy.

The relevant excitation involved in the observed anomalies must have a frequency in-between ω_s and ω_p . Such an extra feature is indeed present for simple metals and corresponds to the multipole mode ω_m (defined in section

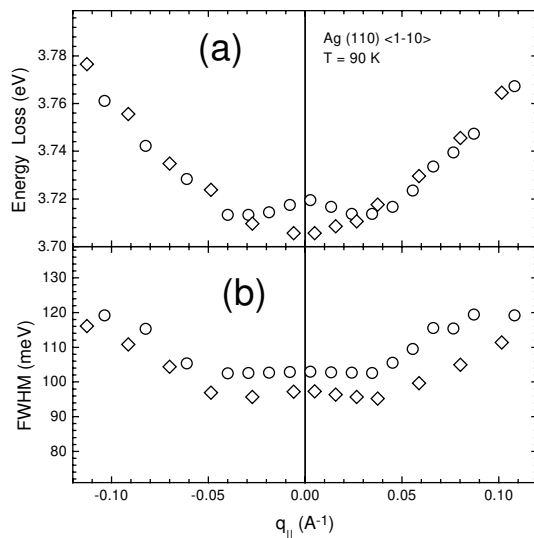


Figure 3.10: (a) Energy losses and (b) FWHM of the loss peaks versus $q_{||}$ for Ag(110). \diamond : $E_i = 65.4$ eV, \circ : $E_i = 16.5$ eV.

1.2), which was observed by HREELS at $\omega_m \approx 0.8\omega_p$ for alkali metal films [12].

Recently [51] the multipole plasmon mode has been observed also for alkali metal overlayers on Al(111) using photoyield spectroscopy, a technique particularly suited for this measurements, because the use of photons suppresses the ordinary surface monopole mode while the bulk plasmon is not yet fully developed on a thin overlayer.

The existence of the multipole mode for simple metals was the object of a prolonged theoretical debate as it can be sustained by the surface only when the ground state electronic properties are realistically described by the density functional scheme [52, 53, 54].

For Ag the very existence had been questioned because of the extreme closeness of surface and bulk plasmon frequency and because of the extra broadening caused by bulk damping processes.

In the present experiment the mode has been evidenced thanks to the different excitation mechanism: dipole scattering for the surface plasmon and impact scattering for the multipole mode: the multipole mode is in fact visible at $q_{||} \approx 0$, where the cross section of the dipole scattering has a minimum, and, also in the case of Ag, it lies between ω_s and ω_p [43].

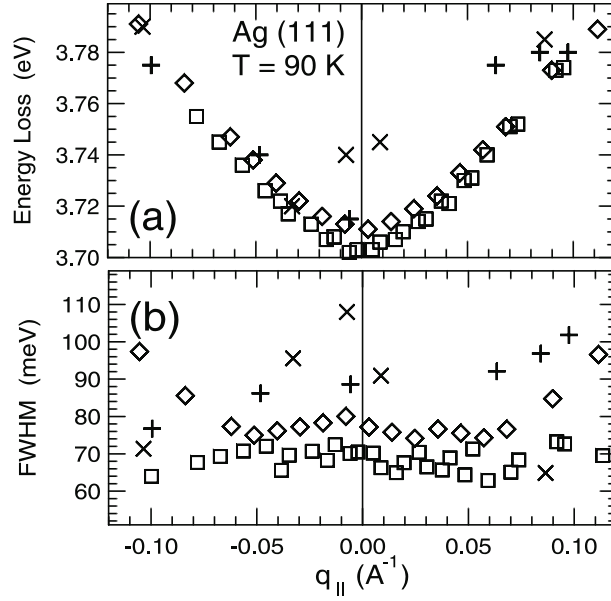


Figure 3.11: (a) Energy losses and (b) FWHM of the loss peaks versus $q_{||}$ for Ag(111). ELS-LEED data \square $E_i = 20.1$ eV, \diamond $E_i = 51.5$ eV; HREELS data (from ref.[Yibing]): \times $E_i = 15.0$ eV, $+$ $E_i = 10.7$ eV.

Very recently Liebsch [55], stimulated by the present data, performed a calculation for the multipole mode on Ag. At variance with our results he found no multipole plasmon at 3.74 eV. A mode with multipole character showed up on the contrary above the bulk plasma frequency near $0.8 \times 9.0 = 7.2$ eV, where 9.0 eV is the bulk plasma frequency of the 5s electrons.

The negative conclusions of A. Liebsch however does not affect our experimental conclusions that:

- 1) one extra sharp mode is present slightly above ω_s ;
- 2) such mode is excited by a different mechanism than dipole scattering and therefore cannot be a second surface plasmon, nor due to excitation of electron-hole pairs which are mostly likely excited via the long range Coulomb field.

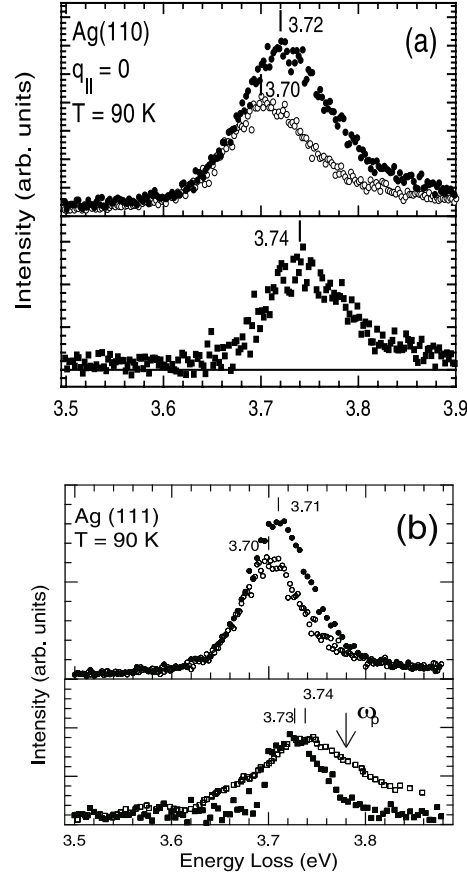


Figure 3.12: Upper panels: comparison of the losses observed under different scattering conditions for $q_{\parallel} = 0$ for: (a) Ag(110) and (b) Ag(111). The spectra are normalized to the low-frequency leading edge. Lower panels: difference spectra obtained by subtraction of the spectra in the upper panel. In both cases a well defined peak centered at about 3.74 eV is obtained. Such a peak is compared in (b) with an anomalous HREELS spectrum (\square) recorded at $E_i = 15.0$ eV. Such spectrum is probably dominated by the multipole plasmon. The arrow indicates the frequency of the bulk plasmon $\hbar\omega_p = 3.78$ eV.

Chapter 4

K adsorption on Ag(110)

4.1 Introduction

Adsorption of small amounts of alkali metal atoms on the (110) surfaces of Ni, Cu, Pd and Ag is known to induce their reconstruction into $(1 \times n)$ missing row structures [34, 35, 56, 57, 58, 59]. Controversial models exist, however, for the mechanism of the transformation, while the effect of the reconstruction on surface electronic excitations has been never reported so far.

In the present work, the influence of K adsorption on the surface geometric structure and on the collective electronic excitations of Ag(110) has been studied by ELS-LEED. Ordered $(1 \times n)$ missing row reconstructions and disordered adsorption have been investigated, finding that an extended surface reconstruction takes place already at 3% K coverage, generating a (1×3) missing row structure. From the spot profile analysis of the LEED peaks it follows that a long range correlation among K adatoms is present along the $\langle 1\bar{1}0 \rangle$ direction on the reconstructed surface, implying that the reconstruction is stable also far away from the adsorption sites of the K adatom and that K islands form.

With increasing K coverage the distance between two K adatoms along $\langle 1\bar{1}0 \rangle$ decreases and the adsorption sites become correlated also along $\langle 001 \rangle$, underlying the very active role played by K in surface reconstruction.

Moreover, from the energy loss measurements, it has been concluded that Ag surface electronic excitations are strongly affected by K adsorption [19] and it has been possible to demonstrate that the special behaviour of surface

plasmon dispersion on Ag(001) is due to the presence of interband transitions which nearly match the surface plasmon energy.

Collective electronic excitations of disordered K films at higher K coverage have been also studied, finding that in the long wavelength limit the Ag surface plasmon energy shifts upwards with increasing K coverage, contrary to what expected from classical dielectric theory, while the dispersion decreases. A K-induced loss sets in above half a monolayer coverage and a collective K induced mode is observed above 1ML.

4.2 Surface Structure

Alkali metal induced missing row reconstruction on the (110) surfaces of Ag, Pd, Ni and Cu is a general phenomenon for which a common origin was postulated [60]. Some differences are however present among the materials, as the alkali coverage necessary to induce the reconstruction depends on the substrate and as not all the metals show the same $(1 \times n)$ structures.

For Ag(110) and Cu(110) the series of $(1 \times n)$ ordered missing row structures starts with $n=3$ and corresponds to the removal of every third $\langle 1\bar{1}0 \rangle$ row. With increasing alkali deposition, a (1×2) reconstruction appears, implying the removal of every second substrate row. A second (1×3) structure is present at still higher coverage and corresponds to two out of three top layer $\langle 1\bar{1}0 \rangle$ rows missing. For Pd(110) and Ni(110), on the other hand, only the (1×2) reconstruction forms. The alkali coverage, Θ_K , necessary to induce such reconstructions depends on the substrate. For K/Ag(110) the (1×3) structure is reported for a K coverage of $0.01 \text{ ML} < \Theta_K < 0.05 \text{ ML}$, while for $\Theta_K \approx 0.1 \text{ ML}$ the (1×2) is observed [56]. For K/Cu(110), on the other hand, the (1×3) structure appears only at the larger coverage $\Theta_K = 0.13 \text{ ML}$ and $\Theta_K = 0.2 \text{ ML}$ are necessary to induce the (1×3) and the (1×2) reconstructions respectively [35, 59].

The driving force and the mechanism of alkali induced missing row reconstruction have been longly debated. Different models exist, all of which claim to describe all fcc (110) transition metal surfaces [61, 62, 63]. According to Jacobsen and Nørskov [61] the effect is local and the driving force results from an increase in adsorption energy which overcompensates the energy required for the reconstruction. A minimum coverage of about 0.1 ML is required to reconstruct the whole surface. On the contrary, according to Fu and Ho [63], the reconstruction mechanism operates through an electron

donation effect, which produces an increased surface electron concentration. They find that the surface undergoes a missing row reconstruction as soon as a small amount (≈ 0.05 electrons per surface atoms) of excess charge is transferred to the surface.

In a recent STM investigation Schuster et al. [59] observed the nucleation of the reconstruction on the K/Cu(110) system, showing that each single K atom removes locally two or three substrate atoms out of a $\langle 1\bar{1}0 \rangle$ row. The K adatom could not be imaged, but it was supposed to be accommodated in the resulting hole, thus forming a nucleus for the missing row structure. The long range reconstruction proceeds then by the coalescence of such local nuclei, which interact attractively in the $\langle 1\bar{1}0 \rangle$ direction and repulsively along $\langle 001 \rangle$. Nucleation starts at a small K concentration and does not need a critical coverage. At low coverage the Cu surface is observed to be only locally reconstructed, with (1×2) areas concentrated in islands. At a coverage of about 0.2 ML an extended (1×2) reconstruction forms, whereby the K sits in the missing rows at an average distance of 2.5 Cu atoms. Such study concludes therefore that the reconstruction is strictly local and that a similar mechanism should be active also for the other metals. However such local reconstruction model cannot explain the reconstruction on Ag, Pd and Ni, which takes place at too small a K amount, implying a long range effect, where a single K atoms modifies the configuration of the substrate beyond its nearest neighbors.

The present study confirms that the Ag surface reconstructs completely already at a lower K coverage than it is the case for K/Cu. The average distance between the K adatoms is smaller than expected for a random distribution, implying that they leave vast reconstructed Ag areas with no K. The K adatoms form thus islands on Ag(110), in contrast to the K/Cu case where the K adatoms have only a local effect. Increasing the coverage the distance between the K adatoms decreases monotonously. For the (1×2) phases we find that the position of the K atoms is correlated also between neighbouring rows.

A series of $(1 \times n)$ missing row structures have been obtained evaporating K on Ag(110) at room temperature. Sample SPA-LEED spectra recorded along the $\langle 001 \rangle$ crystallographic direction at different K coverage and showing the $(1 \times n)$ structures are reported in Fig.4.1. Already for $\Theta_K = 0.03$ ML we observe a (1×3) reconstruction, while for $\Theta_K > 0.06$ ML the (1×2) reconstruction was formed. The high coverage (1×3) structure is present at $\Theta_K \approx 0.3$ ML. The (1×3) and especially the (1×2) reconstructions present

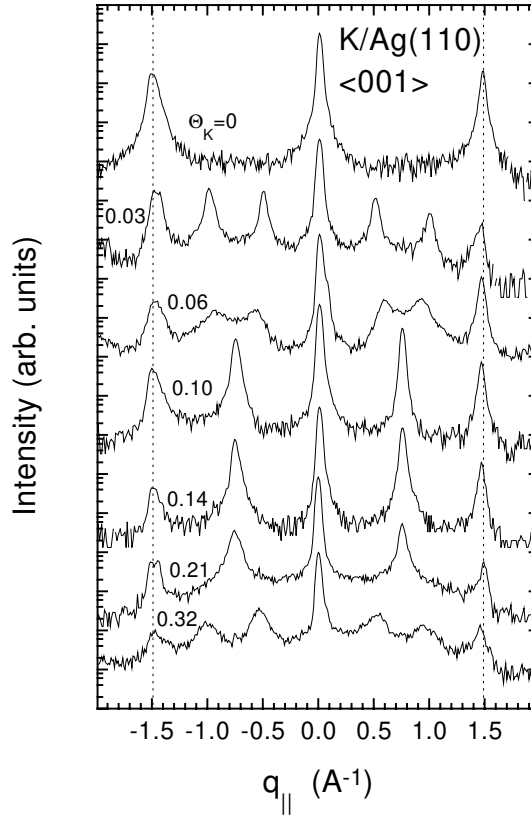


Figure 4.1: SPA-LEED spectra recorded along $\langle 001 \rangle$ for different K coverages measured at $E_i=65.4$ eV after K evaporation at room temperature. The dotted lines indicate the position of the first order spot in the reciprocal surface lattice along this direction.

sharp spots which are indicative of long range order.

The background of the SPA-LEED spectra increases with K adsorption, while the intensity of the main spot decreases without changing its profile. This behaviour indicates an increased statistically distributed disorder at the surface [26].

In Fig.4.2 the SPA-LEED spectra recorded along $\langle 1\bar{1}0 \rangle$ for the same set of measurements of Fig.4.1 are reported, showing that additional features are observed in the diffuse elastic intensity. They shift towards larger exchanged momenta with increasing K coverage. This indicates that the position of K adatoms changes with Θ_K , i.e. that their distance diminishes with increasing

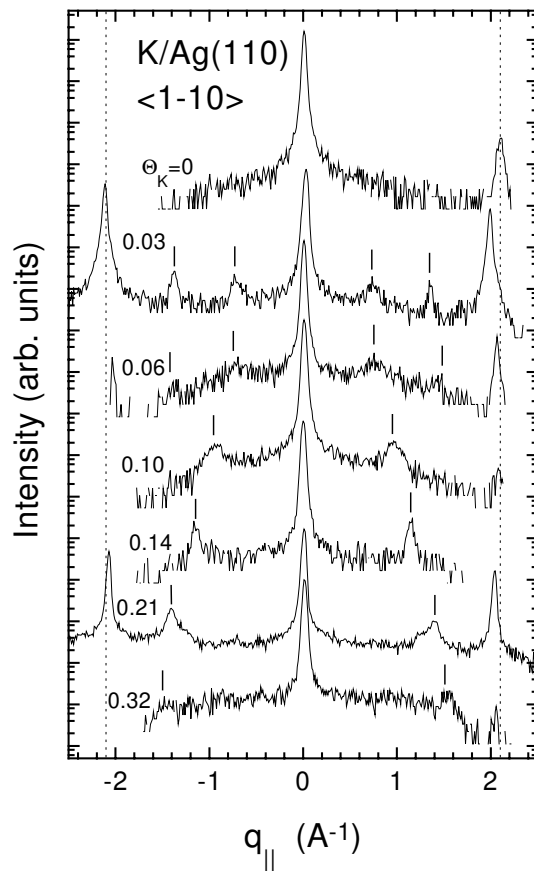


Figure 4.2: SPA-LEED spectra recorded along $\langle 1\bar{1}0 \rangle$ for different K coverages measured at $E_i=65.4$ eV after K evaporation at room temperature. The dotted lines indicate the position of the first order spot in the reciprocal surface lattice along this direction.

K coverage.

The correlation length between the K atoms versus Θ_K , as obtained from the SPA-LEED spectra of Fig.4.2, is reported in Fig.4.3 and decreases from 8.6 \AA at $\Theta_K = 0.03$ ML to 4.5 \AA at $\Theta_K = 0.21$ ML and to 4.2 \AA at $\Theta_K = 0.32$ ML. The latter values are about 5% smaller than the bulk K interatomic spacing, in good agreement with previous results for K/Cu(110) [35]. Two-dimensional LEED patterns recorded for $\Theta_K = 0.03$ ML and $\Theta_K = 0.21$ ML (corresponding to the (1×3) and the (1×2) structures respectively) are reported in Fig.4.4. For the (1×3) surface, streaks are present at approx-

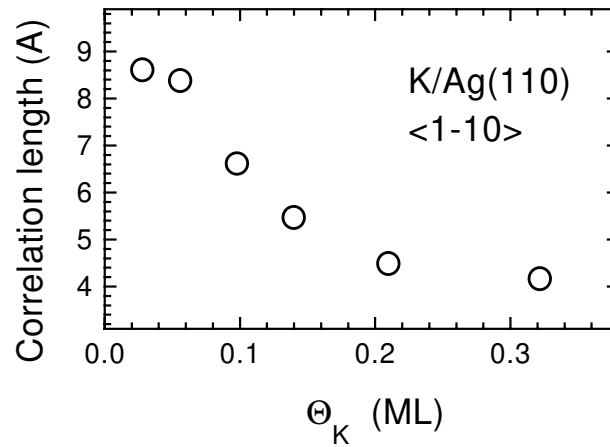


Figure 4.3: Correlation length between the K adatoms versus Θ_K on the reconstructed surface, as deduced from the SPA-LEED data.

imately $1/3$ of the surface Brillouin zone (SBZ) indicating that the K site distribution is uncorrelated between the rows. At $\Theta_K = 0.21$ ML (Fig.4.4b) the streaks break up into spots, showing that the K adatom positions become correlated also between the Ag rows. K-induced peaks are found not only in the (10) SBZ along \bar{Y} (shown in Fig.4.2), but also in the $(0,1/2)$ SBZ at $1/6$ position along the same direction.

In the case of K/Ag(110) therefore, a strong correlation between K atoms is present in both azimuthal directions, at variance with the case of K/Cu [35].

A possible structural model about the position of K adatoms on the Ag(110) surface is presented in Fig.4.5. In part (a) the structure of the K overlayer for the (1×3) phase at $\Theta_K = 0.03$ ML is shown: K sits in the missing rows and forms islands in which every third site is occupied, with no correlation between adatoms in different rows. In part (b) the model of the K overlayer on the (1×2) surface at $\Theta_K = 0.21$ ML is shown: the distance between two K atoms along the missing rows corresponds now to 1.5 times the Ag lattice parameter. K adatoms are also correlated along $\langle 001 \rangle$, as additional LEED spots are present. From the LEED pattern of Fig.4.4 it is however not possible to derive an unique structural model.

It is important to note that the measured K coverage implies that the single K adatom is able to remove Ag atoms also far away from it, so that reconstructed Ag areas without any K atom inside must be present. Such

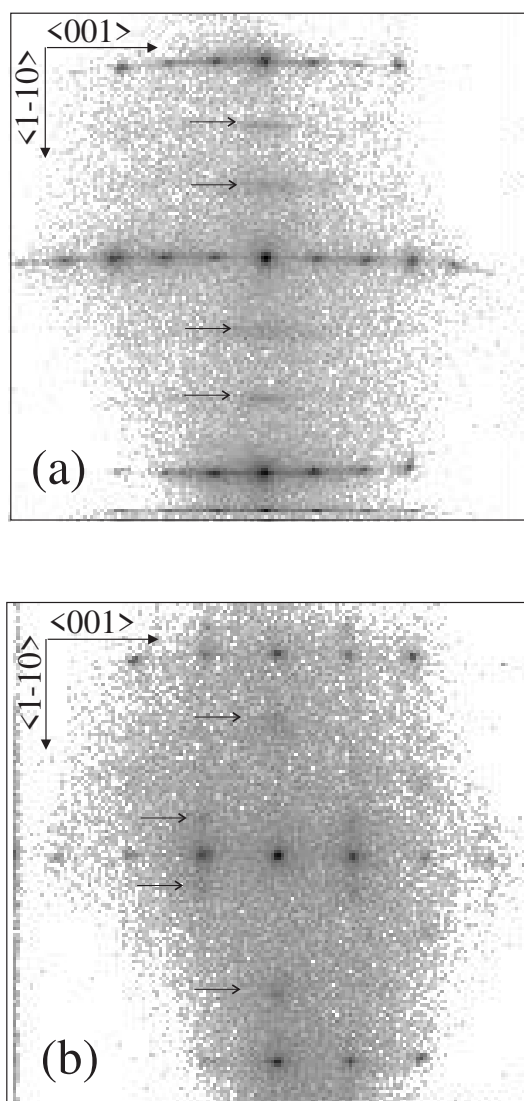


Figure 4.4: Two-dimensional LEED pattern corresponding to a K coverage of a) $\Theta_K = 0.03$ ML and b) $\Theta_K = 0.21$ ML. The arrows show the position of the K-induced additional features.

behaviour is at variance with the apparently very similar case of K/Cu(110) which also presents additional streaks in the reciprocal space for the (1×2) phase. For K/Cu(110) the presence of a K atom every $2.5 a_g$ was postulated over the whole reconstructed (1×2) surface from the analysis of the STM

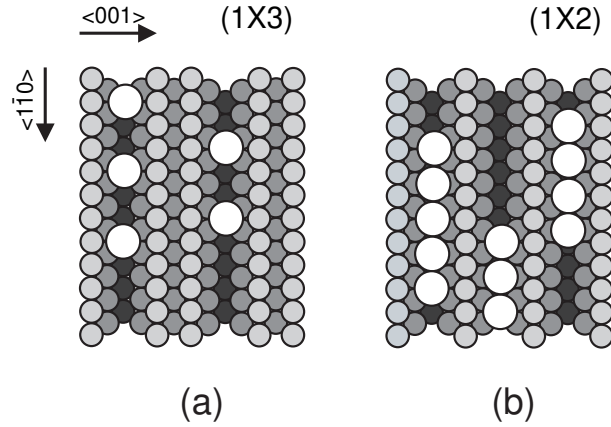


Figure 4.5: Atomistic model of the reconstructed K covered Ag(110) surface for a) $\Theta_K = 0.03$ ML ((1×3) reconstruction) and for b) $\Theta_K = 0.21$ ML ((1×2) reconstruction). The white circles show the position of the K atoms, the gray and black circles the Ag atom positions in the missing row structure.

images [59], a conclusion which cannot be extended to the K/Ag(110) case. The K induced surface reconstruction mechanism is therefore different for the two cases and is most probably connected to the fact that Ag(110) is much more prone to reconstruct than Cu(110).

The process of alkali metal induced missing row reconstruction is thermally activated, with a required minimum substrate temperature of about 150 K. Such an effect has been observed also in the present experiment, as shown in Fig.4.6. SPA-LEED spectra corresponding to the (1×2) reconstruction at $\Theta_K = 0.10$ ML are compared in Fig.4.6 to the spectra obtained at nearly the same K coverage ($\Theta_K = 0.11$ ML) after deposition at $T=100$ K. As one can see in Fig.4.6b, K deposition at low temperature inhibits surface reconstruction. In fact, while in the room temperature case the (1×2) superstructures are clearly visible, only weak features are present in the low temperature deposition case, indicating that only a local rearrangement of the substrate takes place around the K adatoms. Along $\langle 1\bar{1}0 \rangle$ the additional features due to K adsorption are still present, even if their intensity is strongly reduced, indicating a more disordered surface and a worse correlation between the K adatoms.

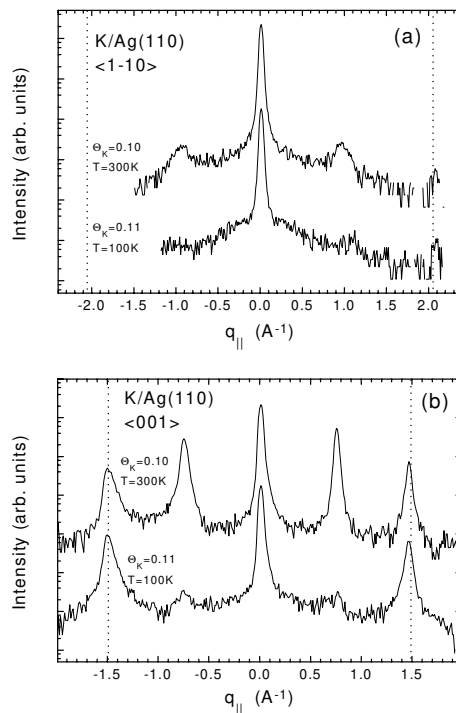


Figure 4.6: SPA-LEED spectra for the reconstructed (1×2) surface at $\Theta_K = 0.10$ ML and for the unreconstructed surface at $\Theta_K = 0.11$ ML along a) $\langle 1\bar{1}0 \rangle$ and b) $\langle 001 \rangle$.

4.3 Surface electronic excitations

4.3.1 Influence of a trace amount of K on surface plasmon dispersion

After the ELS-LEED reinvestigation of the surface plasmon dispersion on Ag(111) and Ag(110), reported in the previous chapter, two main observations remained however unexplained:

i) phases of the same material behave in *qualitatively* different ways as the dispersion on Ag(001) is nearly linear [16], while for the other surfaces a large and *isotropic* quadratic term is present [17, 38, 41, 42]. Such term is usually attributed to bulk properties, which are isotropic for a face centered cubic crystal as Ag. The most striking difference between the (001) and the other two low Miller index faces is that for the former an interband transi-

tion is present between Shockley states [64] which nearly matches the surface plasmon energy, thus opening a very efficient decay channel. Were this the relevant mechanism, a reduction of the quadratic term would be expected for the other surfaces, too, if appropriate surface states could be created.

ii) The linear dispersion coefficient on Ag(110) is anisotropic with respect to crystal azimuth, being three times larger along $\langle 001 \rangle$ than along $\langle 1\bar{1}0 \rangle$ [41, 42]. As already discussed, the phenomenon cannot be described by the quantitative model developed by Liebsch [7], while according to the theory by P.J. Feibelman, which relates the anisotropic dispersion to the stronger geometric corrugation of the electronic density along $\langle 001 \rangle$ [18] (see also section 1.2.2), if one could change the amplitude of the geometric corrugation one should be able to modify the linear term of the dispersion.

Such experiments are feasible for the K/Ag(110) system at low coverage as the surface morphology is severely affected by the missing row reconstructions [34] and as an empty K induced surface state forms at 3.4 eV above the Fermi level [65], while an intrinsic filled surface state is present at \bar{Y} [66], thus creating a similar situation as for the bare Ag(001) surface.

An ELS-LEED investigation of the energy loss spectra on the reconstructed Ag phases induced by K adsorption is reported in this section. Sample spectra recorded at the same q_{\parallel} but along the two high symmetry crystallographic directions of Ag(110) are reported in Fig.4.7 for different values of Θ_K . K adsorption does not affect the energy loss for q_{\parallel} along $\langle 1\bar{1}0 \rangle$ (Fig.4.7a), while it displaces it to lower energy along $\langle 001 \rangle$ (Fig.4.7b). The shift is only present at large wavevectors and its magnitude does not depend on surface reconstruction, being present also for the unreconstructed case (uppermost spectrum in Fig.4.7). Adding more K increases the damping, but has little effect on frequency and dispersion of the surface plasmon.

The measured values of $\hbar\omega_s$ are reported in Fig.4.8 vs. q_{\parallel} for the low coverage (1×3) and for the (1×2) reconstructed surfaces, along both high symmetry directions. Continuous and dashed lines give the result for the anisotropic surface plasmon dispersion of clean Ag(110), reported in section 3.3. As expected, K has little effect at vanishing momentum transfer in agreement with classical dielectric theory which predicts that the surface plasmon frequency is dictated by the bulk dielectric function $\epsilon(\omega) = -1$. At large q_{\parallel} along $\langle 001 \rangle$, on the other hand, the surface plasmon energy is downshifted in presence of K. In order to be more quantitative, the experimental data

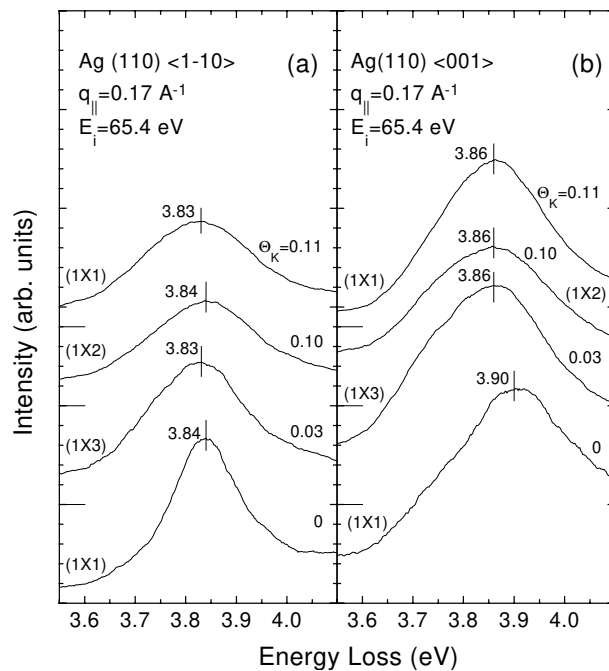


Figure 4.7: Energy loss spectra for different coverage of K on Ag(110), after a smoothing of the experimental data, are reported for the (1×3) and the (1×2) reconstructions and for the unreconstructed surface along both high symmetry directions at the same momentum transfer.

were fitted with the same parabolic form as in section 3.3:

$$\hbar\omega_s(q_{\parallel}) = \hbar\omega_s(0) + Aq_{\parallel} + Bq_{\parallel}^2 \quad (4.1)$$

The values of A and B are reported vs. Θ_K in Fig.4.9 for the low K coverage regime, while the complete set of values is collected in Table 4.1 and 4.2 .

The main cause for the shift of the energy loss peak upon K adsorption is the reduction of the quadratic term along $\langle 001 \rangle$, which drops from the clean surface value of $3.4 \pm 0.3 \text{ eV}\text{\AA}^2$ to $2.1 \pm 0.2 \text{ eV}\text{\AA}^2$ at $\Theta_K = 0.03 \text{ ML}$, while it remains nearly constant along $\langle 1\bar{1}0 \rangle$. The linear term is thereby only slightly affected, independently on surface reconstruction. At larger K coverage an almost linear change of both linear and quadratic dispersion terms along both directions takes place. The anisotropy of both coefficients is completely removed at $\Theta_K = 0.3 \text{ ML}$. The larger error bars on the coefficients at $\Theta_K = 0.10 \text{ ML}$ and $\Theta_K = 0.14 \text{ ML}$ along $\langle 1\bar{1}0 \rangle$ are due to the reduced set of measurements.

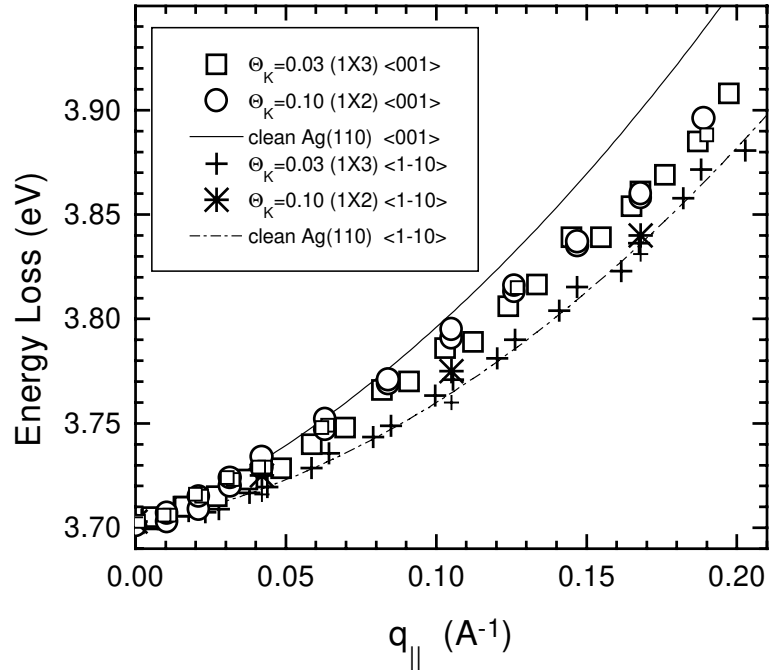


Figure 4.8: Surface plasmon dispersion with $q_{||}$ for different Θ_K . The continuous and dashed lines show the dispersion on the clean Ag(110) surface.

The meaning of quadratic and linear terms in surface plasmon dispersion has long been debated. Within jellium theory, the first is ascribed to bulk properties and the latter to surface properties [1]. The present experiment demonstrates that there is no link between the dispersion coefficients and surface corrugation, as our data are identical for the reconstructed and unreconstructed cases. The anisotropy of the linear term for the bare Ag(110) surface, as well as the difference of the quadratic term between Ag(001) and the other faces, must accordingly be of electronic origin.

K adsorption on Ag(110) involves a decrease in the work function and the formation of new interband transitions involving either s and p K induced states or one of the K induced states and a Shockley state. The relevance of a change of the work function for the observed phenomenon is excluded by the observation that the drop in the quadratic term takes place already at very low K coverage when such change is negligible. The observed effect cannot be due to the interband transition between the K induced states as we

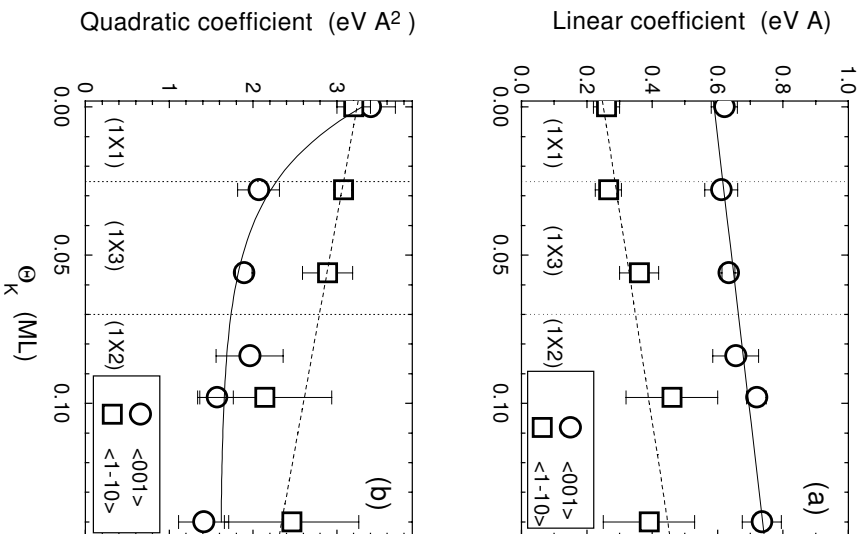


Figure 4.9: a) Linear and b) quadratic coefficients of surface plasmon dispersion versus Θ_K , along $\langle 001 \rangle$ (filled symbols) and $\langle -1\bar{1}0 \rangle$ (open symbols). The continuous and dashed lines are a guide to the eye.

observe the related loss in the energy loss spectra only for $\Theta_K > 0.6$ ML, as we'll see in section 4.4. Both states must therefore be empty at low coverage as it is the case also for K/Ag(001) [67]. Interband transitions involving the Ag(110) surface state at \bar{Y} [64] and the K induced p state are on the other hand possible. The energy gap between such states is similar to the one present at \bar{X} on Ag(001) and nearly matches the surface plasmon energy. The downward shift of the K induced p band with coverage [65] should inhibit the effect at larger Θ_K , but the shift might be compensated by the onset of dispersion, which raises the energy of the p band at \bar{Y} . The energy gap at \bar{Y} remains therefore unaffected. The new decay channel is expected to

reduce the surface plasmon frequency in analogy to the downward shift of the Ag plasmon frequency from its free electron value induced by the presence of the interband transitions involving the d bands. Transitions from the Shockley state to the K s state are on the other hand not expected to affect surface plasmon dispersion significantly because of the mismatch between their energy and the one of the surface plasmon. No direct decay channel is therefore possible.

The anisotropy of the observed phenomenon can be related with the strong anisotropy of the investigated system. Indeed a strong interaction between the Ag atoms builds up along $\langle 001 \rangle$ and leads to $(1 \times n)$ reconstructions. Moreover the interaction between the K adatoms is repulsive along $\langle 001 \rangle$, while it becomes attractive beyond a certain distance along $\langle 1\bar{1}0 \rangle$ [59], as confirmed by the analysis of the SPA-LEED spectra.

The value of the quadratic term for the bare Ag(111) and Ag(110) surfaces is most probably dictated by bulk properties as no surface interband transitions are present for those faces near ω_s .

In conclusion, by studying the effect of K adsorption on Ag(110), it has been possible to demonstrate that:

- i) the quadratic term of surface plasmon dispersion for Ag(001) and for K/Ag(110) $\langle 001 \rangle$ is determined by the balance between bulk properties and the presence of a surface decay channel for the surface plasmon, associated to surface interband transitions;
- ii) the linear term is not affected by surface corrugation on the atomic scale and by K adsorption, so that its anisotropy for the bare Ag(110) surface must be of electronic origin;
- iii) the properties of K/Ag(110) are strongly dictated by the K adatoms already at the extremely small concentration of 0.03 ML, thus demonstrating the long range influence of alkali atoms induced changes on the physical properties of the substrate. This result holds for all alkali atom adsorption systems, as demonstrated by the recently reported anomalous contraction of the Cs induced reconstructed Cu(110) surface [68].

4.3.2 Surface plasmon dispersion at higher K coverage on the reconstructed surfaces

We consider now the case of a higher K coverage on the reconstructed surfaces, where the anisotropy of surface plasmon dispersion is completely re-

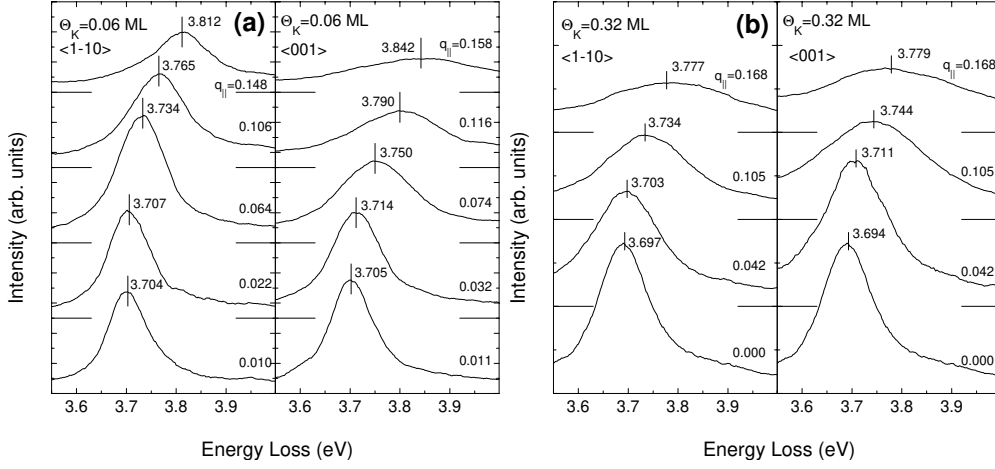


Figure 4.10: Energy loss spectra for the Ag(110) (1×2) and (1×3) II reconstructed surface, corresponding to a) $\Theta_K = 0.06$ ML and b) $\Theta_K = 0.32$ ML, recorded at $E_i = 65.4$ eV along $\langle 1\bar{1}0 \rangle$ and $\langle 001 \rangle$, after a smoothing of the experimental data.

moved. Some spectra, recorded for the reconstructed surfaces corresponding to $\Theta_K = 0.06$ ML and $\Theta_K = 0.32$ ML are reported in Fig.4.10, along the two high symmetry crystallographic directions $\langle 001 \rangle$ and $\langle 1\bar{1}0 \rangle$. The dispersion at $\Theta_K = 0.06$ ML (Fig. 4.10(a)) is still anisotropic.

Surface plasmon energy is reported in Fig.4.11 vs. $q_{||}$. The data corresponds to the low coverage (1×3) , to the (1×2) and to the high coverage (1×3) reconstructed surfaces at different Θ_K , along the two high symmetry directions and are partially the same as reported in Fig.4.8. Continuous lines show the surface plasmon dispersion on the clean Ag(110) surface. As one can see in Fig.4.11a and as already discussed in section 4.3.1, the Ag surface plasmon dispersion at low Θ_K is little affected by K adsorption, while it is strongly modified at $\Theta_K = 0.32$ ML, i.e. as soon as the (1×3) phase forms. Thus, while the anisotropy of the Ag(110) surface plasmon dispersion is already reduced with respect to the bare surface case, for the (1×3) and (1×2) reconstructions it disappears for the high coverage (1×3) structure.

The results of a parabolic fit of the data are collected in Table 4.1 and 4.2 for all data corresponding to room temperature deposition of the K film for measurements along $\langle 001 \rangle$ and $\langle 1\bar{1}0 \rangle$ respectively. The larger errors on the coefficients determined at $\Theta_K = 0.10$ ML and 0.14 ML are due to the smaller set of data.

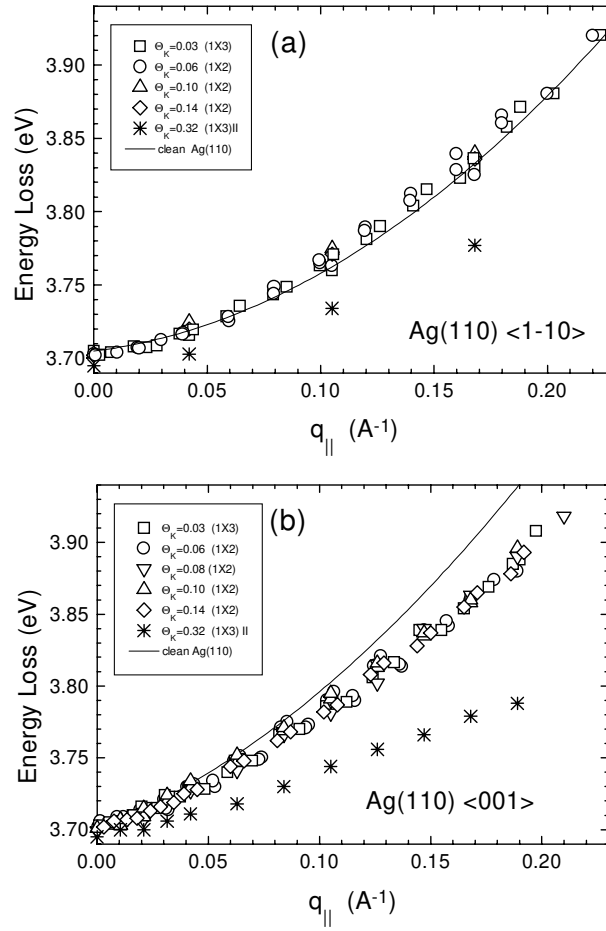


Figure 4.11: Surface plasmon dispersion with $q_{||}$ for different K coverages, on the reconstructed surfaces along a) $\langle 110 \rangle$ and b) $\langle 001 \rangle$, recorded at $E_i = 65.4$ eV. The continuous lines show the dispersion on the Ag(110) clean surface in the two azimuthal directions.

A comparison with the coefficients determined for the clean Ag(110) surface is also given. Let us analyze in detail the effect of K coverage on the different terms:

i) The surface plasmon energy at vanishing $q_{||}$ is weakly reduced by K adsorption on the reconstructed surface, showing that the presence of a little amount of ordered K does not significantly influence the dielectric response at the surface. This result is at variance with the case of low temperature deposition, where a strong increase of the surface plasmon energy is present,

Table 4.1: Surface plasmon dispersion coefficients derived by χ^2 -analysis for K deposition at room temperature along $\langle 001 \rangle$.

Θ_K (ML)	reconstruction	$\hbar\omega_s(0)$ (eV)	A (eV Å)	B (eV Å ²)
0	(1 × 1)	3.700 ± 0.002	0.62 ± 0.04	3.4 ± 0.3
0.03	(1 × 3)	3.700 ± 0.002	0.61 ± 0.05	2.1 ± 0.2
0.06	(1 × 2)	3.699 ± 0.002	0.63 ± 0.02	1.9 ± 0.1
0.08	(1 × 2)	3.698 ± 0.003	0.66 ± 0.08	2.0 ± 0.3
0.10	(1 × 2)	3.698 ± 0.002	0.72 ± 0.03	1.6 ± 0.2
0.14	(1 × 2)	3.698 ± 0.002	0.74 ± 0.06	1.4 ± 0.3
0.32	(1 × 3)	3.693 ± 0.003	0.31 ± 0.07	0.95 ± 0.4

Table 4.2: Surface plasmon dispersion coefficients derived by χ^2 -analysis for K deposition at room temperature along $\langle 1\bar{1}0 \rangle$.

Θ_K (ML)	reconstruction	$\hbar\omega_s(0)$ (eV)	A (eV Å)	B (eV Å ²)
0	(1 × 1)	3.702 ± 0.003	0.26 ± 0.05	3.2 ± 0.2
0.03	(1 × 2)	3.702 ± 0.002	0.27 ± 0.02	3.1 ± 0.1
0.06	(1 × 2)	3.700 ± 0.002	0.36 ± 0.06	2.9 ± 0.3
0.10	(1 × 2)	3.703 ± 0.005	0.46 ± 0.1	2.1 ± 0.8
0.14	(1 × 2)	3.701 ± 0.005	0.39 ± 0.1	2.4 ± 0.8
0.32	(1 × 3)	3.692 ± 0.005	0.21 ± 0.12	1.8 ± 0.7

possibly connected to the formation of a K-Ag interface mode, as we'll discuss at length in section 4.3.4.

ii) The linear term of the surface plasmon dispersion increases slightly at low Θ_K for q_{\parallel} along $\langle 001 \rangle$ and decreases eventually for $\Theta_K > 0.14$ ML. For $\Theta_K > 0.32$ ML it becomes identical to the value observed along $\langle 1\bar{1}0 \rangle$.

iii) The quadratic term along $\langle 001 \rangle$ is reduced by nearly a factor 2 with respect to the clean surface value already at $\Theta_K = 0.03$ ML and decreases then more slowly to 1 eV Å². Along $\langle 1\bar{1}0 \rangle$ it decreases on the contrary almost linearly with increasing K coverage. At $\Theta_K = 0.32$ ML also this term becomes isotropic within experimental error.

4.3.3 Surface plasmon damping on the reconstructed surfaces

The full width at half maximum (FWHM) of the surface plasmon vs. q_{\parallel} is reported in Fig.4.12. The data, deconvoluted with respect to energy and angular resolution as described in section 3.5, first of all indicate that the presence of K has little effect on surface plasmon damping for $q_{\parallel} = 0$.

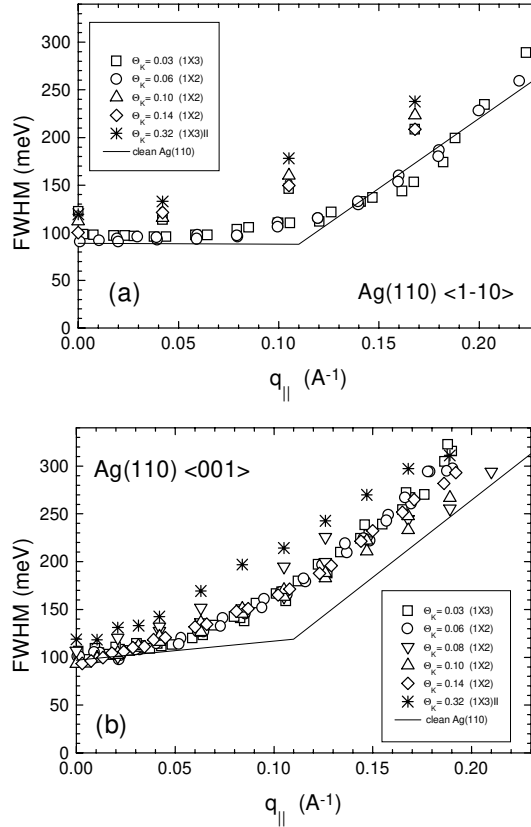


Figure 4.12: Dispersion with q_{\parallel} of the FWHM of the surface plasmon for the same sets of data reported in Fig. 8, along a) $\langle 1\bar{1}0 \rangle$ and b) $\langle 001 \rangle$.

Along $\langle 1\bar{1}0 \rangle$ the FWHM increases initially weakly with q_{\parallel} , while it grows eventually more rapidly above the critical q_{\parallel} value ($q_{\parallel,c} \approx 0.11 \text{ \AA}^{-1}$), as was the case for the clean surface. With increasing Θ_K the damping rate increases both below and above $q_{\parallel,c}$. Notably the value of $q_{\parallel,c}$ does not change

Table 4.3: Surface plasmon damping coefficients versus q_{\parallel} derived by χ^2 analysis for K deposition at T=100 K, along $\langle 1\bar{1}0 \rangle$: $\Delta\hbar\omega_s(0)$ and B, which describes the linear dependence of the FWHM on q_{\parallel} .

Θ_K (ML)	reconstruction		$\Delta\hbar\omega_s(0)$ (eV)	B (eV \AA)
0.03	(1 \times 3)	$q_{\parallel} < 0.11 \text{ \AA}^{-1}$	0.09 ± 0.01	0.13 ± 0.05
0.03	(1 \times 3)	$q_{\parallel} > 0.11 \text{ \AA}^{-1}$		1.60 ± 0.1
0.06	(1 \times 2)	$q_{\parallel} < 0.11 \text{ \AA}^{-1}$	0.09 ± 0.01	0.20 ± 0.05
0.06	(1 \times 2)	$q_{\parallel} > 0.11 \text{ \AA}^{-1}$		1.60 ± 0.1
0.10	(1 \times 2)	$q_{\parallel} < 0.11 \text{ \AA}^{-1}$	0.10 ± 0.01	0.48 ± 0.05
0.14	(1 \times 2)	$q_{\parallel} < 0.11 \text{ \AA}^{-1}$	0.10 ± 0.01	0.47 ± 0.05
0.32	(1 \times 3)	$q_{\parallel} < 0.11 \text{ \AA}^{-1}$	0.12 ± 0.01	0.57 ± 0.05

with K adsorption. A linear fit to the data, for $q_{\parallel} < q_{\parallel c}$ and for $q_{\parallel} > q_{\parallel c}$, is reported in Table 4.3. For $\Theta_K = 0.10$ ML, $\Theta_K = 0.14$ ML and $\Theta_K = 0.32$ ML only the data above $q_{\parallel c}$ are reported, as the set of data was too small to allow for such a fine analysis.

Along $\langle 001 \rangle$ the damping is generally stronger than for the clean surface case. For $\Theta_K = 0.03$ ML and $\Theta_K = 0.06$ ML two damping mechanisms can still be identified. The critical q_{\parallel} value appears however to be shifted to lower q_{\parallel} ($q_{\parallel c} \approx 0.06 \text{ \AA}^{-1}$ versus $q_{\parallel c} = 0.11 \text{ \AA}^{-1}$ for the clean Ag(110) surface). Alternatively a quadratic fit might be more appropriate to describe the q_{\parallel} dependence. At still larger Θ_K , the damping is increased already at small q_{\parallel} . The result of a fit of the FWHM versus q_{\parallel} with linear forms, above and below $q_{\parallel c}$, are collected in Table 4.4. As one can see the damping rate increases slightly with increasing coverage.

4.3.4 Surface plasmon at higher K coverage on the unreconstructed surface

The surface plasmon energy at vanishing q_{\parallel} is reported versus Θ_K in Fig.4.13 for both high and low temperature deposition. As one can see $\hbar\omega_s(0)$ is weakly reduced at small K coverage on the reconstructed surface, showing that the presence of a little amount of ordered K does not significantly influence the dielectric response at the surface. The effect become however

Table 4.4: Surface plasmon damping coefficients versus q_{\parallel} derived by χ^2 analysis for K deposition at $T=100$ K, along $\langle 001 \rangle$: $\Delta\hbar\omega_s(0)$ and B, which describes the linear dependence of the FWHM on q_{\parallel} .

Θ_K (ML)	reconstruction		$\Delta\hbar\omega_s(0)$ (eV)	B (eV \AA)
0.03	(1 \times 3)	$q_{\parallel} < 0.05 \text{ \AA}^{-1}$	0.10 ± 0.01	0.41 ± 0.05
0.03	(1 \times 3)	$q_{\parallel} > 0.05 \text{ \AA}^{-1}$		1.53 ± 0.1
0.06	(1 \times 2)	$q_{\parallel} < 0.05 \text{ \AA}^{-1}$	0.10 ± 0.01	0.36 ± 0.05
0.06	(1 \times 2)	$q_{\parallel} > 0.05 \text{ \AA}^{-1}$		1.48 ± 0.1
0.08	(1 \times 2)	$q_{\parallel} < 0.05 \text{ \AA}^{-1}$	0.10 ± 0.01	0.67 ± 0.05
0.08	(1 \times 2)	$q_{\parallel} > 0.05 \text{ \AA}^{-1}$		1.01 ± 0.1
0.10	(1 \times 2)	$q_{\parallel} < 0.05 \text{ \AA}^{-1}$	0.09 ± 0.01	0.62 ± 0.05
0.10	(1 \times 2)	$q_{\parallel} > 0.05 \text{ \AA}^{-1}$		1.07 ± 0.1
0.14	(1 \times 2)	$q_{\parallel} < 0.05 \text{ \AA}^{-1}$	0.09 ± 0.01	0.66 ± 0.05
0.14	(1 \times 2)	$q_{\parallel} > 0.05 \text{ \AA}^{-1}$		1.30 ± 0.1
0.32	(1 \times 3)	$q_{\parallel} < 0.05 \text{ \AA}^{-1}$	0.12 ± 0.01	0.59 ± 0.05
0.32	(1 \times 3)	$q_{\parallel} > 0.05 \text{ \AA}^{-1}$		1.16 ± 0.1

relatively large for the (1 \times 3) case at $\Theta_K = 0.32$ ML. The negative shift observed for the reconstructed surfaces is at variance with the case of low temperature deposition, where a strong increase of the surface plasmon energy is observed (circles in Fig.4.13).

In Fig.4.14 the energy of the Ag surface plasmon loss (upper panel) and its damping (lower panel) at vanishing momentum transfer are reported for a wider Θ_K range than in Fig.4.13, for deposition at $T = 100$ K. $\hbar\omega_s$ increases monotonously with increasing Θ_K . The shift is linear for $\Theta_K < 0.52$ ML, where it jumps abruptly from 3.74 eV to 3.78 eV. This shift is correlated with an increased damping of the losses, whose FWHM grows (after deconvolution) initially linearly from the bare surface value of 95 meV to 155 meV at $\Theta_K = 0.52$ ML and jumps then to 200 meV, before decreasing eventually again above 1.02 ML.

The shift of the Ag surface plasmon frequency at $q_{\parallel} = 0$ is not expected by dielectric theory which states, as seen in section 1.1, that this quantity should be determined by the condition that the bulk dielectric function $\epsilon(\omega) = -1$, independently of the state of the Ag surface. A negative shift was however

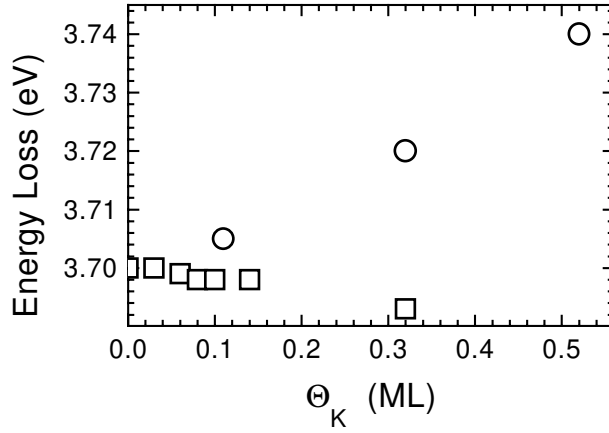


Figure 4.13: $\hbar\omega_s(0)$ versus Θ_K for the reconstructed surfaces corresponding to room temperature deposition (\square) and to low temperature disordered K adsorption (\circ).

reported also for Cl/Ag(111) [69]. In that case the effect was ascribed to the poor angular resolution of the experiment, i.e. to the integration in momentum space of a dispersion which changes from positive to negative. Such explanation does not hold for the present case as the dispersion of the loss changes with K coverage but remains positive and as the q_{\parallel} integration is negligible for our data because of ELS-LEED acquisition. The effect must therefore have physical origin.

As one can see in Fig.4.14, we can distinguish two different K-coverage ranges. At low coverage ($\Theta_K < 0.52$ ML) the peak shifts linearly with Θ_K remaining sharp. If the effect would be associated to the interplay of the intensity of surface plasmon at 3.70 eV and multipole mode at 3.74 eV [43] we would expect, contrary to experimental evidence, that the shift should depend on impact energy as we have seen that the multipole loss is not dipole active. If it would be associated to the excitation of the bulk plasmon, on the other hand, we would not expect a linear shift as the intensity of the latter mode is much weaker than the one of the surface excitation [2] and we would expect it to become significant only above a finite coverage, again contrary to experimental evidence. The phenomenon might be therefore indicative of departure from ideal dielectric theory and be connected to the shift from the value appropriate to the surface plasmon (determined by $\epsilon(\omega) = -1$) to the one appropriate to the interface mode (given by $\epsilon(\omega) = -\epsilon_{film}$).

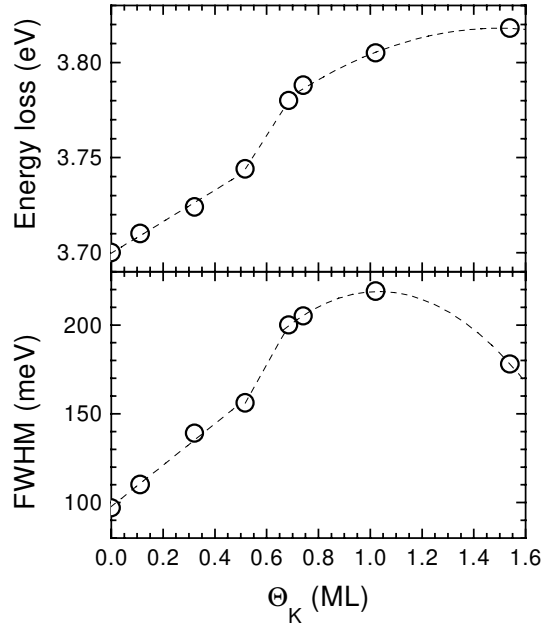


Figure 4.14: Upper panel: Ag surface plasmon energy versus Θ_K for $T_{dep} = 100$ K; lower panel: the corresponding Ag surface plasmon damping versus Θ_K . The dashed lines are a guide for the eye.

The jump at $\Theta_K = 0.69$ ML cannot be explained within this frame and it could be due to the onset of a K related mode. Indeed for K/Al Liebsch [70] finds for the bilayer case that the loss spectra should be dominated at $q_{\parallel} = 0$ by the multipole mode of the overlayer at 3.5 eV. Such mode might have an energy of 3.82 eV in the case of K/Ag because of the different density of the K film and be present already at an average coverage of 1 ML, because of the strong inhomogeneity of the overlayer.

A comparison between the surface plasmon dispersion on the unreconstructed (1×1) and on the reconstructed (1×2) surfaces is reported in Fig.4.15, while the dispersion coefficients are shown in Table 4.5.

As one can see the reconstruction has only a minor effect on the dispersion coefficients, the differences being within experimental error. The geometrical structure does not affect in fact the surface plasmon dispersion significantly as the most corrugated case is the least anisotropic. In Table 4.5 we also report the values obtained for $\Theta_K = 0.52$ ML. The quadratic term of the dispersion has then the same value as reported for the bare surface case,

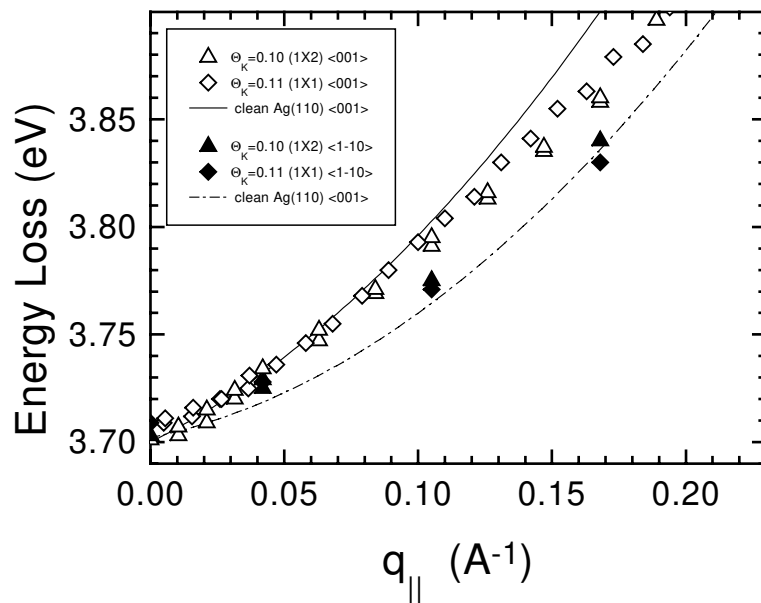


Figure 4.15: Surface plasmon dispersion with $q_{||}$ for the reconstructed (1×2) and the unreconstructed surface, at $\Theta_K = 0.10$ ML and $\Theta_K = 0.11$ ML respectively, along $\langle 001 \rangle$ and $\langle 1\bar{1}0 \rangle$. The continuous and dashed lines show the dispersion on the Ag(110) bare surface in the two azimuthal directions.

Table 4.5: Surface plasmon dispersion coefficients derived by χ^2 -analysis for K deposition at T=100 K.

Θ_K (ML)	Azimuth	$\hbar\omega_s(0)$ (eV)	A (eV Å)	B (eV Å ²)
0.11	$\langle 001 \rangle$	3.701 ± 0.002	0.74 ± 0.06	1.6 ± 0.3
0.52	$\langle 001 \rangle$	3.733 ± 0.004	0.24 ± 0.1	3.6 ± 0.8
0.11	$\langle 1\bar{1}0 \rangle$	3.709 ± 0.005	0.37 ± 0.1	2.08 ± 0.8

while the linear term is 3 times smaller and coincides, within experimental error, with the value observed on the reconstructed surface at $\Theta_K = 0.32$ ML.

The $q_{||}$ dependence of the Ag surface plasmon frequency and damping for $\Theta_K = 0.52$ ML, along $\langle 001 \rangle$ after deposition at 100K, is compared in Fig.4.16 with the case of $\Theta_K = 0.11$ ML and with the bare Ag (110) surface.

At small Θ_K (\diamond) the Ag surface plasmon loss shows a slight increase of the damping around 0.10 \AA^{-1} , a slight increase of the energy at $q_{\parallel} = 0$, and a slight decrease at large q_{\parallel} . The dispersion along $\langle 1\bar{1}0 \rangle$ is on the contrary little affected except for the increase of the frequency at $q_{\parallel} = 0$. At large Θ_K (\square) the loss is more heavily damped and strongly shifted in energy also near $q_{\parallel} = 0$, joining the dispersion curve of the clean surface only above 0.07 \AA^{-1} .

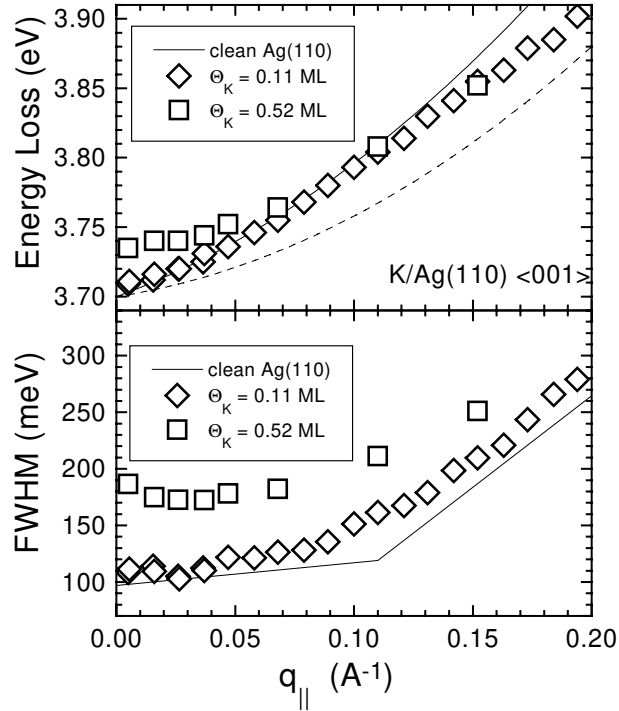


Figure 4.16: Upper Panel: Ag surface plasmon dispersion with q_{\parallel} for two different K coverages along the $\langle 001 \rangle$ azimuthal direction. Lower panel: Ag surface plasmon damping for the same data. The continuous lines show dispersion and damping for the clean Ag(110) surface along the same azimuthal direction, the dashed line the dispersion of the bare surface along $\langle 1\bar{1}0 \rangle$.

Fitting the dispersion curve with a quadratic form it can be seen that the weight of the (initially anisotropic) linear dispersion term is decreased with respect to the bare surface case (continuous line) shifting from 0.62 eV\AA along $\langle 001 \rangle$ to the isotropic value of 0.24 eV\AA at $\Theta_K = 0.52 \text{ ML}$. Such

value is thus very near to the linear term of the bare surface along $\langle 1\bar{1}0 \rangle$, which reads 0.25 eV\AA . The quadratic term decreases initially with respect to the bare surface value, passing from 3.4 eV\AA^2 to 1.6 eV\AA^2 at $\Theta_K = 0.11 \text{ ML}$ and increases eventually again recovering the initial value at large Θ_K (it reads 3.6 eV\AA^2 at $\Theta_K = 0.52 \text{ ML}$). The same effect is present also for the ordered $(1 \times n)$ reconstructions as seen in section 4.3.1, and is due to the formation of K induced interband transitions.

The decrease of the linear dispersion coefficient with Θ_K might be due either to the modification of the charge density profile at the surface, connected to surface charging, which would influence the position of the centroid of the induced charge; or to a q_{\parallel} dependent shift of the surface plasmon frequency connected to the modified screening of the d-electrons. For Cl/Ag, where positive charging of the substrate is present, the slope changes from positive to negative [69]. For K/Ag we have charging with opposite sign and, following the discussion of ref.[69], the spill out density profile is expected to become smoother thus moving the centroid of induced charge further outside of the geometric surface. On the other hand the polarizable ion-cores of the Ag atoms should be better screened so that the frequency at large q_{\parallel} should decrease. The two effects have therefore opposite sign for K/Ag and the latter seems to dominate.

4.4 Collective excitations on K layers

Elementary electronic excitations of alkali-metal atom overlayers adsorbed on metal surfaces have been a subject of inquiry for many years (see [71] and references therein). Of special interest is the case of very thin films (less than 2 monolayers) for which the spatial confinement of the conduction electrons is important. Angle resolved experiments were performed for K and Na on Al(111) by K. D. Tsuei et al. [72] and more recently for K/Ni(111) by G. Chiarello et al. [73], with contradictory conclusions: a significant dependence of the initial dispersion of the K induced loss on coverage was reported for the films deposited on Al(111), while in the case of Ni(111) the form of the dispersion coincides with the one of a thick K film already for the bilayer case. No explanation was found so far for this non-universal behaviour. Moreover in both cases the energy loss shifts with coverage, a phenomenon which was associated [70] to the coverage dependent interplay of the electronic interband transition at low coverage and of the excitation of monopole and multipole

surface plasmon at higher coverage. In the present section the case of a disordered K film deposited on Ag(110) at $T=100$ K will be addressed. The present results are at variance with those of K/Al and K/Ni, indicating that the problem is more complicated than assumed so far.

Sample spectra recorded at $E_i = 51.4$ eV as a function of K coverage at vanishing q_{\parallel} are reported in Fig.4.17. Similar data were obtained for $E_i = 65.3$ eV thus demonstrating that the losses are dipolarly excited. For a K coverage lower than $\Theta_K = 0.52$ ML only the Ag surface plasmon is present. Its frequency shifts upwards with increasing coverage while the loss broadens, as we have seen in section 4.3.4.

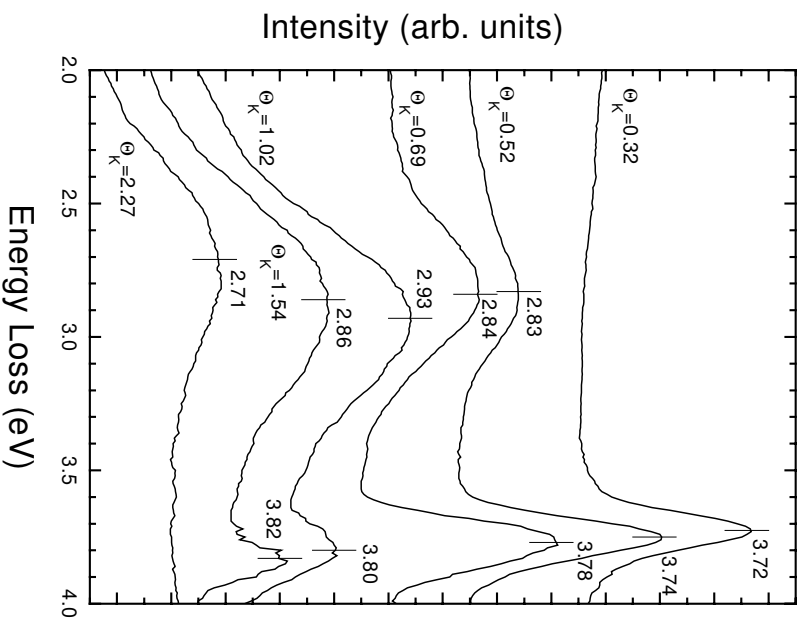


Figure 4.17: Energy loss spectra for K/Ag(110) at $q_{\parallel} = 0$, recorded with ELS-LEED at $E_i = 51.4$ eV for different K coverage, after a smoothing of the experimental data. The momentum transfer depends little on the energy loss value because of the relatively high impact energy and of the near normal geometry.

Above $\Theta_K = 0.52$ ML a K related loss shows up, which is much broader than the Ag surface plasmon, whose energy increases with Θ_K up to 1.02 ML and then decreases again. No energy losses could be observed above $\Theta_K = 2.3$ ML because of vanishing surface reflectivity. The corresponding SPA-LEED profiles, recorded with ELS-LEED along the high symmetry $\langle 001 \rangle$ and $\langle 1\bar{1}0 \rangle$ directions, are reported in Fig.4.18. No superstructures are present, which is indicative of statistically distributed K adatoms without an ordered formation of islands as no splitting of the peaks is observed. K adsorp-

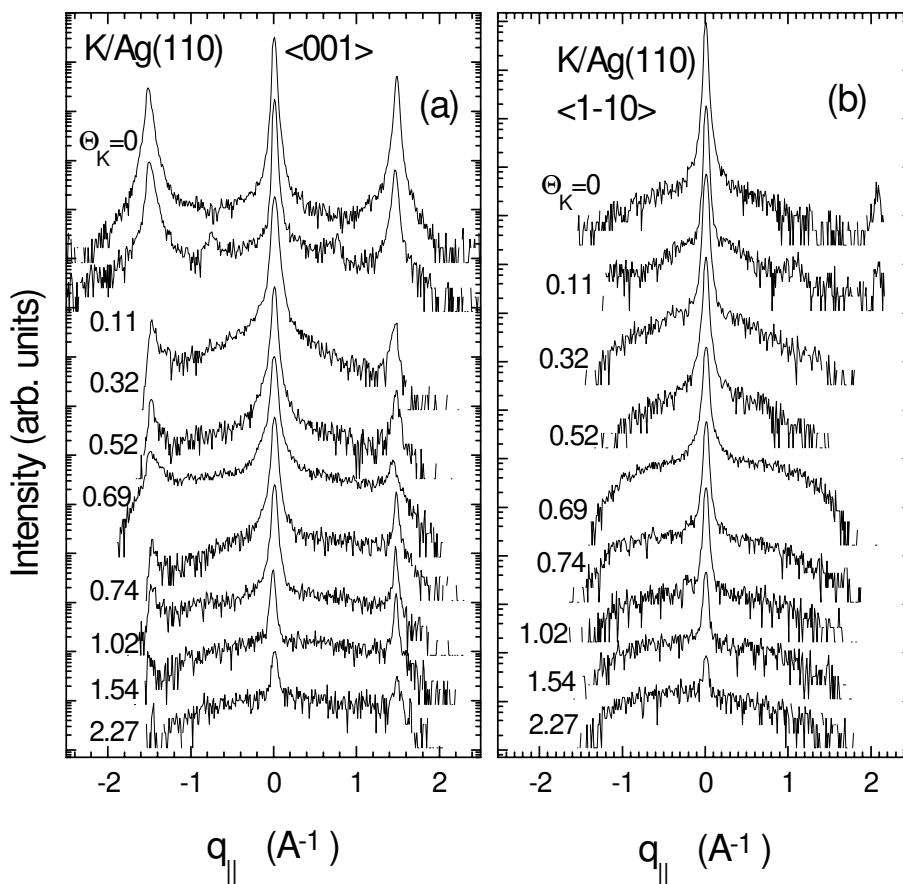


Figure 4.18: SPA-LEED spectra of the K films for different K coverages along the two high symmetry directions, for $T_{dep} = 100$ K: a) $\langle 001 \rangle$ and b) $\langle 1\bar{1}0 \rangle$. The data for $\Theta_K = 0$ and $\Theta_K = 0.11$ ML were recorded at $E_i = 65.4$ eV, while all other spectra were collected at $E_i = 51.4$ eV.

tion causes a generalized decrease of the intensity of the diffraction spots

and the formation of an elastic background peaked exponentially around the diffraction channels. The intensity of the (00) diffraction spot decreases exponentially with Θ_K , indicating a strong increase of the surface roughness and an increased vertical displacement of the atoms [26, 31]. At $\Theta_K = 0.11$ ML additional features are present between zero and first order diffraction peaks along $\langle 001 \rangle$, indicating a local (1×2) reconstruction of a portion of the substrate surface. Weaker additional features are visible along $\langle 1\bar{1}0 \rangle$ at the same K coverage and are due to a correlation between K adatoms, as already discussed in section 4.2. At higher Θ_K any additional peak in the SPA-LEED patterns is present, because of the disordered K adsorption. For $\Theta_K > 0.3$ ML we expect from ref.[35] a higher reconstruction temperature, so that even local reconstruction is inhibited at $T = 100$ K.

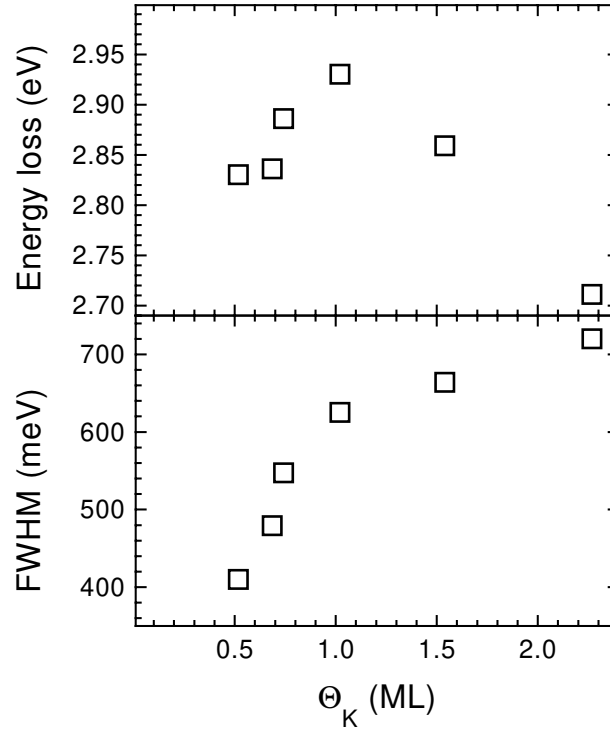


Figure 4.19: Upper panel: energy of the K related loss versus Θ_K at $q_{\parallel} = 0$; lower panel: damping versus Θ_K of the same feature.

In Fig.4.19, $\hbar\omega^K$ and the FWHM of the K related feature are reported versus Θ_K . The mode appears at $\Theta_K \approx 0.5$ ML at $\hbar\omega^K = 2.81$ eV and

shifts then up to 2.93 eV at the completion of the first K layer, while getting broader. Its energy diminishes eventually again for $\Theta_K > 1$ ML. We notice that at $\Theta_K = 2.27$ ML the maximum of the K related loss has reached the same energy as reported for the surface plasmon of a thick K film [71].

The appearance of the K induced loss only above $\Theta_K = 0.52$ ML can be associated to the interband transition between the s and p states of K. A similar late onset of the interband transition was reported for K/Ag(001) [67] and attributed to the fact that the K induced s state is empty below a critical coverage of 0.5 ML. We believe that the same explanation holds also for the present case.

The energy of the interband transition grows initially with Θ_K and decreases eventually. Such a result is at variance with the cases of K/Al(111) and K/Ni(111) [71, 73], where a monotonous increase up to $\Theta_K = 2$ ML was reported. The effect is probably due to the onset of the collective mode of the overlayer above $\Theta_K = 1$ ML. The presence of this mode would be expected at larger coverage, but its formation could occur already at a small average coverage because of the roughness and of the inhomogeneity of the film.

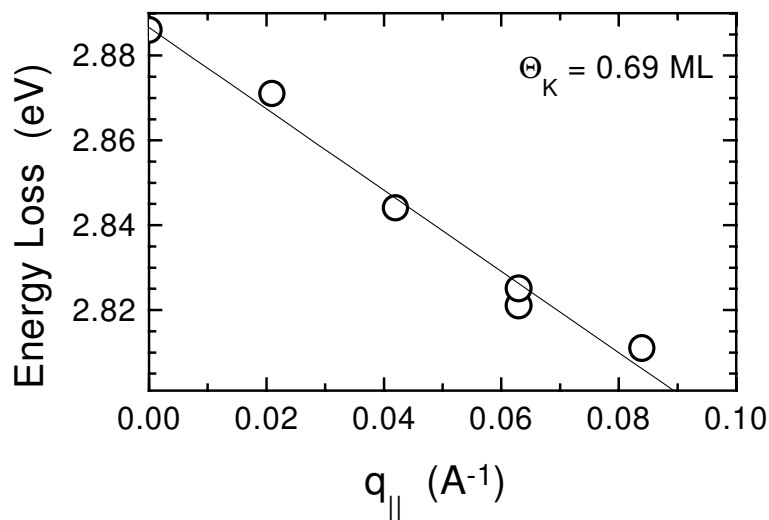


Figure 4.20: Dispersion of the K related loss vs. q_{\parallel} at $\Theta_K = 0.69$ ML. The continuous line is the best fit obtained with the χ^2 method.

The dispersion of the K related energy loss peak versus q_{\parallel} for $\Theta_K = 0.69$ ML is reported in Fig.4.20. Beyond $q_{\parallel} = 0.1 \text{ \AA}^{-1}$ the peak broadens considerably and the inelastic intensity vanishes. The dispersion is linear and

negative with a slope of -0.96 ± 0.06 eVÅ, while $\hbar\omega^K(0) = 2.89$ eV. The q_{\parallel} dispersion of the loss measured at $\Theta_K = 0.69$ ML is nearly identical to the one reported for the K surface plasmon and it probably corresponds to areas of the surface where multiple layers have already formed.

Chapter 5

Thin Ag films

5.1 Introduction

Ultrathin films of silver grown on Si(111) 7×7 constitute an especially interesting system because flat Si(111) surfaces can be easily obtained, no Ag silicide formation is observed, and the silicon substrate is insulator at low temperature.

Recent Scannel Tunneling Microscope (STM) investigations [74, 75] have shown that Ag initially grows on Si(111) 7×7 in a 2D layer-like mode at $T=100\text{K}$, while deposition at room temperature leads to a layer-by-layer growth up a coverage of a few monolayers [74].

The problem of the conductivity of ultrathin metallic films has been studied over decades and it still of great interest, especially for the applications to the miniaturization of integrated circuits. Besides, the question if a perfect 2D silver film could be considered metallic and possibly how thick the layer has to be to show a metallic behaviour has a fundamental scientific interest. Photoemission studies of thin Ag films deposited on Si(111) 7×7 at $T = 100$ K are in progress [76], while the conductivity threshold has recently been measured on the same system, for different temperature of deposition and annealing [77]. Magnetoconductivity studies performed at very low temperature ($T < 20$ K) have moreover evidenced at low Ag coverage an unexpected decrease of the conductivity [78].

The Ag/Si(111) 7×7 system is therefore perfectly suited for a combined energy-loss and structural analysis, with the aim of correlating the electronic properties, monitored by the Ag plasmon energy and dispersion, with the

morphology of the film, which can be easily modified by changing the temperature of deposition and annealing and can be analyzed by means of SPA-LEED. The problem of the metallic character of an ultrathin Ag layer can be considered by measuring the threshold of collective electronic excitations.

According to A. Liebsch [3], collective modes on silver overlayers are expected to appear at a coverage of about two monolayers, at a frequency considerably higher than the one of the bulk or of the surface plasmon on semi-infinite Ag. As the coverage is increased, the overlayer mode should become sharper and the frequency should shift to lower values, approaching the surface plasmon frequency of Ag. The collective excitation of the overlayer is expected to be strongly blue shifted relative to the Ag surface plasmon frequency and to have a negative dispersion. With increasing film thickness the frequency decreases approaching the value of surface plasmon, while the dispersion should become positive.

With the present ELS-LEED study we have been able to qualitatively confirm the predictions of Liebsch's theory and to demonstrate the strong influence of the size of the grains building up the overlayer on plasmon energy and dispersion.

5.2 SPA-LEED analysis of the Ag overlayer

The general nature of the growth process of Ag on Si(111) 7×7 is well known and it has been shown to occur in a layer-by-layer mode. STM studies performed in the last ten years have evidenced that Ag forms initially triangular 2D islands [74], with a close packed (111) arrangement of Ag atoms, while the 7×7 reconstructed Si substrate is not affected by the deposition of Ag, at least if the film is annealed at temperatures lower than 500 K. Above such temperature a phase transition to the $\sqrt{3} \times \sqrt{3}$ phase takes place for a coverage of some monolayers [79], while the symmetry remains (1×1) for thick Ag films.

In the present study Ag has been deposited on Si(111) 7×7 as described in section 2.4.4, either at a crystal temperature of 100 K followed eventually by annealing, or by keeping the crystal at room temperature.

One-dimensional LEED patterns obtained for deposition at $T=100$ K with increasing Ag coverage for a given E_i are reported in Fig.5.1. Other data were collected at the same coverages for E_i in a range spanning approximately between 50 eV and 80 eV. Thicker layers of 18 ML and 45 ML of Ag

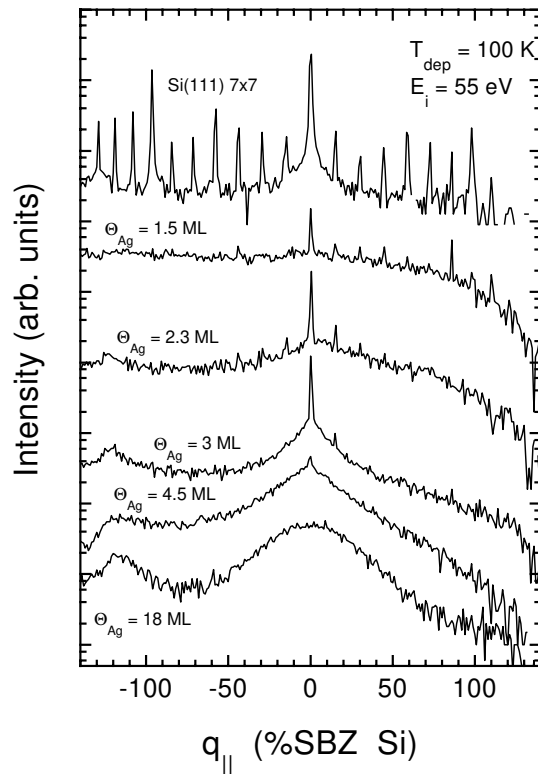


Figure 5.1: SPA-LEED spectra recorded at $T=100$ K for different Ag coverage at $E_i = 55$ eV.

were investigated, too. As one can see in Fig.5.1, with increasing Ag coverage the intensity of the Si (7×7) spots decreases while a structured background forms. At $\Theta_{Ag} = 2.3$ ML the (10) peak of the Ag(111) structure appears. Such feature is quite broad and, as it will be shown later, it shows the polycrystalline character of the layer. A broad shoulder grows with coverage on the (00) peak, indicating an increasing disorder at the surface.

The dependence of the SPA-LEED spectra from the electron energy is shown in Fig.5.2 for $\Theta_{Ag} = 1.5$ ML and $\Theta_{Ag} = 3$ ML and deposition temperature of 100 K. For $\Theta_{Ag} = 1.5$ ML no diffraction peak associated to the Ag overlayer is observed while some of the Si(111) 7×7 spots are still visible, showing that the layer is partially transparent or incomplete. For $\Theta_{Ag} = 3$ ML the silicon peaks is not visible anymore, indicating that the Si surface is now totally covered by the Ag layer; the Ag(111) peak, very broad,

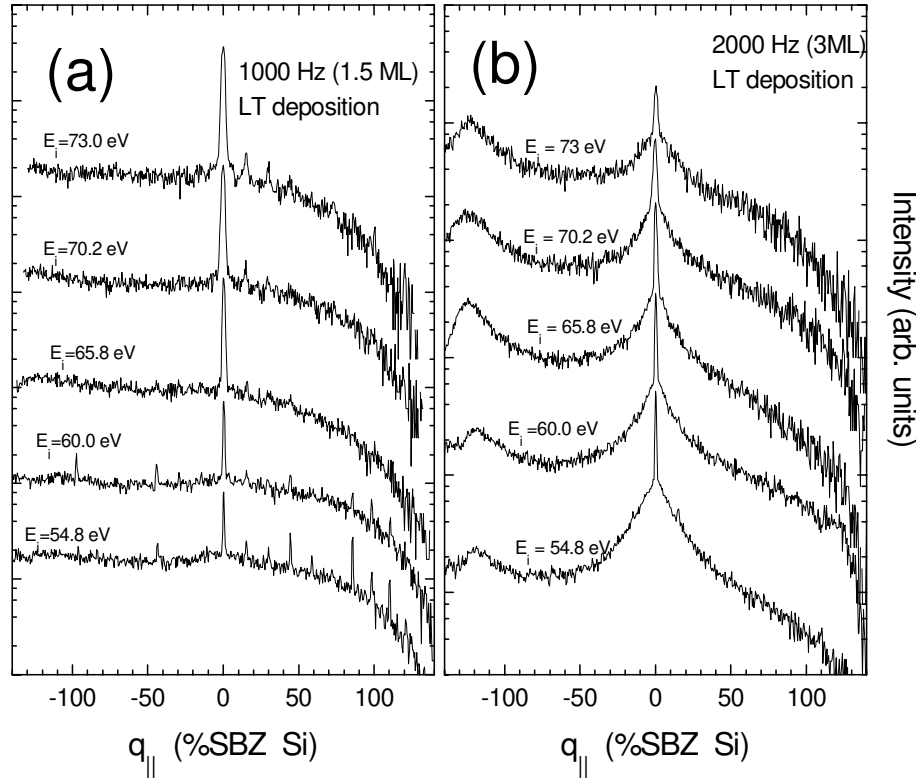


Figure 5.2: SPA-LEED spectra for Ag/Si evaporated at $T=100$ K at different E_i for a) $\Theta_{Ag} = 1.5$ ML and b) $\Theta_{Ag} = 3$ ML.

has already appeared, while the $(1/7\ 0)$ spot of the reconstructed Si is still present, showing a flat modulation of the silver layer on the silicon surface. No periodicity of the profile of the peaks with energy is observed, while, with increasing E_i , a general lowering of the intensity of the peaks takes place.

The (10) Ag peak is strongly influenced by the lateral disorder at the surface and can give quantitative information on the dimension and the orientation of the grain size. From the radial FWHM of the Ag (10) spot it is in fact possible to estimate the lateral size of the Ag grains, which, in the case of the experiment reported in Fig.5.2b, is about $15\ \text{\AA}$. In Fig.5.3, a two-dimensional LEED pattern is reported for the case of $\Theta_{Ag} = 1.5$ ML. As one can see the Ag spots are not point-like, but have an arc-shape, indicative of a rotational disorder at the surface.

Let us consider now what happens to the Ag film if we anneal it to room

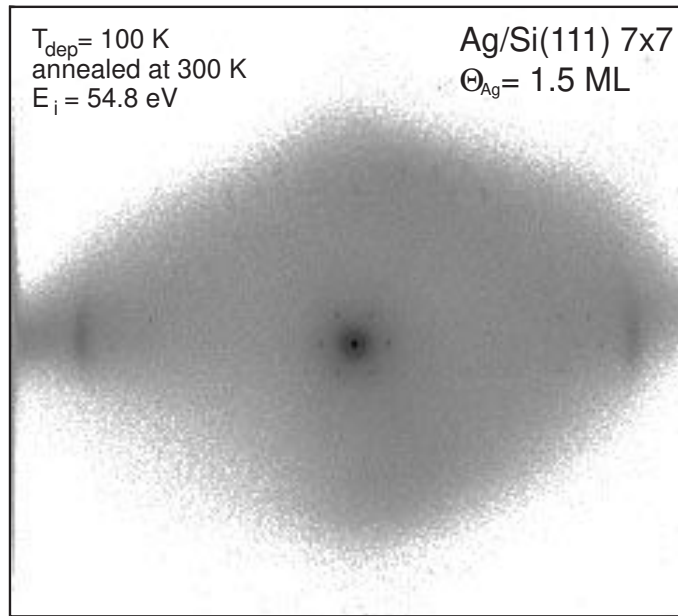


Figure 5.3: Two dimensional LEED pattern for 1ML Ag/Si(111) 7×7 deposited at 100 K and annealed at 300 K.

temperature or if we directly deposit silver at $T=300$ K. In Fig.5.4 the SPA-LEED spectrum recorded at $\Theta_{Ag} = 3$ ML is compared with the spectrum of the same layer after annealing at $T=300$ K and with the one obtained after deposition of the same amount of silver at room temperature. Other data have been recorded for room temperature deposition at $\Theta_{Ag} = 1.5, 2.3$ and 4.5 ML in a E_i range between 50 and 80 eV, while the layers obtained after deposition at $T=100$ K have been annealed to room temperature for $\Theta_{Ag} = 1.5$ and 3 ML and up to 600 K for $\Theta_{Ag} = 18$ ML and 45 ML.

As one can see, the intensity of the spots, reported on a logarithmic scale, increases slightly after annealing of a coldly deposited film, while the spots are much more intense for room temperature deposition. The profile of the shoulder does not change significantly, while the $(1/7)$ spot of the reconstructed silicon is still present. The Ag layer is still modulated on the Si structure, while the main effect of the increased temperature is the narrowing of the Ag(10) spot, which indicates a growth of the Ag grains. The average dimension of such grains passes from 15 Å for low temperature deposition

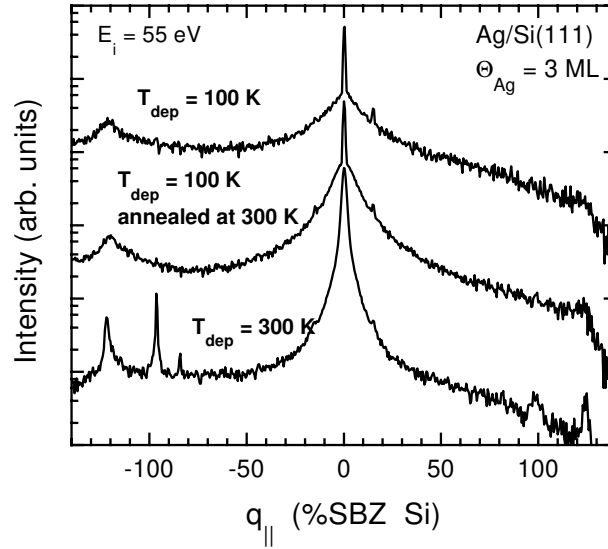


Figure 5.4: Comparison between the SPA-LEED spectra recorded for $\Theta_{Ag} = 3$ ML after evaporation at $T=100$ K, annealing at $T=300$ K and deposition at $T=300$ K.

to 94 Å after deposition at 300K. The film obtained for room temperature deposition presents however some holes, as demonstrated by the appearance of the (10) silicon spot.

In Fig.5.5 the behaviour with E_i of the LEED data recorded after room temperature deposition, for $\Theta_{Ag} = 1.5$ and 3 ML is reported. As one can see for $\Theta_{Ag} = 1.5$ the Ag(111) peak is already present, while it was not visible on the coldly deposited layer of the same thickness. In the case of room temperature deposition, for $\Theta_{Ag} \leq 3$ ML, the (10) spot of Si is visible, indicating that the Ag layer is not complete. By calculating the ratio of the intensity of such a peak relatively to the one of the (00) spot and by comparing the so obtained ratio with the one corresponding to the clean Si surface case, it has been possible to estimate that the amount of Si surface free from silver is less than 6% for $\Theta_{Ag} = 1.5$ ML and less than 3% for $\Theta_{Ag} = 3$ ML. These values indicate that the layer, even if not completely closed, shows only some broken areas, while the presence of separated Ag islands has to be excluded.

The broad and intense shoulder on the (00) spot cannot be explained by the lateral disorder of the grains, which is expected to influence only the (10)

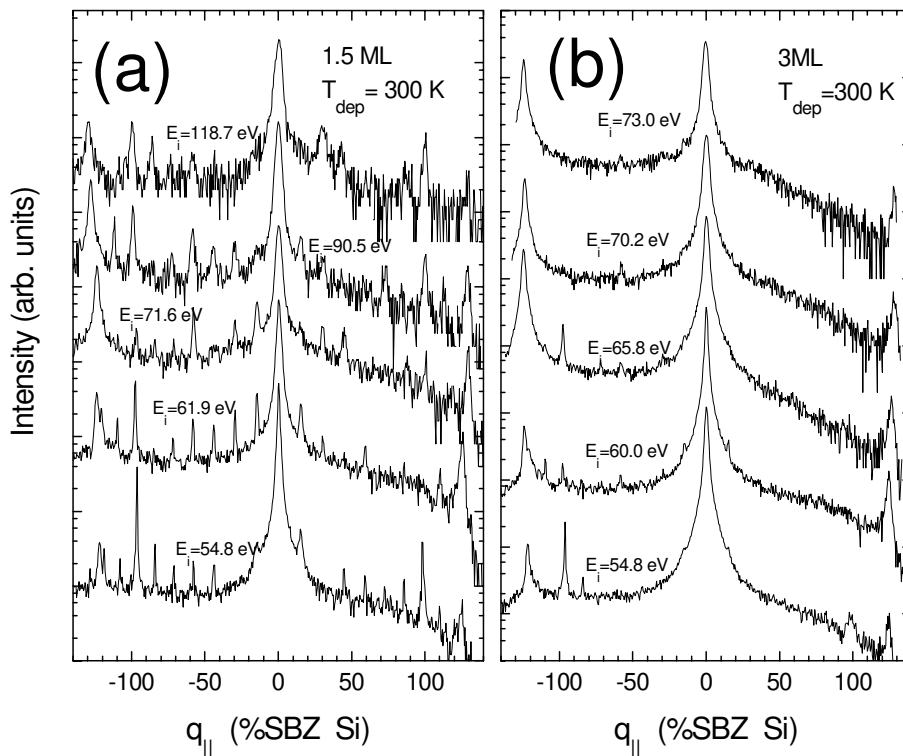


Figure 5.5: SPA-LEED spectra for Ag/Si evaporated at $T=300\text{K}$ at different E_i for a) $\Theta_{Ag} = 1.5\text{ ML}$ and b) $\Theta_{Ag} = 3\text{ ML}$.

silver spot. Such a shoulder is present for all temperatures of evaporation and annealing and, as shown in Fig.5.1 for the low temperature evaporation case, it increases with coverage. Moreover, a mosaic structure has to be excluded, as in this case an increase of the width of the peaks with E_i would be expected.

If such shoulder were due to the presence of steps at the surface, it would disappear when the in-phase conditions for the Ag(111) surface are met [32], i.e. for energies:

$$E_i = \frac{\hbar^2 \pi^2}{2m} \frac{s^2}{d^2 \cos^2 \Theta} \quad (5.1)$$

where d is the vertical distance between two Ag atoms (2.36 \AA), Θ is the incidence angle (6° in the ELS-LEED geometry) and $s = \Delta k_\perp / 2\pi$ is an integer in the in-phase condition. For $s = 3$ the in-phase condition corresponds to $E_i = 60\text{ eV}$, where, as one can see from Fig.5.2 and 5.5, the shoulder is still present, indicating a strong surface disorder due to inhomogeneity. Moreover,

an eventual epitaxial roughness of the layer could be proved if the ratio between the integral intensity of the central spike (I_{spike}) and the total integral intensity (I_{tot}) would be periodic with s [32]. Such ratio, as calculated after a lorentian fit of the peaks done by the software program NUMFIT developed in the Institut für Festkörperphysik of the University of Hannover, is reported in Fig.5.6 for both temperature of deposition and for different Ag coverages. As one can see, I_{spike}/I_{tot} does not change significantly with s and does not show any periodicity, demonstrating that the presence of steps has to be excluded. The surface of the layer shows therefore a random disorder, but it is mostly flat.

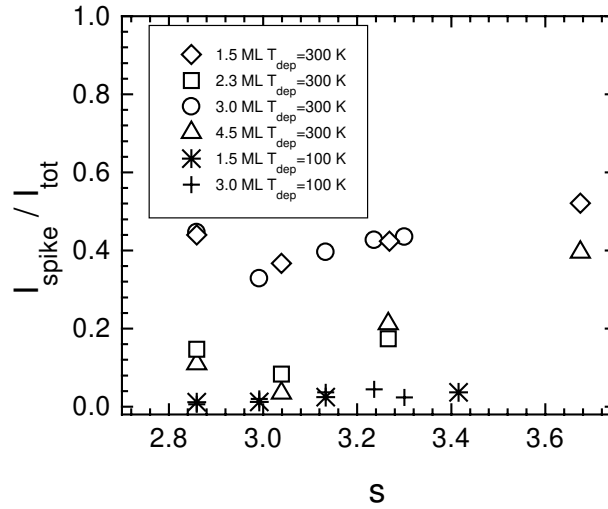


Figure 5.6: Ratio between the integral intensity of the central spike and the total integral intensity versus $s = \Delta k_{\perp}/2\pi$, for different Θ_{Ag} and for different temperature of deposition.

The observed, non-periodic, profile of the shoulder can be partially due to the presence of a gap at the grain boundary, i.e. to a displacement between neighbouring grains which creates additional surfaces, but the observed intensity and width of the shoulder is too large to be caused only by such effect. An additional broadening can be determined by a vertical displacement between neighbouring grains, due to stacking faults or to dislocations. Such a vertical disorder, smaller than the atomic distance, is not periodic with energy and can be numerically estimated by considering the relative integral intensity of the shoulder respect to the central spike in the in-phase

Table 5.1: Average diameter of the Ag grains (d) as calculated from the FWHM of the Ag (10) spot of the SPA-LEED spectra, for different Ag coverage and at different temperature of deposition and annealing.

Θ_{Ag} (ML)	T_{dep} (K)	T_{ann} (K)	d (Å)
2.3	100	-	15 ± 2
3	100	-	15 ± 2
7.6	100	-	15 ± 2
1.5	300	-	95 ± 2
2.3	300	-	59 ± 3
3	300	-	94 ± 2
4.5	300	-	42 ± 2
1.5	100	300	34 ± 2
3	100	300	23 ± 2
18	100	660	30 ± 2
45	100	660	74 ± 2

condition ($E_i = 60$ eV in the present case) [32]. The value of:

$$G_0 = \frac{I_{shoulder}}{I_{spike} + I_{shoulder}} \quad (5.2)$$

where I is the integral intensity of the LEED peak, is related to the average vertical displacement W by:

$$G_0 = e^{-W^2 k_{\perp}^2} \quad (5.3)$$

where k_{\perp} is the vertical component of the exchanged momentum. From this calculation it has been possible to conclude that such a vertical displacement is present, with a value of W in between 5% and 11% of the Ag vertical interatomic distance (2.36 Å). Such disorder increases slightly with coverage, while the lowest values correspond to the annealed or to the room deposition cases.

In conclusion, from the analysis of the LEED profile of Ag overlayers deposited on Si(111) 7×7 , it follows that:

1) For deposition at $T=100$ K, the Ag layer is nearly completed at $\Theta_{Ag} = 1.5$ ML and fully completed for 2.3 ML, while for deposition at $T=300$ K the

layer presents holes not larger than 6% of the surface area.

2) The presence of a lateral disorder is demonstrated by the large width of the Ag(10) peak and indicates a polycrystalline Ag layer, with a rotational disorder between the grains.

3) The dimension of the Ag grains increases with temperature of annealing and deposition. The values of the average diameter of the grains has been calculated from the FWHM of the Ag (10) spot and are reported in Table 5.1. The diameter of the grain, d , has been obtained by averaging on the different measures done over a range of E_i between 50 and 70 eV. As one can see, the average diameter of the Ag grains increases by nearly a factor 6 between low and high temperature deposition, even if it cannot be strictly correlated to the temperature or to the coverage, depending probably also from other experimental conditions such as deposition rate, substrate cleanliness or annealing time.

4) The broad shoulder of the (00) spot is indicative of the superposition of two different phenomena: the presence of a gap between the Ag grains and a vertical displacement between neighbouring grains smaller than 10% of the atomic vertical distance on Ag(111).

5.3 Plasmon energy on Ag overlayers

Energy loss spectra have been measured on the Ag overlayers deposited on Si(111) 7×7 for different temperature of deposition and annealing. Some sample spectra for $\Theta_{Ag} = 3$ ML, recorded at $q_{\parallel} = 0$, are reported in Fig.5.7. Only one peak is present in the energy loss spectra, due to the excitation of the plasma mode of the Ag overlayer. As one can see, with increasing temperature of annealing and deposition, the intensity of the peak increases strongly, while its width diminishes. This behaviour is due to the better order at the surface with increasing temperature, as discussed in the previous section. A more surprising effect is the shift of the plasmon energy: for deposition at T=100 K the layer has a plasmon energy $\hbar\omega_L = 4.15$ eV, after annealing at T=300 K of the same layer we observe $\hbar\omega_L = 4.05$ eV, while on the layer obtained for evaporation at T=300 K we have $\hbar\omega_L = 3.89$ eV. Moreover, the threshold of the appearance of the plasma excitation is observed to be influenced by the temperature. For deposition at T=100 K the plasmon appears at $\Theta_{Ag} = 3$ ML at $\hbar\omega_L = 4.15$ eV, while on the layer annealed at room temperature we observe a peak already for $\Theta_{Ag} = 1.5$ ML,

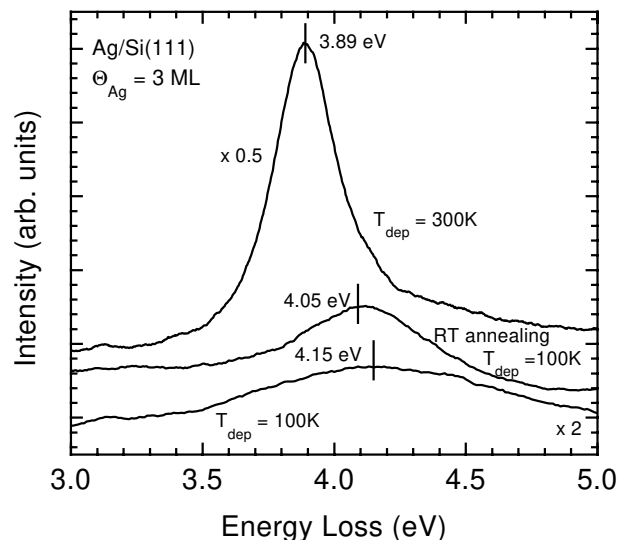


Figure 5.7: Comparison between the energy loss spectra recorded for $\Theta_{Ag} = 3$ ML after evaporation at $T=100$ K, annealing at $T=300$ K and deposition at $T=300$ K, after a smoothing of the experimental data.

at $\hbar\omega_L = 4.24$ eV. With increasing Ag coverage the maximum of the plasmon loss shifts towards lower energies, with a rate which depends again on the temperature of deposition and annealing.

From the model of Liebsch for thin metal overlayers described in section 1.2.3 [6, 3], it is expected that the s - d mutual polarization, considered as an effective polarizable medium of dielectric constant ϵ_d , causes an increasing blue shift of the plasmon with decreasing coverage in analogy to the blue shift of the Ag surface plasmon as a function of q_{\parallel} and of the Ag Mie resonance as a function of $1/R$. The plasmon energy of the Ag overlayer should then be inversely proportional to the layer's thickness, with a slope comparable to the dispersion linear coefficient of the Ag surface plasmon.

The energy of the surface plasmon, obtained from the maximum of the loss peak as described in section 3.2, is reported in Fig.5.8 versus the inverse of the layer thickness, t . The value of t has been calculated from the Ag coverage, considering that the vertical distance between Ag atoms in the Ag(111) structure is 2.36 Å. As one can see, both the data corresponding to deposition at $T=100$ K and the data corresponding to deposition at $T=300$ K show a linear blue shift with $1/t$. However the points relative to different temperature of deposition lie on different lines, which have different slopes.

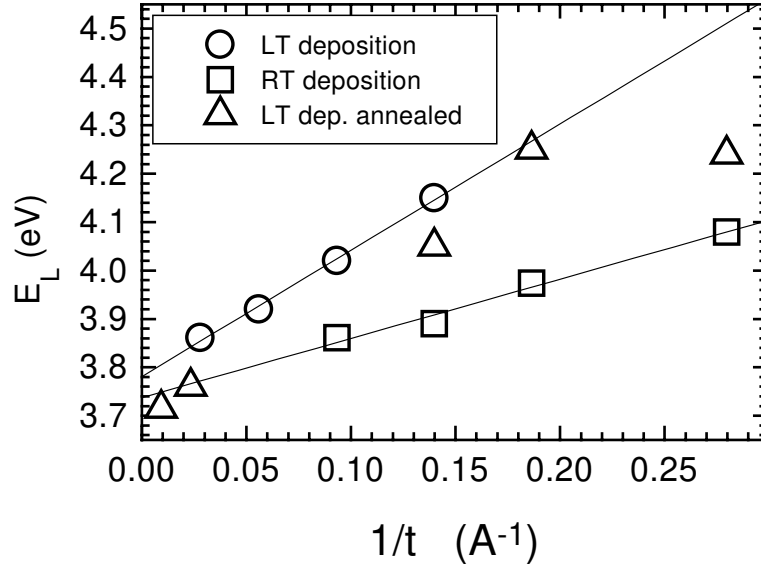


Figure 5.8: Plasmon energy versus the inverse of the layer's thickness. The continuous lines show the linear fit on the two sets of data collected after evaporation at $T=100$ K and $T=300$ K.

The data points recorded after annealing of the layers deposited at low temperature lie on the other hand between the two lines. Such data have been obtained under different annealing conditions (the temperature and the time of the annealing is not the same for all the data) and cannot be therefore directly compared. A linear fit for the low temperature and for the high temperature deposition case reads respectively:

$$\hbar\omega_L\left(\frac{1}{t}\right) = (3.78 \pm 0.01) + (2.61 \pm 0.1)\frac{1}{t} \quad (5.4)$$

for deposition at $T=100$ K, and

$$\hbar\omega_L\left(\frac{1}{t}\right) = (3.74 \pm 0.02) + (1.22 \pm 0.1)\frac{1}{t} \quad (5.5)$$

for deposition at $T=300$ K. For both relations the energy is measured in eV, while the thickness is given in Å.

The data obtained for the low temperature case are in perfect agreement with a recent optical study done on the same system at the same temperature by Borensztein et al. [24]. By means of real-time optical spectroscopy they

obtain in fact a threshold of the plasma resonance for 3ML coverage at $\hbar\omega_L = 4.25$ eV, while the experimental points overlap perfectly.

A previous work by Layet et al. [80] reports on the plasma excitations at the interface between Ag and Si, after deposition at room temperature. Two separated modes are observed and their shift with coverage is explained by means of a classical dielectric theory of an interface between two different metallic materials. The data are not easily comparable with the present ones and with the results of Borensztein, but the higher mode looks like to have energies significantly lower than the one in ref.[24] and to be in better agreement with the present values for room temperature deposition, while the lower one has not been observed neither in the present experiment, nor in ref.[24].

The difference between low and room temperature deposition observed in the present work, has to be ascribed to the different conditions of the Ag overlayer, as observed by LEED measurements and as discussed in the previous section. From the SPA-LEED analysis it has been evidenced that the main difference between room and low temperature deposition is the dimension of the Ag grain on the polycrystalline silver layer, reported in Table 5.1. The experimental data reported in Fig.5.8 show clearly that an effect due to the grain size has to be taken into account to explain the observed behaviour. The data of Fig.5.8 have been replotted in Fig.5.9 versus the inverse of the grain size, considering both the vertical thickness, given by the Ag coverage, and the lateral dimension given by the values in Table 5.1. The single grain, considered as a cylinder of radius r and height t , has been approximated by a sphere having the same volume to surface ratio. Since a cylinder of radius r and height t has a surface to volume ratio:

$$\frac{S}{V} = 2 \left(\frac{1}{r} + \frac{1}{t} \right) \quad (5.6)$$

and a sphere of radius r has $S/V = 3/r$, the experimental data have been then plotted versus $1/x = 1/t + 1/r$.

As shown in Fig.5.9, all the data, included the annealed points, lie now on the same line demonstrating the strong influence of the lateral grain size on the plasmon energy. A linear fit gives then:

$$\hbar\omega_L \left(\frac{1}{x} \right) = (3.62 \pm 0.02) + (1.73 \pm 0.1) \frac{1}{x} \quad (5.7)$$

corresponding, in the Liebsch's notation reported in eq.(1.24) to a value of the parameter $D_L = -(0.96 \pm 0.04)$ Å. Such value is not in very good agreement

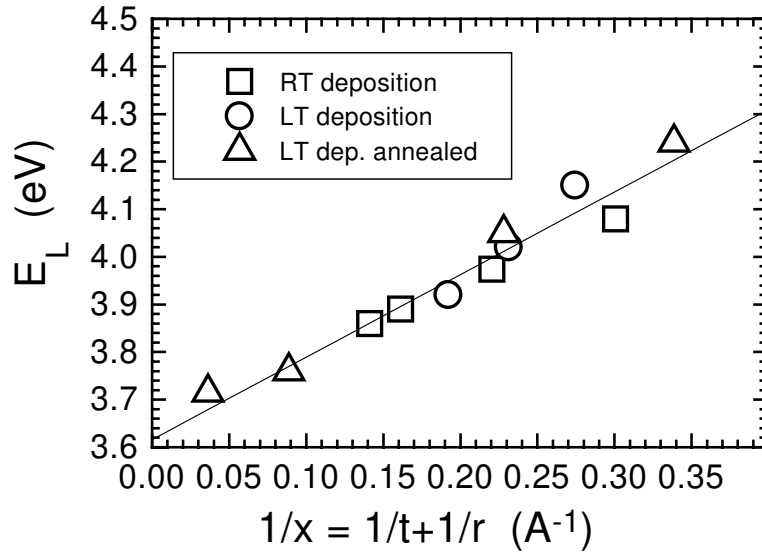


Figure 5.9: Plasmon energy versus the inverse of the dimension of the grain. The continuous line is a linear fit, done on all the data.

with the value of $D_s = -0.23 \text{ \AA}$, obtained for the semi infinite Ag(111) surface, even if it is nearer to the value of -0.85 \AA reported for Ag clusters [22], which are expected to be governed by the same physical mechanism (see section 1.2.3).

In conclusion we have demonstrated that the plasmon of a polycrystalline Ag layer is determined by the size of the grain and behaves like the Mie resonance of Ag clusters of the same size. The central role played by the surface to volume ratio of the grain is in agreement with Liebsch's model, demonstrating that the description of the s - d mutual polarization by means of a polarizable medium which does not coincide with the geometric border of the cluster is correct and it is able to explain also more complicated geometries like the present one.

The influence of the shape of a cluster on the plasma frequency has been theoretically studied inside the jellium model [81], demonstrating that the plasmon energy is increased passing from a spherical to a cubic cluster, being however limited between $\omega_M = \omega_p/\sqrt{3}$ and $\omega_s = \omega_p/\sqrt{2}$. A similar effect could be present in the case of silver, where we observe a value of the plasma frequency of 3.62 eV, slightly larger than the expected value for the Mie resonance of spherical clusters ($\hbar\omega_M = 3.5 \text{ eV}$), but smaller than the surface

value, $\hbar\omega_s = 3.7$ eV.

5.4 Plasmon dispersion on Ag overlayers

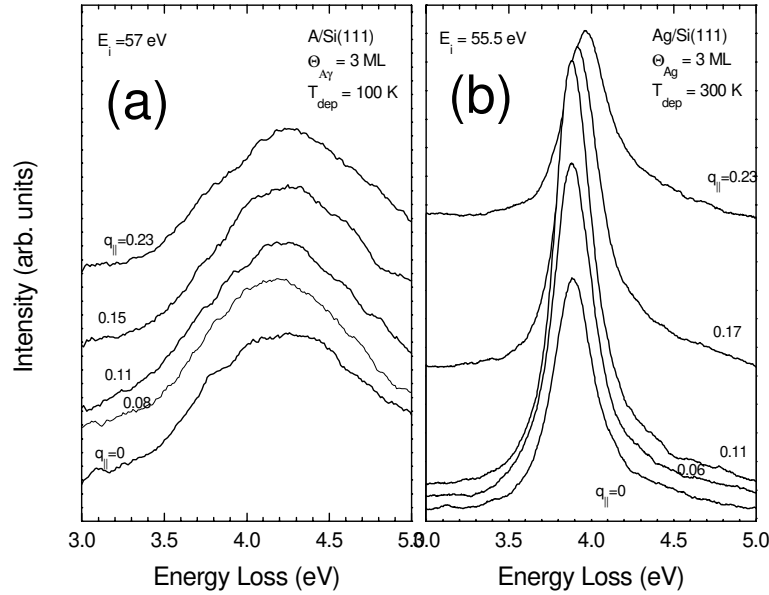


Figure 5.10: Sample energy loss spectra recorded for different $q_{||}$, after a smoothing of the experimental data, for $\Theta_{Ag} = 3$ ML deposited a) at $T=100$ K and b) at $T=300$ K.

The dispersion of the plasma mode of the overlayer has been measured by ELS-LEED, for all the experimental conditions considered in the previous section. Sample spectra recorded for $\Theta_{Ag} = 3$ ML for low and room temperature deposition are reported in Fig.5.10. As one can see in the case of low temperature deposition no dispersion of the plasmon is observed, while for deposition at $T=300$ K, the dispersion is initially flat. The plasmon starts to shift towards higher energies after a critical value of $q_{||}$. A totally flat dispersion has been observed for all the measurements corresponding to the deposition of silver at $T=100$ K and for the set of data recorded after evaporation of 3ML of Ag at low temperature followed by annealing at $T=300$ K. For the layer deposited at room temperature and for the other annealed surface, the dispersion, started after a critical value of $q_{||}$, q_0 , is linear and

positive. Surface plasmon energy is reported versus q_{\parallel} in Fig.5.11, for all the sets of data showing a dispersion. The energy of the plasmon for $q_{\parallel} = 0$ is the one discussed in the previous section, while the dispersion is linear and positive for $q_{\parallel} > q_0$. The value of q_0 varies from set to set of data, showing again a dependence on the temperature of deposition and annealing, being related to the dimension of the silver grains. As one can see from the vertical lines reported in Fig.5.11, representing the values of $2\pi/d$, where d is the dimension of the grain reported in Table 5.1, the critical value of q_{\parallel} coincides with $2\pi/d$. The plasmon of the overlayer shows therefore a dispersion only for wavelength smaller than the lateral dimension of the grain. Such result demonstrates that the plasmon on polycrystalline silver is confined inside the single Ag grain. This effect can be explained by the presence of an additional surface, a gap, between neighbouring grains, not excluded by the SPA-LEED analysis, which makes the single grain behave like an isolated cluster. The flat dispersion observed for the low temperature deposition data and for the case of $\Theta_{Ag} = 3$ ML annealed at room temperature can thus be explained considering the very small dimension of the Ag grains (see Table 5.1) which correspond to a large value of q_{\parallel} , outside the range of the experiment. The experimental data have been in fact recorded for $q_{\parallel} < 0.30 \text{ \AA}^{-1}$, i.e. for $\lambda > 20.9 \text{ \AA}$. For larger q_{\parallel} the plasmon loss has too little intensity and it is too much damped to allow for precise measurements. In the present experiment it is therefore possible to see a dispersion of the plasmon only if the grain's size is larger than 21 \AA .

Moreover, also the threshold of the plasma excitations depends on the grain size, as 3ML are necessary to excite the plasmon when $d = 15 \text{ \AA}$, while 1.5 ML are sufficient if the layer has been annealed and the grains have a width of 34 \AA . The same layer thickness is necessary to have plasmon excitation in case of deposition at room temperature, where $d=95 \text{ \AA}$. We can therefore conclude that the threshold for plasma excitation lies between one and two monolayers. It would be however interesting to know if, on a perfect monocrystalline overlayer, the plasmon can be already excited after the completion of the first layer.

A linear fit of the dispersion for $q_{\parallel} > q_0$ is reported in Table 5.2 for the different sets of data reported in Fig.5.11. The dispersion is positive, with a slope that, considering separately the room temperature deposition and the annealed cases, increases with increasing Ag coverage. Such a behaviour is in qualitative agreement with the calculation of Liebsch for the Ag/Al system, where an increasing of the slope with Θ_{Ag} was expected. Nevertheless, the

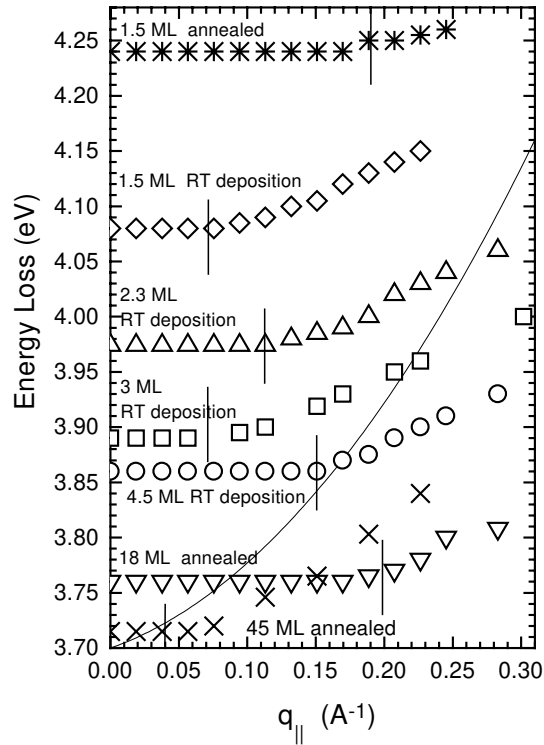


Figure 5.11: Plasmon dispersion versus $q_{||}$ for different Ag coverages and different conditions of deposition and annealing. The vertical lines indicate the value of $q_{||}$ corresponding to the grain size, as obtained by SPA-LEED analysis. The continuous line corresponds to the surface plasmon dispersion on Ag(111).

slope of the dispersion for the annealed data is systematically lower than the one relative to the room temperature deposition, at the same coverage. This phenomenon is again connected to the smaller size of the Ag grains in the annealed case. Moreover, from Fig.5.11, it should be noted that the shape of the dispersion curve does not approach the one of the Ag(111) surface with increasing coverage, but it remains significantly lower, also for $\Theta_{Ag} = 45$ ML.

The slope of the dispersion for $q_{||} > q_0$ is indicative of the behaviour of the plasmon inside the single Ag grain. To relate such a quantity to the grain size, we have reported in Fig. 5.12 the value of the dispersion's slope versus the inverse of the grain size, $1/x$. As one can see, the linear coefficient decreases almost linearly with $1/x$, indicating a strong correlation between

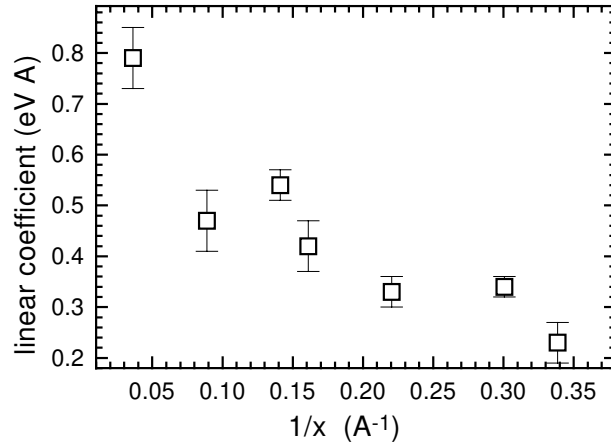


Figure 5.12: Linear coefficient of the plasmon dispersion versus the inverse of the grain size, x .

Table 5.2: Linear coefficient (\AA) of the plasmon dispersion calculated by a χ^2 analysis for $q_{\parallel} > q_0$.

Θ_{Ag} (ML)	T_{dep} (K)	T_{ann} (K)	q_0	\AA (eV \AA)
2.3	100	-	> 0.3	-
3	100	-	> 0.3	-
7.6	100	-	> 0.3	-
1.5	300	-	0.08	0.34 ± 0.02
2.3	300	-	0.11	0.33 ± 0.03
3	300	-	0.06	0.42 ± 0.05
4.5	300	-	0.15	0.54 ± 0.03
1.5	100	300	0.18	0.23 ± 0.04
3	100	300	> 0.3	-
18	100	660	0.20	0.40 ± 0.05
45	100	660	0.08	0.79 ± 0.06

the plasmon dispersion and the dimension of the grain.

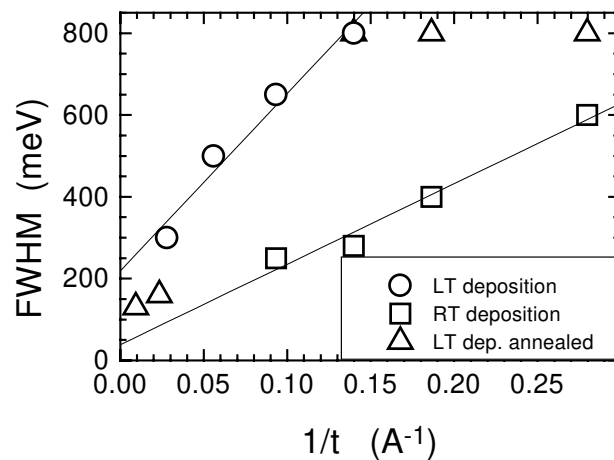


Figure 5.13: FWHM of the plasmon versus the inverse of the layer's thickness. The continuous lines show the linear fit on the two sets of data collected after evaporation at $T=100$ K and $T=300$ K.

5.5 Plasmon damping on Ag overlayers

The FWHM of the plasmon, measured at $q_{\parallel} = 0$, is reported in Fig.5.13 versus the inverse of the layer's thickness. The data indicate a behaviour similar to the one reported in Fig.5.8: the width of the loss peaks increases linearly with $1/t$ for both the data relative to low temperature deposition and to room temperature deposition, while in the first case the damping is much stronger and increases more rapidly. The data set corresponding to the annealed layers lies in-between and do not show linear slope because of the not uniform annealing conditions. A linear fit on the data reads:

$$\Delta E_L\left(\frac{1}{t}\right) = (0.22 \pm 0.05) + (4.34 \pm 0.5)\frac{1}{t} \quad (5.8)$$

for deposition at $T=100$ K, and

$$\hbar\omega_L\left(\frac{1}{t}\right) = (0.04 \pm 0.03) + (1.97 \pm 0.2)\frac{1}{t} \quad (5.9)$$

for deposition at $T=300$ K.

In the case of a Ag spherical Ag cluster it has been shown [21] that the energy and the width of the Mie resonance both depend in the same way on the reciprocal mean radius of the particles. In the present case the

broadening is about 1.6 times faster than the shift of the loss peak, indicating the presence of a further damping mechanism. It is however expected [81] that the shape of the cluster play an important role on the damping rate and that any shape different from the spherical one causes a further increasing of the broadening. Moreover the non uniform size and dimension of the Ag

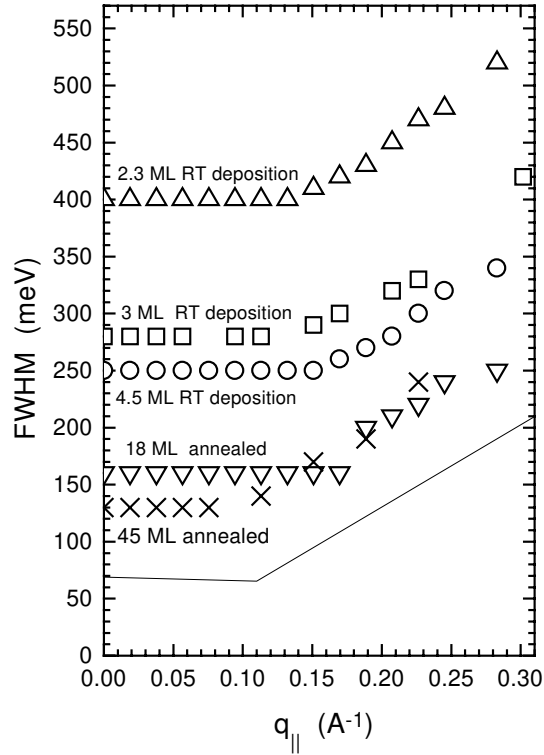


Figure 5.14: FWHM of the plasmon vs. $q_{||}$ for different Ag coverages and different conditions of deposition and annealing. The continuous line corresponds to the damping of the surface plasmon on Ag(111).

grains in the present experiment represent another cause of damping, which is probably more efficient in the case of the smaller grain size. In this frame, it is not possible to simply relate the broadening of the peak to the average grain size, as we have done for the shift of plasmon energy, but it would be necessary to take into account also the shape of the grains and the variance of the size distribution.

The dispersion with $q_{||}$ of the damping of the overlayer plasmon is reported in Fig.5.14, for the sets of data which show a dependence of the FWHM on

Table 5.3: Linear coefficient (B) of the FWHM versus q_c derived by a χ^2 analysis for $q_{\parallel} > q_c$.

Θ_{Ag} (ML)	T_{dep} (K)	T_{ann} (K)	q_c	B (eV Å)
2.3	300	-	0.11	0.74 ± 0.05
3	300	-	0.06	0.74 ± 0.10
4.5	300	-	0.15	0.73 ± 0.06
18	100	660	0.20	0.74 ± 0.10
45	100	660	0.08	0.72 ± 0.10

the momentum transfer. For the data recorded after Ag deposition at $T=100$ K as well as for the data relative to $\Theta_{Ag} = 1.5$ ML and for the annealed layer corresponding to $\Theta_{Ag} = 3$, the plasmon is very broad and does not show any dependence on q_{\parallel} . In the other cases the FWHM is initially flat with q_{\parallel} and it strongly increases beyond a critical value, q_c . A similar behaviour has been observed on the bare Ag(111) surface, as discussed in section 3.5 and as reported in Fig.5.14, with $q_c = 0.11 \text{ \AA}^{-1}$. In the present case the confinement of the plasmon inside the single grain, demonstrated in the previous sections, has to be considered.

The result of a linear best fit to the data in Fig.5.14 for $q_{\parallel} > q_c$ is collected in Table 5.3. All the slopes have the same value within experimental error, coinciding with the value measured on Ag(111), which reads 0.71 ± 0.03 (see Table 3.5). The damping mechanism for large q_{\parallel} seems therefore to be the same as on the bare surface case, while the large width of the peaks at low q_{\parallel} and the value of q_c have to be connected to the grain size and to the spread of shapes and dimensions of the silver grains on the polycrystalline layer. The observed values of q_c , reported in Table 5.3, are in a quite good agreement with the ones obtained from the dimension of the grain size, as discussed in the previous section, showing the major effect played by the confinement of the plasmon inside the single grain. Notably, the new decay channel that opens on Ag(111) for $q_{\parallel} > q_c$ and that is ascribed to the decay into a electron-hole pair involving a filled Shockley state [2], is already present in the Ag grains.

Conclusions and outlook

In the present work, collective electronic excitations on Ag surfaces and thin films have been experimentally studied by means of ELS-LEED, a spectroscopic technique which allows to greatly improve the precision in surface plasmon dispersion measurements and which makes possible to investigate energy loss and SPA-LEED spectra, giving information about both collective electronic excitations and surface geometry. The application of ELS-LEED to the study of surface plasmons has therefore allowed to better understand the complex problem of the relation between surface plasmon energy and dispersion and the geometrical and electronic properties of silver surfaces, clusters and thin layers.

In the first part of this work, surface plasmon energy and dispersion have been reinvestigated on Ag(111) and Ag(110), reducing by a factor two to four the experimental error in the determination of the surface plasmon dispersion coefficients and confirming the anisotropy of the linear term of the dispersion with respect to crystal face and, for Ag(110), also to crystal azimuth. The quadratic term of the surface plasmon dispersion has been observed to be the same for Ag(111) and Ag(110), while in the case of Ag(001) it nearly vanishes. Moreover, the improved quality of the data has permitted for the first time to separate the contribution to the loss spectra of another sharp mode, which is excited by a different mechanism than dipole scattering. Such mode coincides probably with the multipole plasmon mode, already observed in the case of simple metals and expected whenever the charge-density profile at the surface is not too abrupt.

The meaning of the linear and of the quadratic term of Ag surface plasmon dispersion has been then studied by depositing a small amount of K on Ag(110) and by inducing in this way an extended missing row reconstruction. From the SPA-LEED analysis, it has been observed that surface reconstruction takes place at a very low K coverage along $\langle 001 \rangle$, while

along the unreconstructed $\langle 1\bar{1}0 \rangle$ direction K-induced features are present, indicating a correlation between K adatoms. At larger Θ_K this correlation is stronger and is present along both azimuthal directions demonstrating that the reconstruction is driven by a long range mechanism of electronic origin, in contrast to the local driving force which is apparently active for K/Cu(110). By observing the effects of K adsorption on Ag(110) it has been possible to prove that the quadratic term of Ag surface plasmon dispersion has, at least partially, a surface origin connected to the presence of a surface decay channel for the surface plasmon, associated to surface interband transitions. The linear term of surface plasmon dispersion is not affected by surface corrugation on the atomic scale and by K adsorption, so that its anisotropy must be of electronic origin.

In the last part of this work, thin films of Ag deposited on Si(111) 7×7 have been studied. A combined energy-loss and SPA-LEED investigation has been performed, correlating the electronic properties, represented by the Ag plasmon energy and dispersion, with the morphology of the film. Such study has demonstrated that the collective electronic excitation on polycrystalline Ag overlayers is determined by the dimensions of the Ag grains and behaves like the Mie resonance of Ag clusters of the same size. By measuring the dispersion of such mode it has also been proved that the plasmon remains confined inside the single grain, showing a dispersion only for wavelength smaller than the lateral dimension of the grain.

The results of the present work permit to better understand the electronic excitation spectra of Ag surfaces and thin films, suggesting new and interesting fields of investigation. An ELS-LEED study of the collective electronic excitations on Ag islands deposited on NaCl is in progress, while possible further studies connected to the behaviour of Ag plasmon on small islands or clusters could concern the deposition of Ag on GaAs or on others III-V semiconductors, on which Ag is known to form spherical particles. Besides, the behaviour of plasmons on Ag overlayer could be investigated in more detail by depositing Ag on Al, which represents a free-electron-like substrate for which theoretical calculations are already available. Moreover the evaporation of Ag on stepped Si surfaces can create quasi-unidimensional structures, which could give very interesting informations about the electronic excitation spectra in 1D-systems. Finally, combined ELS-LEED and conductivity measurements could provide very interesting connections among electronic excitations, geometrical structure and electronic transport properties of a metallic layer.

In conclusion, in spite of having been studied over decades, the collective electronic properties of metals are still a very interesting and open research field which will hopefully give many interesting results also in the future.

Bibliography

- [1] P.J. Feibelman, Prog. in Surf. Sci. **12**, 287 (1982).
- [2] M. Rocca, Surf. Sci. Rep. **22**, 1 (1995).
- [3] A. Liebsch *"Electronic Excitations at Metal Surfaces"*, Plenum Press, New York (1997).
- [4] A. Zangwill, *"Physics at surfaces"* Cambridge University Press, Cambridge (1988).
- [5] G. Mie, Ann. Phys. **25**, 377 (1908).
- [6] A. Liebsch, Phys. Rev B **48**, 11317 (1993).
- [7] A. Liebsch, Phys. Rev. Lett. **71**, 145 (1993).
- [8] H. Ehrenreich and H.R. Philipp, Phys. Rev. **128**, 1622 (1962).
- [9] E.D. Palik, in: *"Handbook of Optical Constants of Solids"*, Academic Press, New York (1985), p. 355.
- [10] P. Winsemius, F.F. Kampen, H.P. Lengkeek, G.G. van Went, J. Phys. F **6**, 1583 (1976).
- [11] B.N.J. Persson and E. Zaremba, Phys. Rev. B **31**, 1863 (1985).
- [12] K.D. Tsuei, E.W. Plummer, P.J. Feibelman, Phys. Rev. Lett. **63**, 2256 (1989).
- [13] K.D. Tsuei, E.W. Plummer, A. Liebsch, K. Kempa, and P. Bakshi, Phys. Rev. Lett. **64**, 44 (1990).

- [14] K.D. Tsuei, E.W. Plummer, A. Liebsch, E. Pehlke, K. Kempa and P. Bakshi, Surf. Sci. **247**, 302 (1991).
- [15] S. Suto, K.D. Tsuei, E.W. Plummer and E. Burnstein, Phys. Rev. Lett. **63**, 3198 (1991).
- [16] M. Rocca and U. Valbusa, Phys. Rev. Lett. **64**, 2398 (1990); M. Rocca, F. Biggio and U. Valbusa, Phys. Rev. B **42**, 2835 (1990).
- [17] M. Rocca, M. Lazzarino, and U. Valbusa, Phys. Rev. Lett. **69**, 2122 (1992).
- [18] P.J. Feibelman, Surf. Sci. **282**, 129 (1993).
- [19] F. Moresco, M. Rocca, T. Hildebrandt, V. Zielasek and M. Henzler, Europhys. Lett. **43**, 433 (1998).
- [20] Kreibig and Genzel, Surf. Sci. **156**, 678 (1985).
- [21] K.P. Charlé, W. Schulze and B. Winter, Z. Physic. D **12**, 471 (1989).
- [22] J. Tiggesbäumker, L. Koller, O.H. Lutz and K.H. Meiwes-Broer Chem. Phys. Lett. **190**, 42 (1992); J. Tiggesbäumker, L. Koller, K.H. Meiwes-Broer and A. Liebsch, Phys. Rev. A **48**, 1749 (1993).
- [23] T. Lopez-Rios, M. De Crescenzi and Y. Borensztein, Solid State Comm. **30**, 755 (1979).
- [24] Y. Borensztein, M. Roy and R. Alameh, Europhys. Lett. **31**, 311 (1995);
- [25] H. Lüth, *"Surfaces and interfaces of solids"* Springer Verlag, Berlin (1993).
- [26] M. Henzler, Appl. Phys. A **34**, 205 (1984).
- [27] H. Ibach and D.L. Mills, *"Electron energy loss spectroscopy and surface vibrations"* Academic Press, New York (1982).

- [28] H. Claus, A. Büssenschutt and M. Henzler, *Rev. Sci. Instrum.* **63**, 2195 (1992).
- [29] M. Rocca, F. Moresco and U. Valbusa, in: A.F. Ponce, M. Cardona (Eds.), *Surface Science, Lectures on Basics Concepts of the SLAFS VI*, Springer Proceedings of Physics, vol. 62, Springer Verlag, Berlin (1991), p. 59.
- [30] H. Froitzheim, in "*Electron spectroscopy for surface analysis*", editor H. Ibach, *Topics in Current Physics* **4**, (1987). Springer Verlag, Berlin. p. 205.
- [31] M. Henzler, in "*Electron spectroscopy for surface analysis*", editor H. Ibach, *Topics in Current Physics* **4**, (1987). Springer Verlag, Berlin. p. 117.
- [32] J. Wollschläger, J. Falta and M. Henzler, *Appl. Phys. A* **50**, 57 (1990).
- [33] V. Zielasek, Ph.D. thesis, University of Hannover (1997).
- [34] J.W.M. Frenken, R.L. Krams, J.F. van der Veen, E. Holub-Frappe and K. Horn, *Phys. Rev. Lett* **59**, 2307 (1987).
- [35] W.C. Fan and A. Ignatiev, *Phys. Rev. B* **38**, 366 (1988).
- [36] T. Hildebrandt, Diplome thesis, University of Hannover (1996).
- [37] R. Contini and J.M. Layet, *Solid State Commun.* **48**, 445 (1983).
- [38] G. Lee, P.T. Sprunger and E.W. Plummer, *Surf. Sci.* **286**, L547 (1993).
- [39] M. Rocca and U. Valbusa, *Surf. Sci.* **287/288**, 770 (1993).
- [40] M. Rocca, L. Yibing, F. Buatier de Mongeot and U. Valbusa, *Phys. Rev. B* **52**, 14947 (1995).
- [41] F. Moresco, M. Rocca, V. Zielasek, T. Hildebrandt and M. Henzler, *Surf. Sci.* **338**, 1 (1997).

- [42] F. Moresco, M. Rocca, V. Zielasek, T. Hildebrandt and M. Henzler, Surf. Sci. **338**, 24 (1997).
- [43] F. Moresco, M. Rocca, V. Zielasek, T. Hildebrandt and M. Henzler, Phys. Rev. B **54**, R14333 (1997).
- [44] M.Rocca, F. Moresco and U. Valbusa, Phys. Rev. B **45**, 1399 (1992).
- [45] M. Rocca and F. Moresco, Phys. Rev. Lett. **73**, 822 (1994); Phys. Rev. B **50**, 18621 (1994).
- [46] H. Ishida and A. Liebsch, Phys. Rev. B **54**, 14127 (1996).
- [47] L. Yibing, A. Levi and M. Rocca, Surf. Sci. **336**, 371 (1995).
- [48] A. Goldman, E. Bartels, Surf. Sci. **122**, L629 (1982).
- [49] H. Erschbaumer, A.J. Freeman, C.L. Fu, R. Podloucky, Surf. Sci. **243**, 317 (1991).
- [50] J. Daniels, Z. Phys. **203**, 235 (1976).
- [51] S.R. Barman, K. Horn, H. Ishida and A. Liebsch, Phys. Rev. B **57**, 6662 (1998).
- [52] A.J. Bennet, Phys. Rev. B, Phys. Rev. B **1**, 203 (1970); C. Schwartz and W.L. Schaich, Phys. Rev. B **26**, 7008 (1982).
- [53] F.J. Dobson and G.H. Harris, J. Phys. C **21**, L729 (1988).
- [54] H.J. Levinson, E.W. Plummer and P.J. Feibelman, Phys. Rev. Lett. **43**, 952 (1979).
- [55] A. Liebsch, Phys. Rev. B **57**, 3803 (1998).
- [56] B.E. Hayden, K.H. Prince, P.J. Davie, G. Paolucci and A.M. Bradshaw, Solid State Comm. **48**, 325 (1983).
- [57] C.J. Barnes, M.Q. Ding, M. Litroos, R.D. Diehl and D. King, Surf. Sci. **162**, 59 (1985).

- [58] R.J. Behm, D.K. Flynn, K.D. Jamison, G. Ertl and P.A. Thiel, *Phys. Rev. B* **36**, 9267 (1987).
- [59] R. Schuster, J.V. Barth, G. Ertl, R.J. Behm, *Surf. Sci.* **247**, L229 (1991); *Phys. Rev. B* **44**, 13689 (1991); R. Schuster, J.V. Barth, R.J. Behm and G. Ertl, *Phys. Rev. Lett.* **69**, 2547 (1992);
- [60] R.J. Behm, in: *"Physics and Chemistry of Alkali Metal Adsorption"*, Eds. H.P. Bonzel, A.M. Bradshaw and G. Ertl (Elsevier, Amsterdam 1989) p. 111.
- [61] K.W. Jacobsen and J.K. Nørskov, *Phys. Rev. Lett* **60**, 2496 (1988).
- [62] S.M. Foiles, *Surf. Sci. Lett.* **191**, L779 (1987).
- [63] C.L. Fu and K.M. Ho *Phys. Rev. Lett.* **63**, 1617 (1989).
- [64] K.M. Ho, B.N. Harmon and S.H. Liu, *Phys. Rev. Lett.* **44**, 1531 (1980); B. Reihl, K.H. Frank, and R.R. Schlittler, *Phys. Rev. B* **30**, 7328 (1984).
- [65] W. Jacob, E. Bertel and V. Dose, *Phys. Rev. B*, **35**, 5910 (1987).
- [66] L.E. Urbach, K.L. Percival, E.W. Plummer and H.L. Dai, *Phys. Rev. B*, **45**, 3769 (1992); R.A. Bartynski and T. Gustafsson, *Phys. Rev. B* **33**, 6588 (1986); B. Reihl, R.R. Schlittler, and H. Neff, *Phys. Rev. Lett.* **52**, 1826 (1984).
- [67] J.A.D. Matthew, F.P. Netzer and G. Astl, *Surf. Sci.* **259**, L757 (1991).
- [68] R. Schuster and I.K. Robinson, *Phys. Rev. Lett.* **76**, 1671 (1996); A.C.E. Madsen, P. Stoltze, K.W. Jacobsen, J.K. Nørskov, *ibidem* **78**, 158 (1997).
- [69] J.S. Kim, Lieming Chen, L.L. Kesmodel, P. Garcia-Gonzalez, and A. Liebsch, *Phys. Rev. B* **56**, R4402 (1997).
- [70] A. Liebsch, *Phys. Rev. Lett.* **67**, 2858 (1991);

- [71] J.A. Gaspar, A.G. Eguiluz, K.D. Tsuei and E.W. Plummer, Phys. Rev. Lett. **67**, 2854 (1991).
- [72] K.D. Tsuei, D. Heskett, A.P. Baddorf and E.W. Plummer, J. Vac. Sci. Technol. A **9**, 1761 (1991).
- [73] G. Chiarello, A. Cupolillo, A. Amoddeo, L.S. Caputi, L. Capagno and E. Colavita, Phys. Rev. B **55**, 1376 (1997).
- [74] S. Tosch and H. Neddermeyer, Phys. Rev. Lett. **61**, 349 (1988);
- [75] G. Meyer and K.H. Rieder, Appl. Phys. Lett. **64**, 3560 (1994);
- [76] L. Aballe and K. Horn, private communication;
- [77] T. Lüer, Ph.D. thesis, University of Hannover (1997);
- [78] M. Henzler, T. Lüer and A. Burdach, Phys. Rev. B, in press;
T. Lüer, J. Heitmann and M. Henzler, Phys. Rev. B, in press;
- [79] R.J. Wilson and S. Chiang, Phys. Rev. Lett **58**, 369 (1987);
- [80] J.M: Layet, R. Contini, J. Derrien and H. Lüth, Surf. Sci. **168**, 142 (1986);
- [81] S. Grabowski, M.E. Garcia and H. Bennemann, Phys. Rev. Lett. **72**, 3969 (1994);

List of Figures

1.1	Dielectric function of Ag.	9
1.2	Surface loss function of K.	11
1.3	Position of the centroid of the screening charge	13
1.4	Schematic view of the Liebsch's model	14
1.5	Calculated Ag surface plasmon dispersion	15
1.6	Energy of the Mie resonance of Ag vs. $1/R$	18
2.1	Schematic view of ELS-LEED.	22
2.2	Possible loss events in dipole scattering.	25
2.3	Ewald's sphere for elastic scattering in 2D.	27
2.4	Schematic view of the chamber	28
2.5	AES calibration of the K coverage.	30
2.6	AES calibration of the Ag coverage.	31
3.1	Energy loss spectra for Ag(110).	34
3.2	Ag(110) surface.	35
3.3	Energy loss spectra for Ag(111).	36
3.4	Surface plasmon dispersion at $T=90$ K for Ag(110) and Ag(111).	37
3.5	Surface plasmon dispersion curves for Ag surfaces.	39
3.6	Surface plasmon dispersion at $T=300$ K for Ag(110) and Ag(111).	41
3.7	Ag surface plasmon energy versus T	42
3.8	Dispersion of the FWHM of the surface plasmon at $T=100$ K on Ag(110) and Ag(111).	44
3.9	Energy loss spectra for Ag(110) at different impact energies.	46
3.10	Energy losses and FWHM of the loss peaks versus q_{\parallel} for Ag(110) for two values of E_i	47
3.11	Energy losses and FWHM of the loss peaks versus q_{\parallel} for Ag(111) for different values of E_i	48

3.12	Comparison of the losses observed under different scattering conditions.	49
4.1	SPA-LEED spectra for K/Ag(110) along $\langle 001 \rangle$ for different Θ_K	54
4.2	SPA-LEED spectra for K/Ag(110) along $\langle 1\bar{1}0 \rangle$ for different Θ_K	55
4.3	Correlation length between the K adatoms versus Θ_K	56
4.4	LEED patterns of K/Ag(110)	57
4.5	Atomistic model of the reconstructed K/Ag(110) surface	58
4.6	SPA-LEED spectra for the reconstructed and unreconstructed Ag(110) surfaces at $\Theta_K \approx 0.10$ ML.	59
4.7	Energy loss spectra for different coverage of K on Ag(110).	61
4.8	Surface plasmon dispersion for different Θ_K deposited on Ag(110).	62
4.9	Linear and quadratic coefficients of surface plasmon dispersion of K/Ag(110) versus Θ_K	63
4.10	Energy loss spectra for K/Ag(110) at $\Theta_K = 0.06$ ML and $\Theta_K = 0.32$ ML	65
4.11	Surface plasmon dispersion for K/Ag(110) for $\Theta_K \leq 0.32$ ML.	66
4.12	Dispersion with q_{\parallel} of the FWHM of the surface plasmon for K/Ag(110)	68
4.13	Surface plasmon energy versus Θ_K at $q_{\parallel} = 0$ for K/Ag(110)	71
4.14	K/Ag(110): surface plasmon energy and damping versus Θ_K for $T_{dep} = 100K$	72
4.15	Surface plasmon dispersion for the reconstructed and the unreconstructed Ag(110) surface, at $\Theta_K \approx 0.10$ ML.	73
4.16	Surface plasmon dispersion and damping for K/Ag(110) for two values of Θ_K at $T_{dep} = 100$ K along $\langle 001 \rangle$	74
4.17	Energy loss spectra for K/Ag(110) at $q_{\parallel} = 0$ for $\Theta_K \leq 2$ ML.	76
4.18	SPA-LEED spectra for K/Ag(110) for $\Theta_K \leq 2$ ML on disordered films.	77
4.19	Energy and damping of the K related loss versus Θ_K	78
4.20	Dispersion of the K related loss vs. q_{\parallel} at $\Theta_K = 0.69$ ML.	79
5.1	SPA-LEED spectra recorded at T=100 K for Ag/Si(111) at different Ag coverage	83
5.2	SPA-LEED spectra for Ag/Si(111) evaporated at T=100 K	84
5.3	LEED pattern for 1ML Ag/Si(111).	85

5.4	SPA-LEED spectra for Ag/Si(111) at $\Theta_{Ag} = 3$ ML at different T of deposition and annealing.	86
5.5	SPA-LEED spectra for Ag/Si(111) evaporated at T=300 K	87
5.6	G(s) for Ag/Si(111)	88
5.7	Energy loss spectra for Ag/Si(111) at $\Theta_{Ag} = 3$ ML for different T of deposition and annealing.	91
5.8	Ag/Si(111): plasmon energy versus the inverse of the layer's thickness	92
5.9	Ag/Si(111): plasmon energy versus the inverse of the grain's size	94
5.10	Ag/Si(111): energy loss spectra recorded for different q_{\parallel} at $\Theta_{Ag} = 3$ ML	95
5.11	Ag/Si(111): plasmon dispersion versus q_{\parallel}	97
5.12	Ag/Si(111): linear coefficient of the plasmon dispersion versus $1/x$	98
5.13	Ag/Si(111): FWHM of the plasmon versus the inverse of the layer's thickness	99
5.14	Ag/Si(111): FWHM of the plasmon vs. q_{\parallel} for different Ag coverages and different T	100

List of Tables

3.1	Surface plasmon dispersion coefficients at T=100K for Ag(110) and Ag(111).	38
3.2	Surface plasmon dispersion coefficients for Ag(110) and Ag(111) at T=300 K	41
3.3	Coefficients of a linear fit of $\hbar\omega_s(T)$ for Ag surfaces	42
3.4	Surface plasmon damping parameters of Ag(111) and Ag(110) for $q_{\parallel} < 0.11 \text{ \AA}^{-1}$	44
3.5	Surface plasmon damping parameters of Ag(111) and Ag(110) for $q_{\parallel} > 0.11 \text{ \AA}^{-1}$	45
4.1	Surface plasmon dispersion coefficients for K/Ag(110) along $\langle 001 \rangle$ at T=300 K.	67
4.2	Surface plasmon dispersion coefficients for K/Ag(110) along $\langle 1\bar{1}0 \rangle$ at T=300 K.	67
4.3	Surface plasmon damping coefficients versus q_{\parallel} for K/Ag(110) at T=100 K along $\langle 1\bar{1}0 \rangle$	69
4.4	Surface plasmon damping coefficients versus q_{\parallel} for K/Ag(110) at T=100 K along $\langle 001 \rangle$	70
4.5	Surface plasmon dispersion coefficients for K/Ag(110) for $T_{dep} = 100K$	73
5.1	Average diameter of the Ag grains	89
5.2	Ag/Si(111): linear coefficient of the plasmon dispersion.	98
5.3	Ag/Si(111): Linear coefficient of the FWHM versus q_c	101

Thanks

I would like to thank Prof. M. Henzler and Prof. M. Rocca to have made possible the present work, finding a very interesting subject of collaboration, that I hope will go on nicely also in the future. Their experience and their help have been of fundamental importance during all my work. The attention and the interesting contribution of Prof. A. Liebsch are also acknowledged.

I want then to thank all the people who work at the Institut für Festkörperphysik of the University of Hannover who have collaborated with me during these years and especially Torsten Hildebrandt and Volkmar Zielasek, as well as all the nice friends I met in Hannover.

Curriculum vitae

Francesca Moresco

27th Februar 1965	born in Genova, Italy
October 1971 - June 1979	Primary school in Genova
Sept. 1979 - June 1984	High school (Liceo scientifico) in Genova
July 1984	High school's final exam (Maturitá scientifica)
Sept. 1984 - May 1991	Study of physics at the University of Genova
8th May 1991	Degree in Physics (Laurea in Fisica) at the University of Genova. Title of the thesis: "Dipolar scattering of electrons from Ag surfaces". Supervisor: prof. M.Rocca
Sept. 1991 - June 1994	Teacher of Physics and Electronics in italian high schools
Sept. 1994 - April 1997	Master (Scuola di Specializzazione) in Material science and technology
From September 1995	Scientific collaboration with the Institut für Festkörperphysik of the University of Hannover